

Chiral magnetic domain wall dynamics in synthetic antiferromagnet-ferromagnet lateral junctions

Dissertation

zur Erlangung des
Doktorgrades der Naturwissenschaften
(Dr. rer. nat.)

der

Naturwissenschaftlichen Fakultät II

- Chemie, Physik und Mathematik

der Martin-Luther-Universität Halle-Wittenberg

Vorgelegt von

Herrn Jiho Yoon

Gutachter:

Prof. Dr. Stuart. S. P. Parkin

Prof. Dr. Georg Woltersdorf

Prof. Dr. Pietro Gambardella

Tag der öffentlichen Verteidigung:

29.01.2024

Acknowledgements

First, I would like to express my most profound appreciation to my thesis supervisor Prof. Dr. Stuart S. P. Parkin. He is a great scientist and researcher but also a great mentor who keeps inspiring me during my doctoral studies. I have never met anyone like him with such strong motivation and a relentless pursuit of scientific curiosity. His passion made quite an impression on me and also gave me the courage to dream of my career path as a scientific researcher. I also appreciate his open and creative mind, which enabled me to complete this project. The trust and freedom he gave me made me truly enjoy my experiments with great pleasure. Apart from the research, I'm also very grateful for his patience on my long journey.

I would also be grateful for the beautiful mentorship of Dr. See-Hun Yang. He is one of the most knowledgeable and versatile scientists I have met. He taught me not only the knowledge of magnetic domain wall dynamics but also how to conduct research more carefully and efficiently. Thanks to his continuous support, I broadened my horizons and deepened my thoughts. I enjoyed the discussion with him, and whenever I talked to him, I always learned something. It was my great pleasure to work with him on this project.

I also extend my gratitude to Prof. Dr. Mazhar N. Ali for his mentoring at the beginning of my period in Halle. Working with him as a talented and enthusiastic young scientist, was a great pleasure.

Special thanks should go to Dr. Jae-chun Jeon and Dr. Andrea Miglironi. As senior researchers and at the same time as teammates, they helped me a lot to make this work possible. We spent tremendous time together in the cleanroom and the office to build a team spirit. I am very proud of working with them and glad that we also made significant progress on our work.

I would also like to thank all colleagues and employees of the Max Planck Institute of Microstructure Physics. In particular, Mrs. Sklarek Kornelia and Mr. Kai-Uwe Assmann guided me to the field of lithography, and I love to have expertise over my entire life. I am also thankful to Korean colleagues in our group, Dr. Hyeon Han, Dr. Kun-rok Jeon, Dr. Kyungjune Cho, and Dr. Jae-keun Kim, who encouraged me to finish my Ph.D. successfully. Friday Korean lunchtime and summer barbeque were always fun and fruitful for me. I would also like to thank our racetrack team, Dr. Tianping Ma, Dr. Yicheng Guan, Dr. Hakan Deniz, and Dr. Peng Wang, Dr. Rana Saha, Dr. Holger Meyerheim for fruitful discussions. I would also

emphasize that it was impossible to make this journey without the fantastic support from Mrs. Antje Paetzold, Mrs. Simone Jäger, and Mr. Michael Strauch. Also, I would like to thank our technical support and administration teams for their tremendous and immediate support.

I was fortunate to meet wonderful people during my long Ph.D. journey. Edouard Lesne, James Taylor, Alessandro Fumarola, Amine Wahada, and André Farinha are amazing friends I could and will genuinely rely on. I will undoubtedly miss our Sunday protocol with very nicely chilled bottles of Funky Forelle in August-Bebel-Platz. Also, I would like to thank Annika Johansson, Lukas Fisher, Berthold Rimmler, Pedram Bassirian, and Martha Schulz for being good lunchmates every day. Having lunch in Mensa with lovely friends always gives me great refreshments during the day. It was my great pleasure to meet the wise man Dr. Winfried Heichler. He always taught me the wisdom of life, which hugely supported me in finishing my Ph.D. I am also thankful to my friend Mar Viñallonga for encouraging me to make this work.

I also would like to especially thank Ilya Kostanovskiy, Bodo Kalkofen, Mindaugas Silinskas, and Daniel Meyer for their great friendship. They always encouraged me to finish my dissertation as soon as possible and sincerely supported me from the heart. I wish that our every morning Kaffepause will continue forever.

Words cannot express my gratitude to my friends Wonjong Kim, Dong Cheon Kim, Jejune Park, and Heritage Park. We started a long journey together in 2015, and the time I spent with them in France has still been an excellent foundation for me. Although we are now all in different places, Belgium, Switzerland, Germany, and Korea, I am sure we will see each other soon.

This endeavor would not have been possible without the tremendous support from my family. In 2015, I left them and started my journey in France, USA, and Germany. Over the last eight years, three different countries, they have always been a beacon of unquenchable light for me. I am so happy that I can finally fulfill my promise to them.

Last, I'm deeply indebted to my wife, Han Sol Bae, and my son Ihan Yoon. My Ph.D. journey is made of our relationship, marriage, and the birth of Ihan. I still cannot imagine how we could manage all these things over the last eight years, and it is certainly sure that it would not have been made possible without my wife. My family has been an incredible pillar of support and motivation for my life. Thank you very much for your support and patience.

Abstract

The current induced manipulation of chiral spin textures is of great interest for fundamental research and technological applications. Of particular interest are magnetic non-volatile memories formed from synthetic antiferromagnetic racetrack nanowires in which chiral composite domain walls (DWs), that act as data bits, can be efficiently moved by current pulses. However, overcoming the trade-off between energy efficiency, namely a low threshold current density and high thermal stability, remains a major challenge for developing integrated chips with high reliability and low power consumption. In this thesis, we experimentally show that chiral domain walls in a synthetic antiferromagnet (SAF) -ferromagnet (FM) lateral junction, formed by local plasma oxidation, are highly stable against large magnetic fields, whilst the domain walls can be efficiently moved across the junction by current. Our new approach takes advantage of field-induced global energy barriers in the engineered energy landscape of the junction that are added to the local energy barrier. One of our most important results is that we demonstrate that thermal fluctuations are energetically equivalent to a magnetic field effect, thereby, increasing the energy barrier, and further stabilizing the DW in the junction at higher temperatures, which is in sharp contrast with conventional FMs or SAFs. We find that the threshold current density can be effectively decreased by tilting the junction's angle across the racetrack while keeping a high domain wall stability. Furthermore, we demonstrate that our approach can effectively create nanoscopic domain bits which is the key element for the racetrack memory technology. To achieve this, we created a novel structure wherein a FM region is spatially confined between adjacent SAF regions and confirmed that a magnetic bit can efficiently formed and shifted.

This thesis clearly shows how the aforementioned trade-off between efficiency and stability can be broken which will guide the future development of reliable DW-based memory, logic, and beyond.

Contents

Acknowledgements	iii
Abstract.....	vi
Contents	vii
List of figures.....	x
List of tables.....	xiv
Abbreviations	xv
1. Introduction.....	1
1.1 Magnetic domain walls for racetrack memory	1
1.2 Motivation	5
1.3 Scope of the thesis	8
2. Background	9
2.1 Magnetic domains and domain walls	9
2.1.1 Bloch and Néel type domain walls	11
2.1.2 Domain wall profile in nanowires	12
2.2 Domain wall energy	14
2.2.1 Ferromagnet.....	14
2.2.1.1 Dzyaloshinskii-Moriya interaction	15
2.2.2 Synthetic antiferromagnet (SAF)	17
2.2.2.1 Ruderman-Kittel-Kasuya-Yosida interaction	18
2.3 Domain wall dynamics	20
2.3.1 Field-induced domain wall motion.....	20
2.3.2 Current-induced domain wall motion.....	24
2.3.2.1 Spin-transfer torque	24
2.3.2.2 Spin-orbit torque	26
2.3.2.3 Exchange coupling torque.....	31
2.3.3 Thermally-induced domain wall motion	34
2.3.3.1 Energy barrier of domain wall motion.....	35
2.3.3.2 Electrical current fluctuations	36
2.3.3.3 Magnetic field fluctuations	38
3. Experimental methods.....	39

3.1 Film deposition and characterization	39
3.1.1 Magnetron sputtering.....	39
3.1.2 Vibrating sample magnetometry	41
3.2 Device fabrication	42
3.2.1 Lithography	42
3.2.2 Ion-beam etching/deposition	44
3.3 Detection of magnetic domain wall motion	46
3.3.1 Magneto-Optical Kerr Effect.....	46
3.3.2 Differential Kerr microscopy	49
3.3.3 Measurement of domain wall velocity	51
4. Experimental results	53
4.1 Magnetic properties of ferromagnets and synthetic antiferromagnets	53
4.2 Effect of oxidation on the magnetic properties of synthetic antiferromagnets	56
4.3 Synthetic antiferromagnet-ferromagnet lateral junctions	59
4.3.1 Fabrication of SAF-FM junction in racetrack nanowire	60
4.3.2 Field-induced deterministic domain wall initialization	61
4.4 Current-induced domain wall motion in SAF-FM lateral junctions	64
4.4.1 Ferromagnet region	64
4.4.1.1 Domain wall motion in flow regime.....	64
4.4.1.2 Domain wall motion in thermally assisted regime	68
4.4.2 Synthetic antiferromagnet region	70
4.4.2.1 Domain wall motion in flow regime.....	70
4.4.2.2 Domain wall motion in thermally assisted regime	73
4.4.3 SAF- FM junction.....	75
4.4.3.1 Domain wall injection in flow regime	75
4.4.3.2 Domain wall injection in thermally assisted regime.....	79
4.4.3.3 Junction angle dependent domain wall injection	81
4.5 Field-induced domain wall motion in SAF-FM lateral junctions	85
4.5.1 Ferromagnet region	85
4.5.1.1 Domain wall depinning in thermally assisted regime.....	85
4.5.2 Synthetic antiferromagnet region	87
4.5.2.1 Domain wall depinning in thermally assisted regime.....	87
4.5.3 SAF-FM junction.....	90
4.5.3.1 Domain wall injection in thermally assisted regime.....	90
5. Discussions	92

5.1 Oxidation state of upper magnetic layer of synthetic antiferromagnet multilayers	92
5.1.1 X-ray photoemission spectroscopy depth-profile analysis	93
5.2 Transition region in SAF-FM lateral junctions	96
5.2.1 Vertical and lateral structure formation.....	96
5.3 Determination of energy barriers for the domain wall motion.....	98
5.3.1 Energy barriers derived from current-induced domain wall motion	98
5.3.2 Energy barriers derived from field-induced domain wall motion	102
5.3.3 Comparison of energy barriers in current- and field-induced domain wall motion	104
5.4 Two energy barriers in SAF-FM lateral junctions	106
5.4.1 Field-induced energy landscape for domain wall.....	106
5.4.2 Determination of field-induced energy landscape in synthetic antiferromagnet.....	109
5.4.3 Local and field-induced global energy barriers at the junction	111
5.4.4 Junction tilting angle dependent energy barrier at the junction	113
5.5 Thermal stability of domain wall in SAF-FM lateral junctions	117
5.5.1 Thermally-induced domain wall depinning at the junction.....	117
5.5.2 Effect of electrical current fluctuations on domain wall depinning	121
5.5.3 Temperature dependent energy barriers for domain walls	123
5.5.4 Extremely high thermal stability of domain wall in SAF-FM-SAF bi-junctions.....	129
6. Conclusion and perspectives	131
Appendix A.....	134
A.1 Deterministic multi-DW injection.....	135
A.2 Determination of DW injection across the SAF-FM junction.....	137
A.3 Evaluation of pulsed magnetic fields	139
Bibliography	140
Curriculum vitae.....	153
Publications	154
Patent applications.....	155
Conference contributions	156

List of figures

Figure 1.1. Concept of racetrack memory	2
Figure 1.2. Evolution of racetrack memory	3
Figure 2.1. Domains and domain wall in ferromagnet	9
Figure 2.2. Bloch and Néel type domain wall	11
Figure 2.3. Domain wall profile in ferromagnet nanowire	12
Figure 2.4. Domain wall profile in synthetic antiferromagnet nanowire.....	13
Figure 2.5. Energy contributions to domain wall in ferromagnet nanowire.....	14
Figure 2.6. Illustration of Dzyaloshinskii-Moriya interaction.....	15
Figure 2.7. Energy contributions to domain walls in synthetic antiferromagnet nanowire.....	17
Figure 2.8. Oscillatory Ruderman-Kittel-Kasuya-Yosida exchange interaction.....	18
Figure 2.9. Field-induced torques on magnetization	21
Figure 2.10. Field-induced domain wall motion.....	23
Figure 2.11. Spin-transfer torque induced domain wall motion	26
Figure 2.12. Illustration of spin Hall effect and anomalous Hall effect	27
Figure 2.13. Spin-orbit torque driven by spin Hall effect.....	29
Figure 2.14. Illustration of exchange coupling torque in anti-parallel coupled moments	31
Figure 2.15. Exchange coupling torque induced domain wall motion in synthetic antiferromagnet.....	32
Figure 2.16. Moment compensation dependent domain wall velocity in synthetic antiferromagnet.....	33
Figure 2.17. Illustration of thermally-induced domain wall motion.....	34
Figure 2.18. Intrinsic energy barrier of STT-driven domain wall motion.....	35
Figure 3.1. Magnetron sputtering deposition.....	40
Figure 3.2. Schematic illustration of vibration sample magnetometer	41
Figure 3.3. Electron beam lithography system and patterned racetrack nanowire	43
Figure 3.4. Incident angle dependent ion-beam etching profile and secondary-ion mass spectrometry.....	44
Figure 3.5. Schematic illustrations of racetrack device fabrication process flow	45
Figure 3.6. Magneto-Optical Kerr effect	47
Figure 3.7. Kerr microscope setup.....	50

Figure 3.8. Exemplary differential Kerr microscopy images of domain wall motion.....	52
Figure 4.1. M - H hysteresis loops of single layer FM structure	54
Figure 4.2. Magnetic easy-axis hysteresis loop of SAF structure.....	55
Figure 4.3. Effect of oxidation process upon the SAF structure.....	56
Figure 4.4. Comparison of magnetic properties between oxidized SAF and as-grown FM....	57
Figure 4.5. Schematic illustrations of working principle of SAF-FM lateral junction.....	59
Figure 4.6. SAF-FM lateral junction fabrication process flow	60
Figure 4.7. Field-induced deterministic DW initialization	62
Figure 4.8. Demonstration of CIDWM in FM, SAF, and SAF-FM junction	63
Figure 4.9. Current density dependence of the DW velocity in the FM region.....	65
Figure 4.10. Pulse length dependence of the threshold current density for flow DW motion in the FM region.....	66
Figure 4.11. DW depinning probability versus applied current density in the FM region	68
Figure 4.12. Pulse length dependence of the threshold current density for thermally assisted DW depinning in the FM region.....	69
Figure 4.13. Current density dependence of the DW velocity in the SAF region	71
Figure 4.14. Pulse length dependence of the threshold current density for flow DW motion in the SAF region	72
Figure 4.15. DW depinning probability versus applied current density in the SAF region	73
Figure 4.16. Pulse length dependence of the threshold current density for thermally assisted DW depinning in the SAF region	74
Figure 4.17. DW motion in the SAF-FM lateral junction.....	76
Figure 4.18. DW injection (FM \rightarrow SAF) probability versus applied current density in flow regime	77
Figure 4.19. Pulse length dependence of the threshold current density for DW injection (FM \rightarrow SAF) in flow regime	78
Figure 4.20. DW injection (FM \rightarrow SAF) probability versus applied current density in thermally assisted regime	79
Figure 4.21. Pulse length dependence of the threshold current density for DW injection (FM \rightarrow SAF) in thermally assisted regime	80
Figure 4.22. SAF-FM lateral junction with junction tilting angle	81
Figure 4.23. Field-induced domain wall initialization at tilted junction.....	82

Figure 4.24. Junction angle dependence of pulse length versus the threshold current density for DW injection (FM \rightarrow SAF) in flow regime.....	83
Figure 4.25. Junction angle dependence of pulse length versus the threshold current density for DW injection (FM \rightarrow SAF) in thermally assisted regime	84
Figure 4.26. Field-induced DW depinning in the FM region	86
Figure 4.27. Field-induced DW depinning in the SAF region.....	88
Figure 4.28. Comparison of field-induced DW motion in the FM and SAF region.....	89
Figure 4.29. Field-induced DW injection (FM \rightarrow SAF) probability versus τ_H^P at various junctions.....	91
Figure 5.1. XPS profile of atomic concentrations of elements with etching time.....	94
Figure 5.2. XPS spectra of Co and Ni at different etching times.....	95
Figure 5.3. Atomic force microscopy (AFM) images of SAF-FM junction ($\theta_j = 0^\circ$) in a racetrack.....	96
Figure 5.4. Cross-sectional transmission electron microscopy (TEM) image of SAF-FM junction	97
Figure 5.5. Threshold current density as a function of pulse length in FM, SAF, and FM \rightarrow SAF ($\theta_j = 0^\circ$)regions	99
Figure 5.6. Energy landscape of DWs in SAF-FM junction ($\theta_j = 0^\circ$).....	101
Figure 5.7. Threshold field as a function of pulse length in FM and SAF regions.....	103
Figure 5.8. Comparison of current- and field-induced DW energy barriers.....	104
Figure 5.9. Illustration of DW depinning and energy landscapes for $\uparrow\downarrow$ DW configuration for the FM and SAF cases.	107
Figure 5.10. Illustration of the field-induced energy landscape for $\uparrow\downarrow$ DW configuration (LM) in the SAF	109
Figure 5.11. Illustration of field-induced energy landscapes and global energy barriers for $\uparrow\downarrow$ domain walls in a SAF-FM junction.....	111
Figure 5.12. Junction tilting angle dependent DW injection threshold current density in the flow regime	113
Figure 5.13. Junction tilting angle dependent DW injection energy barriers	115
Figure 5.14. Domain wall injection into tilted SAF-FM junctions.....	116
Figure 5.15. Illustration of thermal fluctuation torques depending on the DW position in FM-SAF junction.....	119

Figure 5.16. Illustration of electrical current density fluctuation induced by thermal energy in equilibrium.....	121
Figure 5.17. Temperature dependent current-induced DW depinning and energy barriers ..	124
Figure 5.18. Illustration of temperature dependent energy landscapes induced by thermal fluctuation fields H_{fl}	125
Figure 5.19. SAF-FM-SAF lateral bi-junctions	129
Figure 5.20. Demonstration of field stability of SAF-FM-SAF lateral bi-junction.....	130

List of tables

Table 3.1. List of e-beam and photoresists and corresponding process conditions.....	42
Table 5.1. Quantities measured from experiment and estimated from thermal fluctuations for FM, SAF and SAF-FM junction	126

Abbreviations

DW	Domain wall
SAF	Synthetic antiferromagnet
FM	Ferromagnet
CIDWM	Current-induced domain wall motion
RTM	Racetrack memory
HDD	Hard disk drive
MRAM	Magnetic random-access memory
STT	Spin-transfer torque
PMA	Perpendicular magnetic anisotropy
DMI	Dzyaloshinskii-Moriya exchange interaction
SOT	Spin-orbit torque
ECT	Exchange coupling torque
MTJ	Magnetic tunnel junction
AF	Antiferromagnet
UM	Upper magnetic layer
LM	Lower magnetic layer
SOC	Spin-orbit coupling
RKKY	Ruderman- Kittel-Kasuya-Yosida
LLG	Landau-Lifshitz-Gilbert

FIDWM	Field-induced domain wall motion
SHE	Spin Hall effect
AHE	Anomalous Hall effect
NM	Non-magnetic
MANGO	Multi- source, atomically engineered, next generation, alloys and compounds
HM	Heavy metal
XRR	X-ray reflectivity
VSM	Vibrating sample magnetometer
EBL	E-beam lithography
SEM	Scanning electron microscope
IBE / IBD	Ion-beam etching / Ion-beam deposition
SIMS	secondary-ion mass spectrometry
MOKE	Magneto-optical Kerr effect
MO	Magneto-optical
RIE	Reactive ion etching
XPS	X-ray photoemission spectroscopy
AFM	Atomic force microscopy
TEM	Transmission electron microscopy
TMAH	Tetramethylammonium hydroxide
FIB	Focused ion beam

Chapter 1 Introduction

1.1 Magnetic domain walls for racetrack memory

A magnetic domain wall (DW) is a boundary between magnetic domains with magnetizations oriented along distinct directions. On the nanoscale, such DWs behave like nano-objects with mass and momentum [1]. These distinct nano-objects can form magnetic bits in memory and logic devices [2]–[4]. Decades ago, magnetic bubble memory was a mainstream technology in which micron-sized magnetic bubbles were cleverly manipulated by local and global magnetic fields [5]. The recent discoveries[6]–[8] of several distinct current-induced torques that can be employed to manipulate DWs have made possible the potential realization of high-performance magnetic memory and logic devices based on the creation and motion of DWs in magnetic nano-wires, namely racetracks [9]–[12].

On the basis of the phenomenon of current-induced DW motion (CIDWM), the Racetrack Memory (RTM) concept was first proposed by Prof. Dr. Stuart Parkin in 2002 [13], as an innately three-dimensional magnetic storage device that promises a non-volatile solid-state memory with high density even beyond magnetic random-access memories (MRAMs) and even beyond conventional magnetic hard disk drives (HDDs). The information in a RTM is stored in a magnetic nano-wire track where a series of magnetic domains are formed. The corresponding DWs between each domain can be shifted along the wire by passing an electrical current through the wire, thus making possible a shift register.

Key to these devices is the efficiency and stability of the manipulation of DWs within the racetracks. Regarding efficiency, there have been four major developments over the past 2 decades that have made possible extremely efficient CIDWM and very large storage capacities (see Fig.1.2) [3].

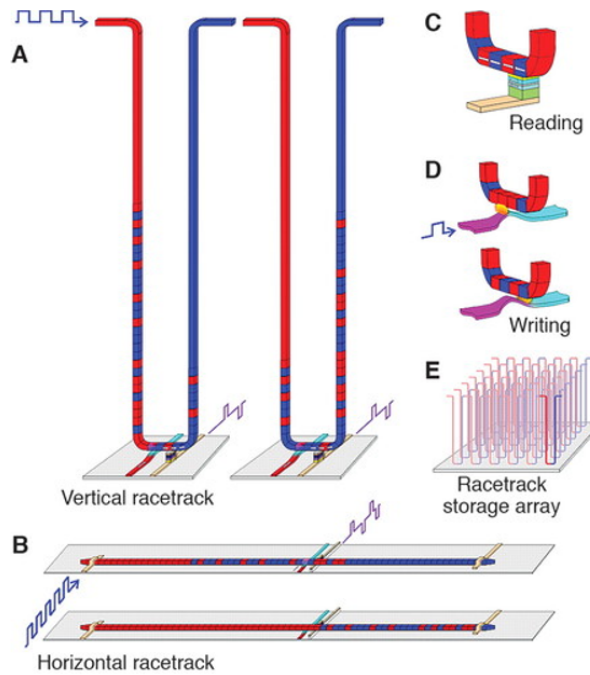


Figure 1.1. Concept of racetrack memory. (a) Three-dimensional racetrack memory (RTM) composed of U-shape vertical magnetic nanowire. (b) Two-dimensional RTM with straight magnetic nanowire. (c, d) Read and write operations in RTM. Data (magnetic domains) in RTM is read by a magnetic tunnel junction (c) and written by stray fields arising from a separate crossing magnetic line (d). (e) High density RTM storage array. Figure is adopted from [2] with permission from American Association for the Advancement of Science.

The first concept of RTM was demonstrated in in-plane magnetized permalloy wires (RTM 1.0) [14], [15]. In RTM 1.0, the DW moves along the electron flow direction (opposite to the applied current flow direction) since the underlying mechanism for current induced motion is based on the phenomenon of spin-transfer torque (STT) [16]–[19]. Due to the shape anisotropy in soft magnets such as permalloy the easy axis of magnetization is restricted to an in-plane orientation along the wire so that the minimum domain size is physically limited. The DW configuration in such a thin layer favors the formation of a Bloch-type DW structure which are innately very large since they result from a competition between the Heisenberg nearest neighbor ferromagnetic exchange interaction and long-range magnetostatic forces.

DWs can be shrunk in size to useful dimensions by introducing materials that exhibit a strong perpendicular magnetic anisotropy, such as in Co/Ni superlattices formed with atomically thin Co and Ni sub-layers. The Co/Ni interfaces give rise to a very strong interfacial perpendicular magnetic anisotropy (PMA) in which the net magnetization is aligned perpendicular to the film plane [20], [21]. This category of materials led to RTM 2.0 with

promising high domain walls capacities inside the racetrack wires. The STT-driven DW motion efficiency in RTM 2.0 is similar to that in RTM 1.0. Thus, DWs move in the same direction (electron flow direction) and the roughly at the same velocity for the same current density [22], [23].

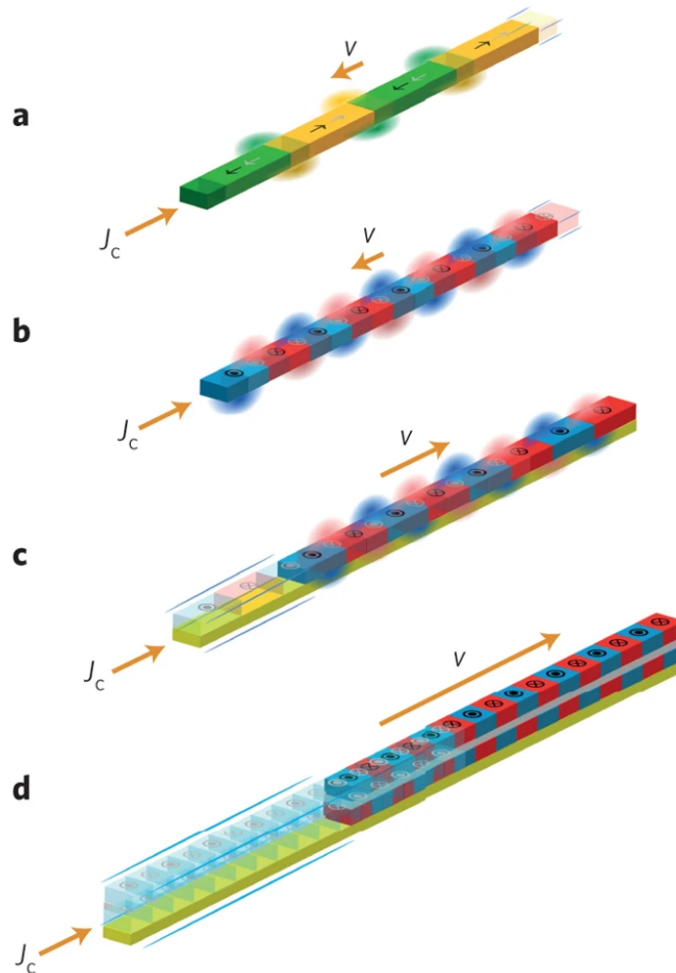


Figure 1.2. Evolution of racetrack memory. (a) RTM 1.0, with in-plane magnetized ferromagnet (FM) nanowire. (b) RTM 2.0, with perpendicularly magnetized (easy axis along out-of-plane) FM nanowire. CIDWM in both RTM 1.0 (a) and 2.0 (b) is based on conventional spin-transfer torque. Thus, the DW moves opposite to the current flow direction (electron flow). (c) RTM 3.0, with spin-orbit torque driven CIDWM. Néel DW moves along the current flow direction with high velocities due to the chiral spin torque. (d) RTM 4.0, with synthetic antiferromagnet which is composed of antiferromagnetically coupled two sub-FMs. Novel giant exchange coupling torque significantly enhances the DW motion efficiency. Note that the fringing field from RTM nanowire is completely suppressed in RTM 4.0 contrary to others (a-c). Figure is adopted from [3] with permission from Springer Nature.

In 2011 highly efficient DW motion was first experimentally demonstrated in a perpendicularly magnetized ultrathin cobalt layer deposited on a platinum layer in which the DW velocity reaches up to 400 m/s [24]. More interestingly, the DW moves along the current flow direction, which is opposite to that found for RTM 1.0 and RTM 2.0. The origin of such a novel DW motion turned out to be derived from a strong spin-orbit coupling phenomenon at the interface between the magnetic layers and a heavy metal underlayer or overlayer [6], [25]. Due to the broken inversion symmetry at these interfaces, a Dzyaloshinskii-Moriya exchange interaction (DMI) [26], [27] gives rise to an antisymmetric exchange energy between neighboring moments across the DW, thus stabilizing the DW in a chiral Néel-type structure [28]. Furthermore, in addition to DMI, the discovery of spin-orbit torques (SOTs) [29]–[31], that originate from a spin Hall effect (SHE) in adjacent heavy metal layers, considerably boosts the efficiency of the current-induced chiral DW motion [32]. Consequently, the combination of such interfacial spin-orbit coupling-based phenomena, including DMI and SOT, paved the way for novel chiral spintronics, thus allowing DWs to be moved by chiral spin torques in RTM 3.0.

Despite the greater efficiency of current-induced chiral DW motion in RTM 3.0, a high density of DWs in the racetrack is needed for achieving large-capacity memory devices. Due to the demagnetizing fields from each DW arising from ferromagnets (FMs) such as Co/Ni multilayers, there is an undesirable interaction between neighboring DWs along and even between adjacent racetracks. This can potentially degrade the performance of the RTM when integrated at the chip level scale. To overcome this issue, RTM 4.0 was recently developed by using synthetic antiferromagnets (SAFs) as host materials for the DWs [8]. The SAF is formed from two perpendicularly magnetized sub-magnets, which are antiferromagnetically coupled through an ultrathin ruthenium spacer layer [33]–[35]. In the SAF the DWs are always formed in each sub-magnetic layer as a pair which are mirror images of the other. Thus, the demagnetizing fields from the DWs (and the corresponding domains) can be tuned to be close to zero. More surprisingly, the CIDWM in such SAFs was found to be highly efficient, with a velocity exceeding 1000 m/s. This originates from a novel exchange coupling torque (ECT) in addition to the chiral SOT, and such efficiency can be further improved by tuning the strength of the AF coupling and the net moment compensation [8], [36]. In consequence, the discovery of highly efficient DW motion in RTM 4.0 led to the emergence of chiral AF spintronics, as well as bringing RTM to mainstream platforms.

1.2 Motivation

Despite the remarkable progress in the efficiency of CIDWM, the stability of DWs against external stimuli, such as thermal fluctuations, has not yet been explicitly investigated so far. Up to date, only few experimental demonstrations have discussed the thermal stability of DWs [37]–[41]. To consider a DW as a data-bit in RTM, the DW position along the nanowire must not be shifted over time by thermal agitation that is one of the most critical factors of magnetic memory devices. Therefore, achieving a high thermal stability of DWs is key to success of RTM. In case of conventional MRAMs, for instance, the thermal stability of magnetic tunnel junctions (MTJs) can be evaluated by obtaining the thermal stability factor $\Delta = \frac{E_b}{k_B T}$ (E_b is energy barrier between two stable states, and k_B is the Boltzmann constant) at finite temperature T [42], [43]. Also, it is widely known that $\Delta > 40$ of MTJ is required to guarantee the data retention of ten years at room temperature [44]. The E_b is mainly proportional to the saturation magnetization, volume and anisotropy energy, so that it can be measured by current- or field-induced switching of two states (parallel \leftrightarrow anti-parallel) in thermally activated regime [45]–[47]. In general, the high thermal stability in MTJ accompanies a large threshold current (or field) for switching, thus achieving both high stability and high energy efficiency remains a major challenge.

Such trade-off is common for other non-volatile magnetic memory devices as well as RTM. Moreover, the correlation between E_b and the threshold current (or field) for DW motion still has not yet been clearly established [48], which is contrast to MTJ. Therefore, overcoming aforementioned trade-off seems to be more difficult, but, in one side, there are still more rooms to manipulate compared to MTJs.

In 2013, for instance, Kim *et al.* [39] experimentally revealed that the STT-driven DW (RTM 2.0) is governed by two different energy barriers, so called an intrinsic [49] and an extrinsic barrier, depending upon the current- and field-induced motion, respectively. At the same time, it was understood that the energy barrier that is relevant for thermal stability is the field-induced depinning barrier rather than that induced by current, although this has not yet been further demonstrated in experiments. Nevertheless, this finding provided an important clue that how to achieve both lower J_{th} with a high Δ of DW by separating two energy barriers.

On the other hand, for the case of DW depinning by SOT, the current and field depinning barriers are found to be nearly identical, since there is no intrinsic pinning for SOT [32], [38]. As a result, the energy barrier of SOT-driven DW is solely governed by external pinning. Despite such fundamental challenges, it is essential to find a new means whereby the J_{th} in SOT is low while the field energy barrier is high [6], [7], [48].

In this thesis, we present a novel approach to resolve a critical challenge in RTM – improving thermal stability whilst lowering the J_{th} . We note that J_{th} and the field-stability are proportional to the respective energy barrier densities to overcome the displacement of a DW from its static state. Since it is understood that the corresponding energy barriers are linearly proportional to the effective volume of the DW [40], if we can decrease the energy barrier with respect to the effective DW volume on which the current-driven torque is applied and, at the same time, whilst increase the energy barrier compared to the effective volume on which the field-torque is applied, we can overcome such a trade-off.

Here we resolve this problem by forming a novel lateral junction between a SAF (RTM 4.0) and a FM (RTM 3.0) [50]. To realize this, we employ two novel concepts into the standard SAF racetracks. First, by locally oxidizing the upper FM layer of SAF to make it into non-magnetic, we create lateral SAF-FM junction, in which the lower FM layer is common to both. Secondly, the moment in the upper FM layer is designed to be slightly larger than that of the lower FM layer. In this junction, we demonstrate that the field driven torque is dominated by the unconventional energy landscape, namely field-driven global energy barrier, that tightly binds the DW to neighbouring large volume of domains, while the current driven torque, by contrast, is dominated by a conventional local energy barrier defined by the DW itself. Consequently, this structure effectively traps the DW at the boundary so that depinning the DW by external fields is impossible when the field is lower than saturation field. Furthermore, this structure makes it possible for us to clearly demonstrate from temperature-dependent experiments that thermal effects indeed give rise to corresponding fluctuating magnetic fields. We also show from these experiments that the global energy barrier indeed increases significantly with increasing temperature. As a consequence, our experiments clearly prove that the thermal effects are equivalent to the field effects rather than the current fluctuation in DWs.

Moreover, the junction is also fabricated so that the boundary between the SAF and FM regions is tilted by a junction angle with respect to the direction of DW motion. We show that

the tilted junction significantly reduces J_{th} by reducing the effective volume of the magnetic domain in the upper FM layer that has to be switched, whilst the field-stability of DW is unchanged regardless of shape of junction.

Furthermore, by extending single junction concept to a SAF-FM-SAF bi-junction we demonstrate that a DW can be robustly confined within the FM region that is laterally sandwiched between SAF regions so that the DW is stable against arbitrary magnetic fields whose magnitude is smaller than the spin-flop field of the individual SAF domains, while, at the same time the DW can be efficiently injected from the FM into the SAF regions by current.

1.3 Scope of the thesis

This thesis is structured as follows. First, the fundamental backgrounds for the basic magnetism of thin films, in particular the perpendicularly magnetized FM and SAF, are introduced in chapter 2. Chapter 2 also covers the DW dynamics, including the underlying mechanisms of current-, and field-induced DW motion, and corresponding energy barriers.

In chapter 3, we present the experimental steps and detailed methods that were employed in this study.

Afterwards, the experimental results of the current- and field-induced DW motion in SAF-FM junction integrated racetrack are shown in chapter 4.

More detail discussions with qualitative and quantitative analysis about the experimental results are provided in chapter 5. In particular, this discussion focuses on the evaluation of temperature dependent energy barriers of DW in each FM, SAF, and SAF-FM junction.

Lastly, we summarize this study and discuss the perspectives for future experiments in chapter 6.

Chapter 2 Background

In this chapter, we briefly introduce the fundamentals of magnetic domain walls and its dynamics in atomically thin ferromagnet and synthetic antiferromagnet system. The strong interfacial spin-orbit coupling between transition metal magnets, and non-magnetic heavy metal layers gives rise to the exotic novel magnetic and electrical properties, thereby leading to a highly efficient chiral magnetic domain wall motion. The underlying mechanisms of such domain wall motion is discussed by comparing three different external stimuli, including magnetic fields, electrical currents, and thermal fluctuations. Furthermore, we discuss the energy barrier that is correlated to the threshold condition and thermal stability of domain wall motion as well.

2.1 Magnetic domains and domain walls

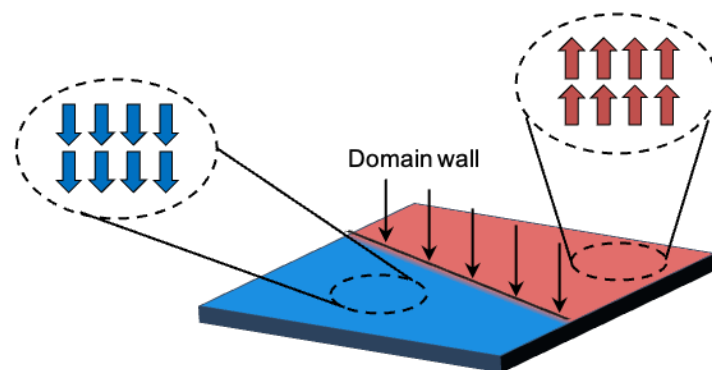


Figure 2.1. Domains and domain wall in ferromagnet with perpendicular magnetic anisotropy. Ferromagnetic (FM) domains are aligned in downwards (blue) and upwards (red), respectively. Each colored arrow represents the magnetization of FM. The boundary between domains (black line and arrows) indicates the domain wall.

Magnet is widely used in our daily life for various purposes. For instance, the development of magnetic hard disk drives (HDDs) composed of ferromagnets (FMs), allows to drastically increase the capacities of data storage over the decades [51]–[53]. Here the

magnets, including FM and antiferromagnet (AFM), exhibits an ordering of magnetic moments that originates from the spin and orbital momentum of the electrons that are based on the quantum mechanical phenomenon [54], [55]. In FMs, magnetizations are collectively aligned to all same direction that is determined by the strong exchange energy between neighboring atoms [56]. In reality, however, a length scale of such ordering is not infinite, but is limited by size of from few hundreds of nanometers to even beyond micrometers scale. Such region where the magnetization is uniformly aligned is called magnetic domains (Fig. 2.1). The formation of multi magnetic domains in FM is a consequence of the minimization of the total magnetostatic energy E_{tot} that can be described by [57]

$$E_{tot} = E_{ex} + E_K + E_d + E_Z + E_{stress} + E_{ms} \quad (2.1)$$

where E_{ex} is an exchange energy, E_K is a magnetocrystalline anisotropy energy, E_d is a demagnetizing energy, E_Z is Zeeman energy, E_{stress} is a stress energy, and E_{ms} is a magnetostriction energy, respectively. In general, the last three terms can be negligible in static state which does not take into account any external stimuli. Here, the boundary between two domains which are aligned differently to each other is called a magnetic domain wall (DW).

2.1.1 Bloch and Néel type domain walls

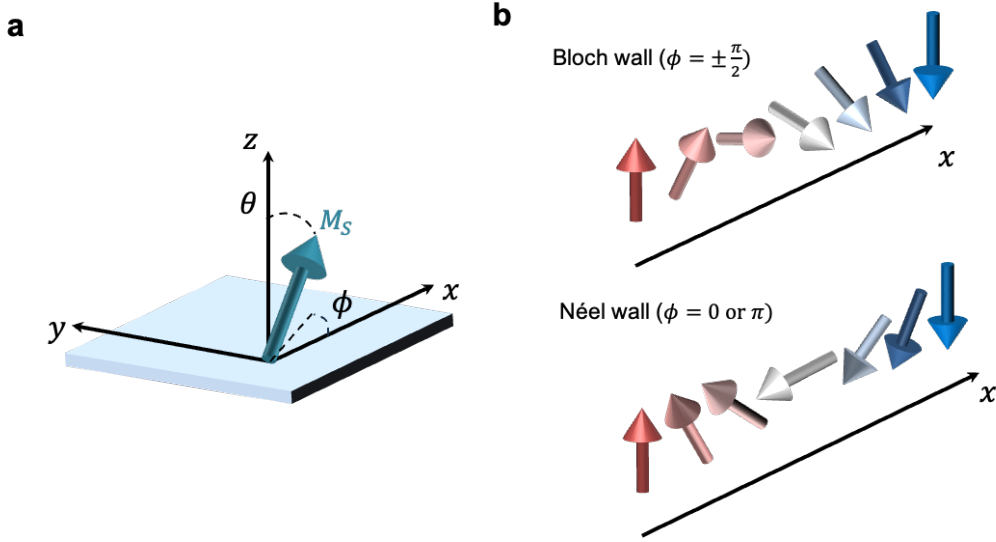


Figure 2.2. Bloch and Néel type domain wall. (a) Magnetization in spherical coordinate system. (b) Bloch (upper panel) and Néel type (lower panel) domain wall in perpendicularly magnetized FM (easy-axis along z-direction). Note that the DW plane is in yz-plane.

Magnetic DWs can be formed in various types depending upon the crystal structure, thickness, as well as a shape of magnetic materials since they lead to the change E_{tot} of the corresponding system. In this thesis, we mainly focus on the dynamics of Bloch and Néel type walls in perpendicularly magnetized FM thin film system which exhibit a narrow transition region between domains. Both Bloch and Néel wall, can be readily represented by one-dimensional (1D) model in a spherical coordinate system [5], [58], [59] with a magnetization $\mathbf{M} = M_S(\sin \theta \cos \phi, \sin \theta \sin \phi, \cos \theta)$, where M_S is the magnitude of saturation magnetization, θ is the polar angle, and ϕ is the azimuthal angle, respectively (Fig 2.2a). In a Bloch wall, the magnetization of the wall \mathbf{M}_{DW}^{Bloch} lies along the DW plane with $\phi = \pm \frac{\pi}{2}$ (yz-plane), which is perpendicular to the magnetization rotation axis, whereas the magnetization of the Néel wall $\mathbf{M}_{DW}^{Néel}$ points along the direction of rotation axis with $\phi = 0$ or π (x-axis) which is in perpendicular to the DW plane (Fig. 2.2b).

2.1.2 Domain wall profile in nanowires

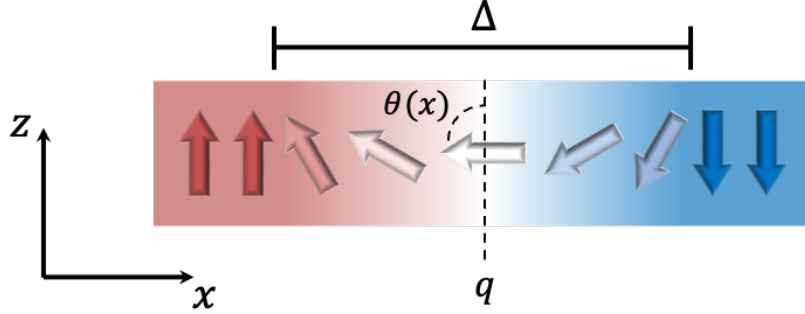


Figure 2.3. Domain wall profile in ferromagnet nanowire. Néel type domain wall of width Δ in perpendicularly magnetized nanowire. The magnetization rotates in $\theta(x)$ along x -direction from up (\uparrow) to down (\downarrow). The center of domain wall is denoted by the position $x = q$ with $\theta(q) = \frac{\pi}{2}$.

The profile of DW in FM nanowire with respect to its position can be described in 1D model (Fig. 2.3). It is derived by the minimizing the total energy of DW E_{tot} which only takes into account exchange and anisotropy energy terms and that can be generally presented by [60]

$$\theta_{FM}(x) = 2 \tan^{-1} \left[\exp\left(\pm \frac{x - q}{\Delta}\right) \right] \quad (2.2)$$

where q is the position of DW along x -axis, and Δ is the DW width parameter, respectively. Note that the Δ is determined by the intra-layer exchange stiffness A_{ex} , and the effective anisotropy K_{eff} parameters ($\Delta = \sqrt{A_{ex}/K_{eff}}$). Here + or - sign in Eq. 2.2 represents the DW which forms in between either $\uparrow\downarrow$ ($\odot|\otimes$) or $\downarrow\uparrow$ ($\otimes|\odot$) domain configuration.

Let us assume the DW in synthetic antiferromagnets (SAFs) nanowire where the two FM layers are antiferromagnetically coupled via atomically thin non-magnetic spacer layer. In a SAF, a pair of DWs are tightly bound to each other due to the interlayer exchange coupling

through spacer layer so that they behave like a single DW in FM. Thus, the profile of each DW in SAF can be described by [8], [59]

$$\theta_{SAF}^{UM}(x) = 2 \tan^{-1} \left[\exp \left(\pm \frac{x - q_{UM}}{\Delta_{UM}} \right) \right] \quad (2.3)$$

$$\theta_{SAF}^{LM}(x) = 2 \tan^{-1} \left[\exp \left(\mp \frac{x - q_{LM}}{\Delta_{LM}} \right) \right] \quad (2.4)$$

where UM and LM represent to upper magnetic and lower magnetic sub-FM layers, respectively. Note here that the signs of DW profile in UM and LM of SAF are opposite to each other due to the AF coupling. Furthermore, we consider that the position of two DWs is always identical by assuming a strong coupling strength [61].

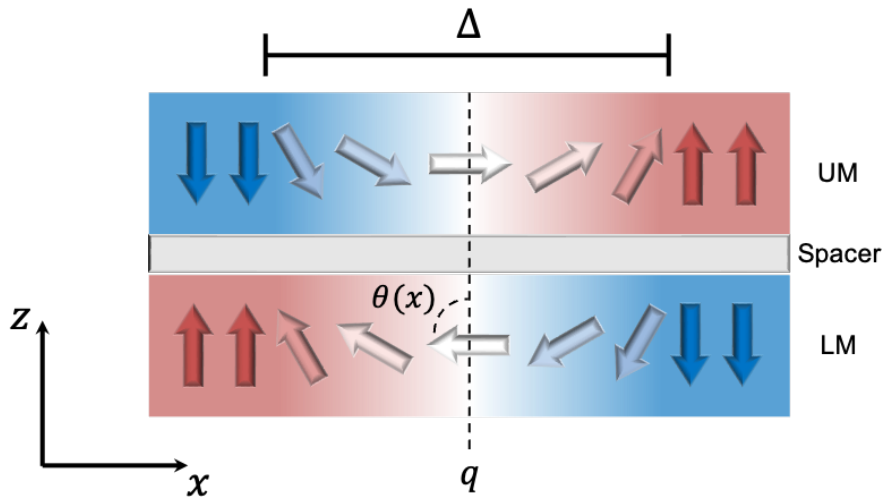


Figure 2.4. Domain wall profile in synthetic antiferromagnet nanowire. Néel type domain wall with a width of Δ in perpendicularly magnetized synthetic antiferromagnet nanowire. The magnetizations in lower magnet (LM) and upper magnet (UM) are antiferromagnetically coupled via spacer layer. DW profiles of LM and UM exhibit always opposite sign.

2.2 Domain wall energy

Determination of preferred DW type in a given system is governed by the minimization of total energy as presented in Eq. 2.1. In this regard, a Bloch wall is generally favored in many thin film systems rather than Néel wall due to the demagnetizing energy along the DW direction [57]. In certain cases, however, a Néel wall is more stabilized [6], [7], [50] since the additional energies overcome a given demagnetizing energy likewise our study. To better understand this, it is essential to have a closer look at each energy terms that contribute to the total DW energy.

2.2.1 Ferromagnet

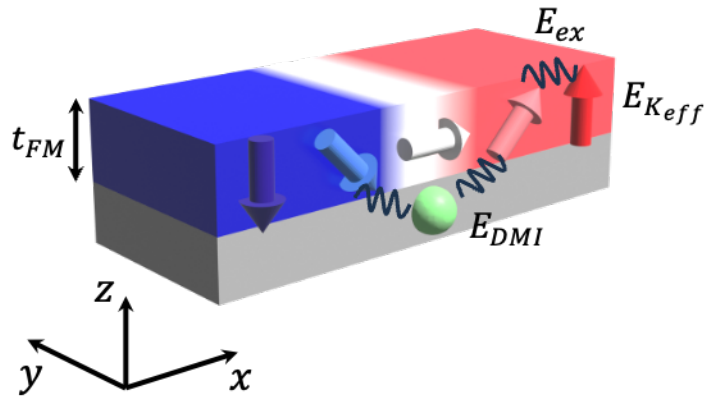


Figure 2.5. Energy contributions to domain wall in ferromagnet nanowire. Total energy terms relevant to Néel wall in perpendicularly magnetized ferromagnet nanowire. Intra-layer exchange energy E_{ex} arises from the neighboring moments in FM layer. Effective anisotropy energy $E_{K_{eff}}$ includes the magnetocrystalline and shape anisotropy. Dzyaloshinskii-Moriya interaction energy E_{DMI} arises from the interface of adjacent non-magnetic layer. The thickness of ferromagnetic layer is denoted by t_{FM} .

Let us consider a DW in a FM nanowire as shown in Fig. 2.5. The DW energy terms relevant for here are the intra-layer exchange interaction E_{ex} , the effective anisotropy energies $E_{K_{eff}}$, and the additional energy which enables to stabilize a Néel wall, so called the Dzyaloshinskii-Moriya interaction (DMI) energy E_{DMI} (Fig. 2.3) [26], [27], [32], [62]. Here the intra-layer exchange is the Heisenberg exchange between the neighboring magnetic

moments that energetically favor to align parallel to each other. Note here that the E_{ex} and $E_{K_{eff}}$ is mainly volume effects whereas the E_{DMI} originates from the interfaces. Therefore, it is relevant to describe the energy densities of each term by taking into account the width of nanowire w and the thickness of films t^{FM} , respectively. As a result, the total DW energy density of FM can be described by

$$\varepsilon_{DW}^{FM} = \varepsilon_{ex}^{FM} + \varepsilon_{K_{eff}}^{FM} + \varepsilon_{DMI}^{FM} = \frac{A_{ex}^{FM} t_{FM}}{\Delta^2} \sin^2 \theta + t_{FM} K_{eff}^{FM} \sin^2 \theta \pm \frac{D_{FM}}{\Delta} \cos \phi \sin \theta \quad (2.5)$$

where the K_{eff} is the effective anisotropy constant that is positive ($K_{eff} > 0$) for perpendicular magnetic anisotropy (PMA) system, D_{FM} is the DMI constant whose sign is determined its exchange direction, respectively. In Co/Pt case, for instance, the DMI constant is positive values ($D_{Co} \sim 0.2 \text{ pJ m}^{-2}$) [63].

2.2.1.1 Dzyaloshinskii-Moriya interaction

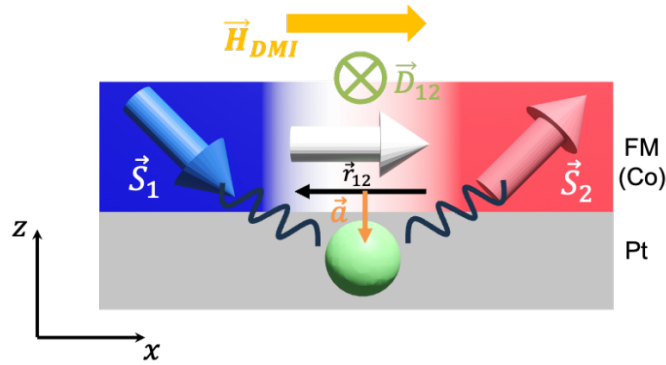


Figure 2.6. Illustration of Dzyaloshinskii-Moriya interaction. DMI is an antisymmetric exchange coupling between the spins of two ions \vec{S}_1 and \vec{S}_2 via non-magnetic ligand (green sphere). The sign of DMI vector \vec{D}_{12} and corresponding effective DMI field \vec{H}_{DMI} is determined by the geometrical configuration of \vec{S}_1 and \vec{S}_2 . \vec{r}_{12} and \vec{a} are a displacement vector from the midpoint of two adjacent spins and a distance vector, respectively.

The DMI arises from the substantial spin-orbit coupling (SOC) in the presence of broken inversion symmetry at the interface between FM and HM layers (e.g., Co/Pt interfaces) [64], [65]. In principle, the DMI is another form of indirect exchange where the interaction between spins of two magnetic ions is transferred via single third ion by a superexchange mechanism (see Fig. 2.4). Initially, this type of exchange interaction was proposed by Dzyaloshinskii [27] to explain the weak ferromagnetism in bulk α -Fe₂O₃ crystal arising from the lack of inversion symmetry based on the Landau theory. Later, Moriya found that this is a consequence of spin-orbit interactions [26]. In this regard, one particular orientation is favourable over the other, hence it is also called an antisymmetric exchange. Therefore, the DMI energy gives rise to a canting of the spins \vec{S}_1 and \vec{S}_2 and that is given by

$$E_{DMI} = \vec{D}_{12} \cdot (\vec{S}_1 \times \vec{S}_2) \quad (2.6)$$

where \vec{D}_{12} is the DMI constant vector that is proportional to DW plane vector \vec{r}_{12} and a distance vector \vec{a} ($\vec{D}_{12} = -\lambda_{SOC} \vec{r}_{12} \times \vec{a}$). Here λ_{SOC} is a coefficient proportional to the strength of SOC. As a consequence, the DMI in DWs generates a local longitudinal effective magnetic field $\vec{H}_{DMI} = -\frac{\partial E_{DMI}}{\partial \vec{M}}$ along DW direction, thereby stabilizing Néel wall against Bloch wall in the present system. One can also notice that the orientation of \vec{D}_{12} depends upon the sign of λ_{SOC} and this only allows to form opposite orientation of DWs in $\uparrow\downarrow$ ($\odot|\otimes$) or $\downarrow\uparrow$ ($\otimes|\odot$ \odot) DW configuration [66]. As a consequence, the DMI energy does not only stabilize the Néel wall but also introduce a chirality of DWs. The chirality generates the DW rotation either clockwise or counter clockwise. Apart from Co/Pt interface, in general, the DMI can also be observed in many ultrathin magnetic layers at adjacent HM which exhibits a strong SOC, for instance, Ta [7], [48], Pd [25], W[67], Hf [48], and Ir [25] as well.

2.2.2 Synthetic antiferromagnet (SAF)

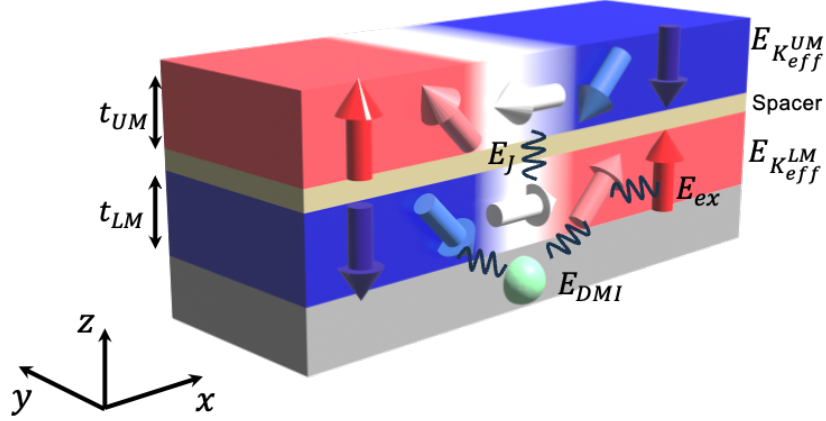


Figure 2.7. Energy contributions to domain walls in synthetic antiferromagnet nanowire. Total energy terms for a pair of Néel walls in perpendicularly magnetized each sub-ferromagnet layers (UM: upper magnetic layer, and LM: lower magnetic layer). Inter-layer exchange energy E_J via non-magnetic spacer layer contributes total domain wall energy. $E_{K_{eff}^i}$ and t_i ($i = LM$ or UM) denote the effective anisotropy energy, and thickness of sub-layer, respectively. Note that Dzyaloshinskii-Moriya interaction energy E_{DMI} is taken into account in both LM and UM.

In a SAF, there are pair of DWs in each LM and UM sub-magnetic layers that are tightly bound to one another via inter-layer exchange coupling. Considering the total DW energy in the SAF, therefore, the inter-layer exchange energy E_J must be included in addition to the energy of two DWs (Fig. 2.7). Since the total energy of individual DW in each sub-magnetic layers are identical to FM case, the total DW energy density of SAF can be described by [8], [59]

$$\begin{aligned}
 \varepsilon_{DW}^{SAF} &= \varepsilon_{ex}^{LM} + \varepsilon_{ex}^{UM} + \varepsilon_{K_{eff}}^{LM} + \varepsilon_{K_{eff}}^{UM} + \varepsilon_{DMI}^{LM} + \varepsilon_{DMI}^{UM} + \varepsilon_J \\
 &= \frac{A_{ex}^{LM} t_{LM}}{\Delta^2} \sin^2 \theta + \frac{A_{ex}^{UM} t_{UM}}{\Delta^2} \sin^2 \theta + t_{LM} K_{eff}^{LM} \sin^2 \theta \\
 &\quad + t_{UM} K_{eff}^{UM} \sin^2 \theta \pm \frac{D_{LM}}{\Delta} \cos \phi \sin \theta \mp \frac{D_{UM}}{\Delta} \cos \phi \sin \theta \\
 &\quad - J_{ex} [\cos(\phi^{LM} - \phi^{UM}) \sin^2 \theta - \cos^2 \theta]
 \end{aligned} \tag{2.7}$$

where J_{ex} is the inter-layer exchange coupling constant that indicates the strength of coupling ($|J_{ex}|$) and the type of coupling depending upon the sign; $J_{ex} > 0$ (FM) or $J_{ex} < 0$ (AFM), respectively. The sign of the DMI energy density term in LM and UM is opposite to each other due to their anti-parallel configuration. Similar to the DMI energy, the inter-layer exchange energy density ε_j originates from the interface, not from the bulk.

2.2.2.1 Ruderman-Kittel-Kasuya-Yosida interaction

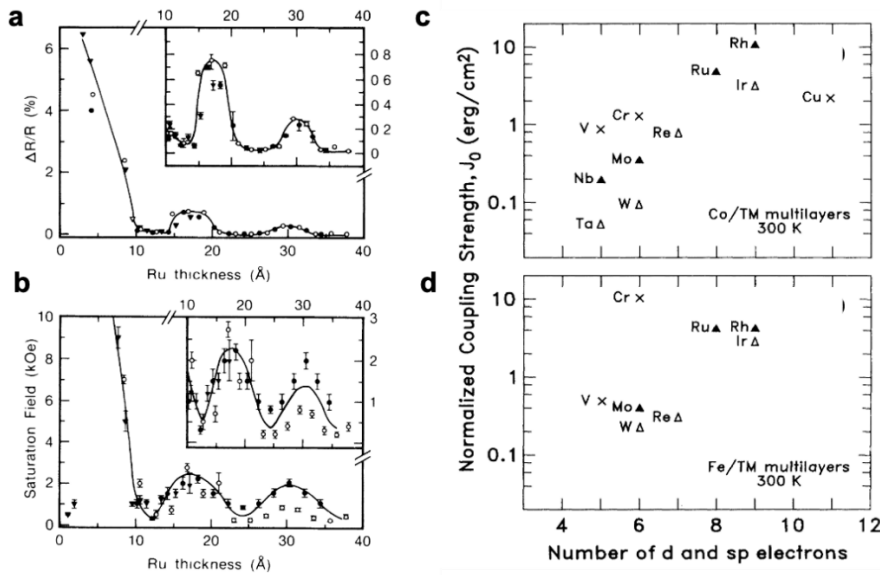


Figure 2.8. Oscillatory Ruderman-Kittel-Kasuya-Yosida exchange interaction. Ru spacer layer thickness dependent (a) transverse saturation magnetoresistance, and (b) saturation field at room temperature for Co/Ru multilayers. Oscillation period is observed about 12 Å. Normalized inter-layer exchange coupling strength J_{ex} of various spacer materials with (c) Co and (d) Fe multilayers. Figures are adopted from [33], [34] with permission from American Physical Society.

The origin of inter-layer exchange coupling is understood based on the Ruderman-Kittel-Kasuya-Yosida (RKKY) exchange interaction [68]–[70]. The RKKY interaction refers the indirect exchange of localized magnetic moments through the conduction electrons in a metal. The theory is innately based on Bloch wavefunctions so that it is only relevant to crystalline systems. Later, such exchange coupling was observed in the ultrathin magnetic

multilayer systems with insertion of non-magnetic transition metal spacer layers [33], [34]. Here it is noteworthy that the coupling exhibits the oscillation behavior as a function of the thickness of spacer layer, either they become FM or AFM coupling, and the periods of the oscillatory coupling is determined by the critical spanning vectors of the Fermi surface of spacer [71], [72]. The SAF system investigated in this thesis, for instance, the spins of the conduction electrons in ultrathin Ru spacer layer play a role of medium between magnetic moments of Co sub-layers and the thickness spacer layer is designed to be $\sim 9 \text{ \AA}$ [33], [34] as well. The corresponding exchange energy density ε_j is given by [73], [74]

$$\varepsilon_j = -J_{ex} \hat{m}^{LM} \cdot \hat{m}^{UM} \quad (2.8)$$

where \hat{m}^i ($i = LM$ or UM) is a unit vector of magnetization of LM and UM, and J_{ex} denotes the exchange coupling strength, respectively. By replacing the DW magnetization of LM and UM in Eq. 2.8, as a consequence, the inter-layer exchange energy density of DW in SAF can be written as

$$\varepsilon_j = -J_{ex} [\cos(\phi^{LM} - \phi^{UM}) (\sin^2 \theta - \cos^2 \theta)]. \quad (2.9)$$

2.3 Domain wall dynamics

In the previous session, we discuss the steady state of the DWs in FM and SAF nanowire in which there is no changes in their position by neglecting any external perturbations. In reality, however, the DW motion can be readily observed in the presence of the external magnetic fields, and even by the thermal fluctuation at finite temperature. Moreover, a discovery of the DW motion induced by an electrical current flow enables the manipulation of the DW in a controlled manner. In this session, we will discuss the DW dynamics resulting from the three different sources of the magnetic field, the electrical current, and the thermal fluctuation.

The DW dynamics can be described by the Landau-Lifshitz-Gilbert (LLG) equation [75], [76], which is a differential equation describing the time dependent angular momentum change. As the external torque exerted, the magnetization initiates the precession and the equation of corresponding motion can be simplified as

$$\frac{d\vec{m}}{dt} = \vec{\tau}_{field} + \vec{\tau}_{current} + \vec{\tau}_{therm} \quad (2.10)$$

where the $\vec{\tau}_{field}$, $\vec{\tau}_{current}$, and $\vec{\tau}_{therm}$ represent the exerted torques by the external magnetic field, the electrical current, and the thermal fluctuation, respectively.

2.3.1 Field-induced domain wall motion

When an external magnetic field \vec{H}_{ext} is applied to the magnetic moment \vec{M} with a finite angle, the precession of \vec{M} occurs around the field. In principle, the \vec{H}_{ext} induces the additional energy into the steady state, so called Zeeman energy E_{zeeman} and it can be described by [57]

$$E_{zeeman} = -\mu_0 \int \vec{M} \cdot \vec{H}_{ext} dV = -\mu_0 \vec{m} \cdot \vec{H}_{ext} \quad (2.11)$$

where the μ_0 is a permeability, and V is the total volume of magnet. Hence, the \vec{m} favors to minimize the total energy by aligning parallel to the field direction.

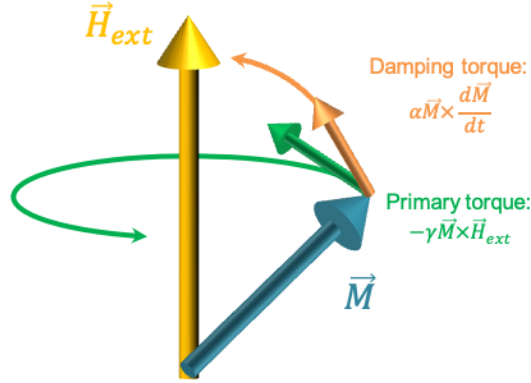


Figure 2.9. Field-induced torques on magnetization. Primary and damping torques applied on the magnetization \vec{M} in a response to an external magnetic field \vec{H}_{ext} . \vec{M} is consequently aligned along the direction of \vec{H}_{ext} .

As can be seen in Fig. 2.9, the \vec{H}_{ext} exerts a primary torque $-\gamma \vec{m} \times \vec{H}_{ext}$ that gives rise to the precession motion of \vec{m} . In addition to the precession, a primary torque induces a damping torque $\alpha \vec{m} \times \frac{d\vec{m}}{dt}$ which eventually rotates \vec{m} towards \vec{H}_{ext} . As a consequence, the field-induced torque τ_{field} is given by

$$\tau_{field} = -\gamma \vec{m} \times \vec{H}_{ext} + \alpha \vec{m} \times \frac{d\vec{m}}{dt} \quad (2.12)$$

where α is a gilbert damping constant which indicates the strength of dissipative effect. Hence, the LLG equation induced by the external field can be written as

$$\frac{d\vec{m}}{dt} = -\gamma\vec{m} \times \vec{H}_{ext} + \alpha\vec{m} \times \frac{d\vec{m}}{dt}. \quad (2.13)$$

Now let us consider the DW motion in the presence of external magnetic field (Fig. 2.10). We assume that the DW is formed in between $\downarrow\uparrow$ ($\otimes|\odot$) domain configuration. The external field \vec{H}_{ext} can be composed of three components H_x, H_y , and H_z . Thus,

$$\vec{H}_{ext} = H_x \cos \phi \sin \theta + H_y \sin \phi \cos \theta + H_z \cos \theta. \quad (2.14)$$

When the field is applied to the x -direction ($H_x \neq 0$, and $H_y, H_z = 0$), which is antiparallel or parallel to the magnetization of DW, and perpendicular to the orientation of two domains, the DW does not move due to $\vec{\tau}_{field} = 0$. Despite $\vec{\tau}_{field} \neq 0$, in case of $H_y \neq 0$, ($H_x, H_z = 0$), the DW only transforms to the Bloch wall without any changes in its initial position. Both cases, the field is applied to hard-axis of magnet, thus the E_{zeeman} is nearly zero since the volume of DW is negligible compared to two domains. As a result, \vec{H}_{ext} does not influence the entire potential energy landscape.

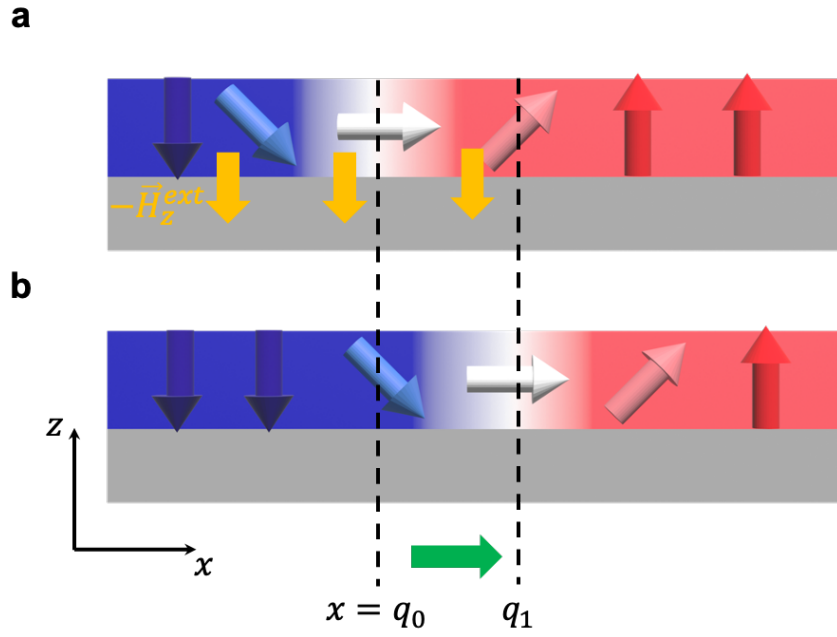


Figure 2.10. Field-induced domain wall motion. Illustration of field-induced domain wall motion in perpendicularly magnetized ferromagnet nanowire. Néel wall is formed between $\downarrow\uparrow$ ($\otimes|\ominus$) domain configuration. An external field along $-z$ direction ($-\vec{H}_z^{ext}$) exerts torques on domain wall magnetization **(a)**, thereby inducing motion ($q_0 \rightarrow q_1$) **(b)**.

In contrast, the field-induced DW motion (FIDWM) occurs in the presence of the field along z -direction (easy-axis; $H_z \neq 0$). Because the E_{zeeman} induces the tilting of the energy landscape with respect to the DW position $x = q$, thereby driving DW towards the total energy minima [77]–[79]. Depending upon the orientation, hence, either $+z$, or $-z$, the DW can move towards right or left-hand side from initial position q_0 , respectively (Fig. 2.10). According to Eq. (2.11), the degree of tilting of landscape is proportional to the magnitude of easy-axis components of field.

2.3.2 Current-induced domain wall motion

2.3.2.1 Spin-transfer torque

When the electron travels into the conventional non-magnetic materials, the spins of electron are randomly oriented therefore the net spin polarization is zero. On the other hand, when the electrons are travelling into the FM, which is magnetized along a specific orientation, they are scattered by the magnet moments through the s - d (transition metals) [80] or s - f (rare earth metals) [81] exchange interaction, thereby resulting a spin-polarization of electrons. Here, the spins that are parallel to the magnetic moment are less scattered while the others are more scattered. As a result, the spin-dependent scattering gives rise to the spin-polarized current in the FM. The degree of spin-polarization P in the FM can be identified as

$$P = \frac{\sigma_{\uparrow} - \sigma_{\downarrow}}{\sigma_{\uparrow} + \sigma_{\downarrow}} \quad (2.15)$$

where the σ_i ($i = \uparrow$ or \downarrow) is the conductivity of electrons depending upon the parallel or antiparallel with respect to the magnetization of the material. In general, the $3d$ transition metal based FMs (Co, Ni, and Fe) exhibit positive polarization ($P > 0$).

Slonczewski [16], and Berger [17] found that, interestingly, the spin-polarization process not only occurred in one direction, but also accompanied with a reciprocal phenomenon. This means that magnetization can also be influenced by the injected spin current during the scattering. As the spin polarized electrons travel, the spins that are not collinear with magnetic moment orientation exchange their spin and magnetic angular momentum. These angular momenta exchange results to the parallel alignment of spins of electrons and the magnetic moments. As a consequence, the magnetic moments are rotated toward the orientation of polarized spins of electrons by the torque that is called the spin-transfer torque (STT). Here the governing rule is the total angular momentum conservation, thus it is also known as an adiabatic STT and the corresponding torque is given by

$$\tau_{aSTT} = -b_j \vec{m} \times \vec{m} \times (\hat{j} \cdot \nabla) \vec{m} \quad (2.16)$$

where b_j is the adiabatic STT coefficient, \hat{j} is the unit vector of electrical current density flowing along the magnetic layer, respectively. The adiabatic STT coefficient b_j is proportional to the degree of spin polarization P [82].

On the other hand, there are some cases of STT which do not agree with the angular momentum conservation rule [83], that is possibly due to the mistracking between spins and local moments. The STT resulting from corresponding mechanism is called a non-adiabatic STT and can be written as [84]

$$\tau_{naSTT} = -\beta b_j \vec{m} \times (\hat{j} \cdot \nabla) \vec{m} \quad (2.17)$$

where β is the non-adiabatic STT coefficient that indicates the ratio to the non-adiabatic STT to the adiabatic STT. Note here that the direction of adiabatic STT is an analogy to the damping torque in which the local moment rotates toward spins, therefore it is also called a damping-like torque. The non-adiabatic STT, however, generates the precession of moments around spins that is similar to the primary field torque discussed in previous section 2.1.4.1. Hence, it is also named as field-like torque.

As a result, the LLG equation can be extended by including a both STT terms ($\tau_{aSTT} + \tau_{naSTT}$) in addition to Eq. (2.13)

$$\frac{d\vec{m}}{dt} = -\gamma \vec{m} \times \vec{H}_{ext} + \alpha \vec{m} \times \frac{d\vec{m}}{dt} - b_j \vec{m} \times \vec{m} \times (\hat{j} \cdot \nabla) \vec{m} - \beta b_j \vec{m} \times (\hat{j} \cdot \nabla) \vec{m}. \quad (2.18)$$

For the STT-driven DW motion, as can be seen in Fig. 2.11, the spin of injected electron into the nanowire is initially polarized along +z direction and passes through the DW by tracking the rotation of magnetization along the DW. During this process, the exchange of angular momentum between spins and moments exerts the STT, thereby moving the DW in the electron flow direction. Note here that the direction of CIDWM in STT is opposite to the current flow direction [15], [18].

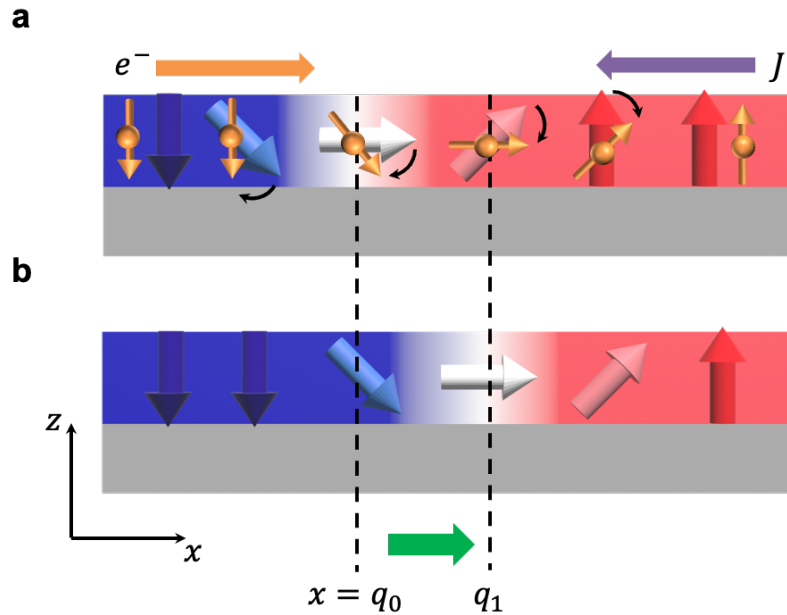


Figure 2.11. Spin-transfer torque induced domain wall motion. (a) As the electrical current flows in $-x$ direction, the injected spin polarized electrons into the domain wall give rise to the spin-transfer torque, thereby resulting a domain wall motion ($q_0 \rightarrow q_1$) (b). The direction of domain wall motion is opposite to current flow direction.

2.3.2.2 Spin-orbit torque

The main driving force to manipulate the DW is the STT arising from the spin polarized current. So far, we introduced that the origin of STT is mainly due to the angular momentum exchange of electrons flowing into the FM. However, there is another way of transferring angular momentum originating from the spin-orbit interaction phenomenon, so called a spin-orbit torque (SOT) [6], [7], [25], [29], [30], [48]. Depending upon the underlying mechanism, the SOT can also be classified as arising from either the spin Hall effect (SHE) [31] or the Rashba-Edelstein effect [85], [86]. In contrast to conventional STT, both are observed in the bilayer system of a non-magnetic heavy metal layer/ferromagnet in the presence of strong spin-orbit coupling. The major difference between the two is that the SHE is mainly governed by a bulk effect whereas the Rashba-Edelstein effect is an interfacial effect originating from the broken inversion symmetry [87]. Of course, it is possible that both can simultaneously generate

SOT in certain systems. From now on, however, we only consider the SHE as a main source of SOT in our discussion since the Rashba-Edelstein effect is negligible in our experiments [7].

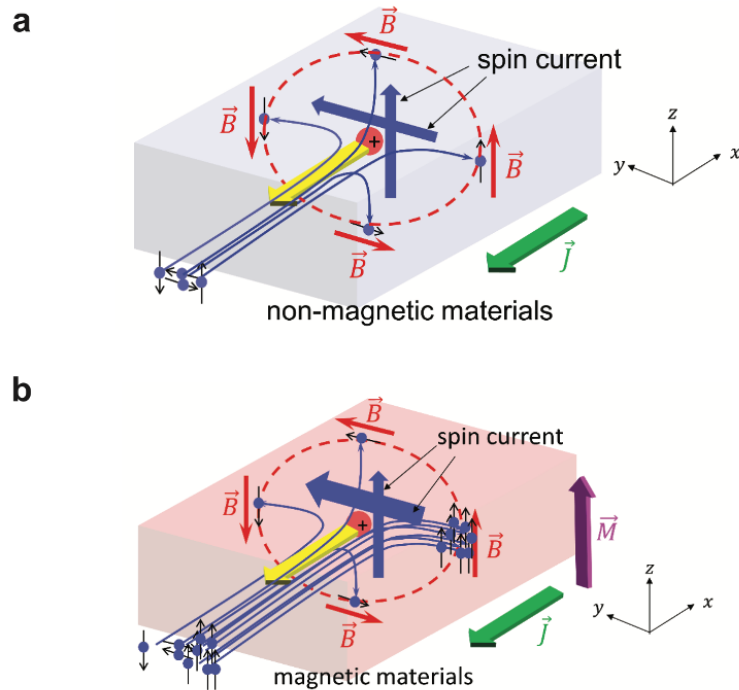


Figure 2.12. Illustration of spin Hall effect and anomalous Hall effect. Spin current generated by (a) spin Hall effect in non-magnetic materials and (b) anomalous Hall effect in magnetic materials. Note that there is no charge current accumulation induced in spin Hall effect contrary to anomalous Hall effect. Figure is adopted from [59] with permission from IOP publishing.

The SHE is a transport phenomenon that gives rise to the charge to spin conversion thereby leading to a spin accumulation perpendicular to the current flow direction (Fig. 2.12a). In general, this can be distinguished between an intrinsic or extrinsic SHE but both requires a large SOC in host material. The intrinsic SHE arises from a band splitting due to the SOC and an effective magnetic field caused by Berry phase [88], whereas the extrinsic SHE is based on the scattering of conduction electrons at impurities or defects in a real space [89], [90]. This is a relativistic effect between electrons and positive ions similar to the anomalous Hall effect (AHE) in FM (Fig. 2.12b) [91], but is observed in non-magnetic (NM) materials. In this thesis, we only focus on the extrinsic SHE that is more relevant for our experimental works. In

principle, the SHE leads to a deflection of charge carriers depending upon the spin orientation. The main difference between the SHE and AHE is that the SHE only accumulates the spin current, no charge current, therefore there is no transverse voltage (see Fig. 2.12). As a result, the direction of current ($\pm x$ -direction), spin current ($\pm y$ and z -direction), and spin orientation ($\pm z$ and y -direction) are all perpendicular to each other.

The SHE efficiency can be evaluated by quantifying the charge to spin conversion efficiency that is defined by

$$\theta_{SHE} = \frac{J_s}{J_c} \quad (2.19)$$

where the J_s is the spin current density and the J_c is the charge current density, respectively. Here the θ_{SHE} is also known as the spin-Hall angle [92]. Note that the θ_{SHE} can have either positive or negative sign depending upon the materials, since the orientation of J_s can be opposite to one another. For instance, the Pt [6], [25] shows a positive θ_{SHE} , whereas Ta [48], and W [48], [67] show negative values. As a result, the spin current that flows to $+z$ direction can be given by

$$\vec{S} = \frac{\hbar\theta_{SHE}}{2e} (\hat{J}_c \times \hat{z}) \quad (2.20)$$

where the \hbar is the Planck constant, and the e is the elementary charge, respectively. For the Pt, the spin current along $+z$ direction is polarized in $-y$ direction when J_c flows $+x$ direction.

In the NM/FM bilayer system, when the majority current flows into the NM layer instead of FM (J_{NM}/J_{FM}), the conventional STT is negligible, but the SHE is prominent source for generating spin current in the system. Since the SHE results in the spin polarization along $-y$ direction in this case, the torque arising from SHE towards adjacent upper FM layer can be written as

$$\vec{\tau}_{SHE} = \vec{m} \times (\vec{m} \times \vec{H}_{SHE}) = \vec{m} \times (\vec{m} \times \frac{\hbar\theta_{SHE}}{2eM_s t} (\hat{J}_c \times \hat{z})) = \theta_{SHE} b_J \vec{m} \times \vec{m} \times \hat{y} \quad (2.21)$$

where \vec{H}_{SHE} is the effective field generated from SHE that can be parameterized by $H_{SHE} = \frac{\hbar\theta_{SHE}J}{2eM_s t}$. Here the t denotes the thickness of adjacent FM layer. As a consequence, the LLG equation including the SOT driven by SHE is given by

$$\begin{aligned} \frac{d\vec{m}}{dt} = & -\gamma\vec{m} \times \vec{H}_{ext} + \alpha\vec{m} \times \frac{d\vec{m}}{dt} - b_j \vec{m} \times \vec{m} \times (\hat{j} \cdot \nabla)\vec{m} - \beta b_j \vec{m} \times (\hat{j} \cdot \nabla)\vec{m} \\ & + \theta_{SHE} b_j \vec{m} \times \vec{m} \times \hat{y}. \end{aligned} \quad (2.22)$$

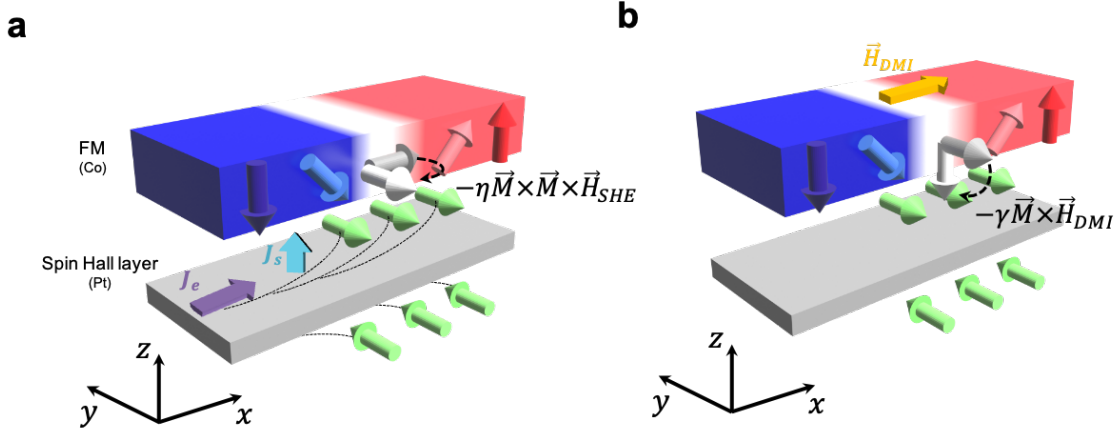


Figure 2.13. Spin-orbit torque driven by spin Hall effect. (a) Spin polarized currents (J_s arrows) arises from the charge current flow (J_e) in adjacent non-magnetic spin Hall layer (e.g., Pt) that give rise to the rotation of domain wall magnetization towards y -direction. (b) \vec{H}_{DMI} coherently exerts torque on the rotated wall towards out-of-plane direction, thereby moving the domain wall along the current flow direction.

Now let us consider the DW motion driven by SHE. In the present thesis, we employed the Pt/Co bilayer as a primary source of the SOT, thus the SHE is generated by Pt layer and influences to the DW in Co layer. As discussed in section 2.1.3.1., the \vec{H}_{DMI} stabilizes the Néel wall, therefore the \vec{H}_{SHE} exerts the torque to $\vec{m}_{Néel}$ ($\vec{H}_{SHE} \perp \vec{m}_{Néel}$) (Fig.2.13a). Simultaneously, the \vec{H}_{DMI} applies a restoring torque on the $\vec{m}_{Néel}$ thereby leading an out-of-plane rotational torque (Fig.2.13b). This is called chiral spin torque. As a consequence, the DW can move along the same direction of current flow, that is opposite to the STT-driven case (DWs move along the electron flow direction). Although the SOT-driven DW motion requires

a source material (NM) in addition to FM, and is limited for the Néel DW ($\vec{H}_{SHE} \perp \vec{m}_{Néel}$), in comparison to STT, it exhibits a significant efficient DW motion by achieving high velocity with lower current density [6], [7].

2.3.2.3 Exchange coupling torque

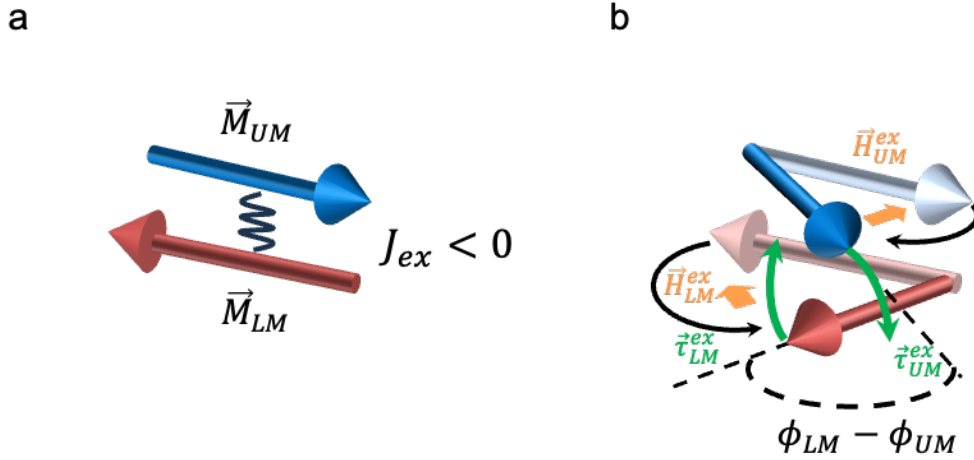


Figure 2.14. Illustration of exchange coupling torque in anti-parallel coupled moments.

(a) Antiferromagnetically coupled domain walls in lower (LM) and upper magnetic layer (UM) in equilibrium state (no external stimuli). (b) Exchange coupling fields \vec{H}_{ex}^i ($i = LM$ or UM) generate the exchange coupling torques $\vec{\tau}_{ex}^i$ on canted moments towards out-of-plane direction.

Due to the high current efficiency, the SOT has become a mainstream for the chiral DW motion. Recently, however, the more efficient CIDWM has been reported in SAF, in which the maximum velocity can reach up to ~ 1000 m/s, due to the additional contribution of new types of torque, namely the exchange coupling torque (ECT) [8], [93]. The ECT originates from the effective interlayer exchange field \vec{H}_{ex}^i between two sub-FM layers, LM and UM, that can be derived from the $\vec{H}_{ex}^i = -\frac{\partial E_J^i}{\partial \vec{m}_i}$, where E_J^i is the inter-layer exchange energy in LM or UM layer ($i = LM$ or UM). Thus, the exchange field in LM and UM can be described by

$$\vec{H}_J^{LM} = -2 \frac{J_{ex}}{m_{LM}} \sin(\phi_{LM} - \phi_{UM}) \hat{\phi}, \quad (2.23)$$

$$\vec{H}_J^{UM} = -2 \frac{J_{ex}}{m_{UM}} \sin(\phi_{UM} - \phi_{LM}) \hat{\phi}, \quad (2.24)$$

respectively, where the $\hat{\phi} = -\sin \phi \hat{x} + \cos \phi \hat{y}$. As a consequence, the ECT is then given by

$$\vec{\tau}_{ECT}^i = -\gamma \vec{m}_i \times \vec{H}_j^i. \quad (2.25)$$

As can be seen in Fig. 2.14, when two DWs are collinear (anti-parallel for SAF) in stationary state, \vec{H}_j^i becomes zero, thus there is no exchange torque. However, as soon as the spin canting occurs in one of DWs, the \vec{H}_j^i generates $\vec{\tau}_{ECT}^i$ thereby leading a DW motion. Note that the DW in the LM layer \vec{m}_{DW}^{LM} is directly governed by the $\vec{\tau}_{SHE}$ generated from Pt underlayer (see Fig. 2.13), thus the DW in the UM layer \vec{m}_{DW}^{UM} moves toward the current flow direction together as well. The direction of $\vec{\tau}_{ECT}^i$ is always along the z -direction but the sign is opposite in LM and UM depending upon the configuration.

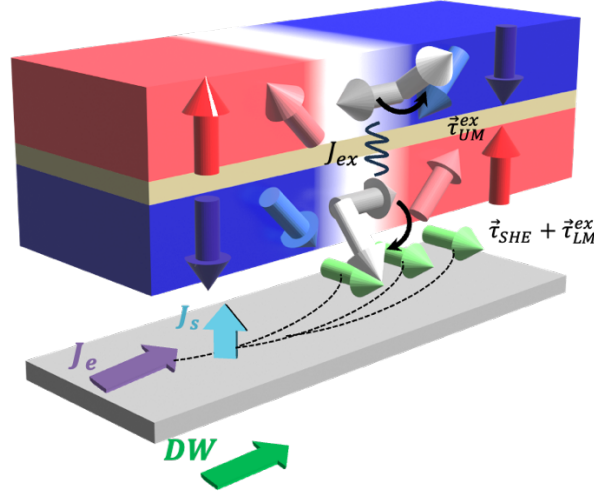


Figure 2.15. Exchange coupling torque induced domain wall motion in synthetic antiferromagnet. The domain wall motion in lower magnetic layer (LM) is governed by primary spin orbit torque ($\vec{\tau}_{SHE}$), thus moving in a same direction to charge current flow J_e . Antiferromagnetic interlayer exchange coupling ($J_{ex} < 0$) gives rise to an exchange field that exerts the exchange coupling torque $\vec{\tau}_i^{ex}$ ($i = LM$ or UM) along out-of-plane direction, thereby moving together with a domain wall in upper magnetic (UM) in a same direction.

In this regard, the underlying mechanism of CIDWM in SAF is still similar to the FM, so that the SOT is main source for delivering the spin torque to initiate the DW motion (Fig. 2.15). Moreover, of course, there is a contribution of \vec{v}_{SHE} generated from the spacer layer. However, the corresponding SOT efficiency is considerably less compared to the ECT. Hence, the highly efficient CIDWM in SAF is mainly induced by the SOT arising from LM and the ECT. Consequently, the LLG equation for the DW motion in SAF is redefined by [59]

$$\begin{aligned} \frac{d\vec{m}_i}{dt} = & -\gamma\vec{m}_i \times \vec{H}_{ext} + \alpha\vec{m}_i \times \frac{d\vec{m}_i}{dt} - b_j \vec{m}_i \times \vec{m}_i \times (\hat{j} \cdot \nabla)\vec{m}_i \\ & - \beta b_j \vec{m}_i \times (\hat{j} \cdot \nabla)\vec{m}_i + \theta_{SHE} b_j \vec{m}_i \times \vec{m}_i \times \hat{y} \\ & - \gamma\vec{m}_i \times \vec{H}_j^i \quad (i = LM \text{ or } UM). \end{aligned} \quad (2.26)$$

Interestingly, the strength of the ECT can be further enhanced by increasing the AF coupling strength J_{ex} , which is determined by the spacer layer, and as well as achieving $m_{LM} = m_{UM}$ [8], [36], [61]. As shown in Fig. 2.16, the DW velocity is maximized when $m_{LM} = m_{UM}$, where they are fully compensated to each other ($m_R = 0$).

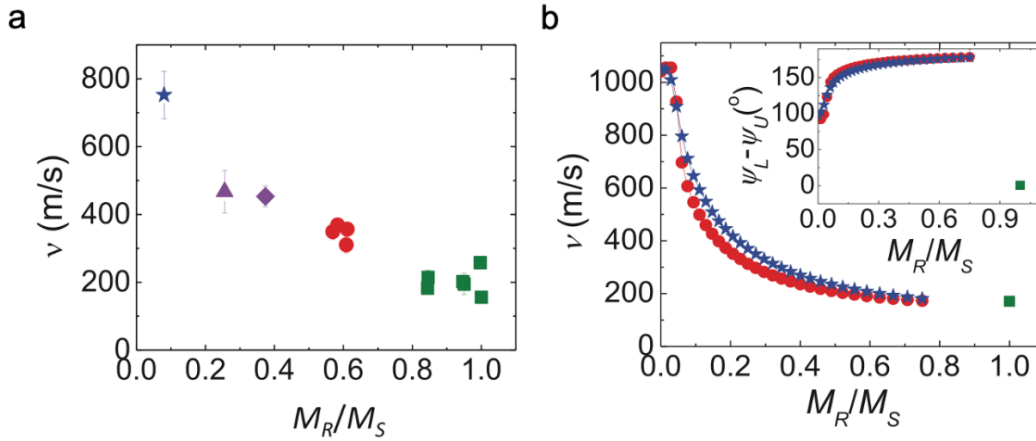


Figure 2.16. Moment compensation dependent domain wall velocity in synthetic antiferromagnet. Maximum domain wall velocity as a function of moment compensation degree $\frac{M_R}{M_S}$, obtained by (a) experiments, and (b) calculation. $\phi_{LM} - \phi_{UM}$ dependency on $\frac{M_R}{M_S}$ within the analytical model is shown in inset as well. Figures are adopted from [59] with permission from IOP publishing.

2.3.3 Thermally-induced domain wall motion

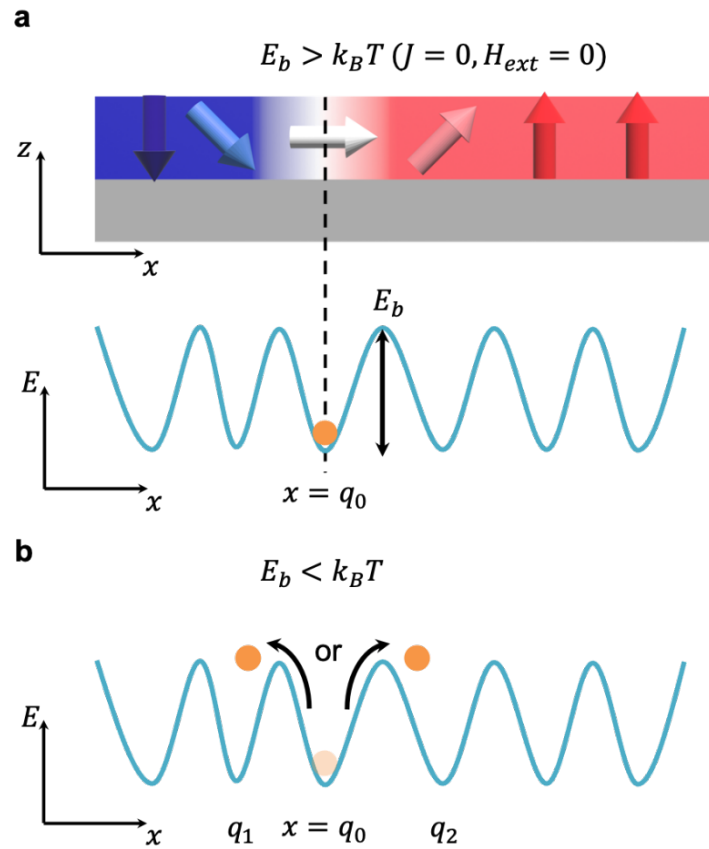


Figure 2.17. Illustration of thermally-induced domain wall motion. At finite temperature T , domain wall stays at initial position ($x = q_0$) when the local potential barrier height is larger than thermal energy ($E_b > k_B T$) (a). Thermally activated domain wall motion arises when $E_b < k_B T$ (b). Note that the direction of thermally-induced domain wall motion is arbitrary, thus domain wall moves to either $x = q_1$ or q_2 .

In previous sections, we discussed the DW motion induced by the effective fields, that can be generated from either an external field, or electrical current. This also implies that any kind of external stimuli that potentially produce the effective fields can result to the DW motion. In some cases, for example, the spontaneous DW motion can occur even in the absence of either an external magnetic field, or an electrical current source [94]–[96]. That is due to the effective fields induced by the thermal activation energy, $k_B T$, where k_B is the Boltzmann

constant, and T is the temperature, respectively. At a finite temperature, the thermal agitation gives rise to a fluctuation of both conduction electrons and magnetic moments, thereby generating the current and field fluctuations [97]–[104]. Now let us discuss how this influences the DW. As shown in Fig. 2.17, the steady state of DW is initially positioned at q_0 , which is the energy minima of potential energy landscape. Once the thermal energy is large enough to overcome corresponding potential energy barrier E_b , the DW can move to the neighboring potential energy minima (q_1 or q_2). This is called thermally-induced DW motion. Note that the direction of thermally-induced DW motion is arbitrary.

2.3.3.1 Energy barrier of domain wall motion

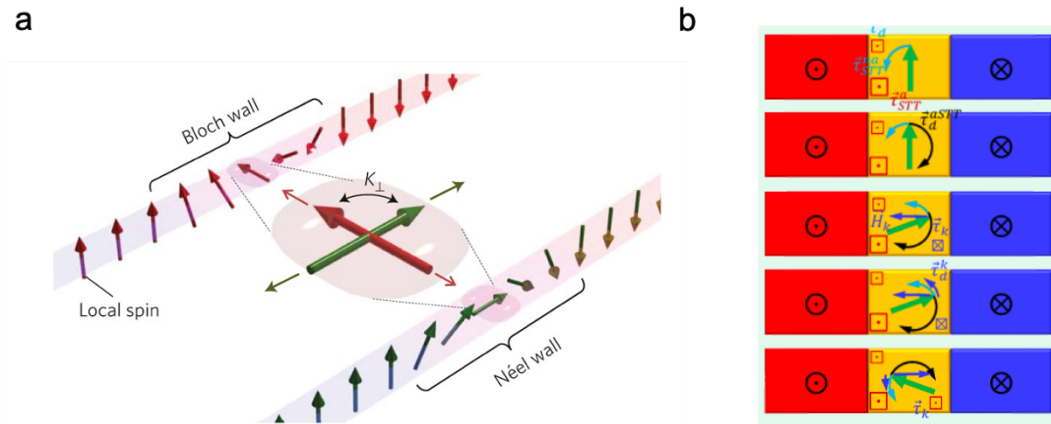


Figure 2.18. Intrinsic energy barrier of STT-driven domain wall motion. (a) Deviation of Bloch wall moment induced by STT. **(b)** Due to the deviation, a shape anisotropy field \vec{H}_k becomes non-zero, thus generating a torque $\vec{\tau}_k$ in opposite direction to STT $\vec{\tau}_{STT}$. As a consequence, the domain wall stays at initial position. Figures are adopted from [49] and [59] with permission from Springer Nature and IOP publishing, respectively.

The origin of E_b for DW is still not yet clearly understood, but there are several parameters, such as the volume, and the anisotropy of DW that certainly contribute to determine the barrier height likewise conventional MTJs. It also depends on the type of DW either Bloch or Néel wall, where the underlying mechanism of DW motion is distinct. In case of Bloch wall, the DW motion can be generated by the STT, whereas the SOT drives the DW

motion in the Néel wall. In STT-driven motion, there is an intrinsic energy barrier that originates from the competition between shape anisotropy and the degree of tilting of DW [39], [59]. As shown in Fig. 2.18, the under the threshold current, the precession of DW only occurs without complete rotation, thus the DW is pinned and its position does not change. On the other hand, the SOT-driven motion does not have an intrinsic energy barrier since the DMI strongly stabilizes the DW [32], [58]. There is only extrinsic energy barrier that is induced by localized non-uniform anisotropy, the grain boundaries, the edge roughness of structures, and so on. Therefore, the extrinsic barrier is common for the DW motion in reality regardless of mechanism, and this is verified by number of experiments [37]–[40].

Ideally, the corresponding barrier height E_b can be evaluated by measuring an activation energy of thermally-induced DW depinning based on Arrhenius law [39], [47], [105]. However, such thermal effects on the DW at a steady state have not been simply taken into account so far due to the experimental difficulties. One of the main challenges is that the detection of DW motion is limited since the thermal effective fields is applied in an arbitrary orientation. Furthermore, the time-scale for occurring a thermal activation process is indefinite, thus it is not straightforward. Instead, the DW depinning threshold current or field in thermally assisted regime, where the excitation time-scale is much longer than intrinsic angular momentum transfer process [106], [107]. Despite such difficulties, it is important to identify how the thermal effects on the DW are accounted for the DW dynamics.

2.3.3.2 Electrical current fluctuations

Let us first consider the influence of thermal fluctuations of electrons in the presence of DW. In metallic system, the fluctuating electrons lead to the current fluctuations that exhibit a typical decaying time scale of $\tau \sim 10^{-15} \sim 10^{-13}$ sec based on Drude model. In this regard, from the fluctuation-dissipation theorem [108], the spectral density of current fluctuations can be obtained by

$$S_J(\omega) = \frac{4k_B T}{V} \cdot \text{Re}\sigma(\omega) \quad (\omega > 0) \quad (2.27)$$

where $\sigma(\omega)$ is the electrical conductivity of the sample which is governed by Drude theory at frequency ω , and V is the volume of sample, respectively. Note here that we assume the profile of J obeys Gaussian distribution. By integrating Eq. 2.23 with respect to ω , and taking root mean square, we obtain the average magnitude of current density fluctuations in given system,

$$\delta J = \sqrt{\frac{k_B T}{V} \cdot \frac{\sigma}{\tau}} \quad (\omega = 0) \quad (2.28)$$

where $\sigma = \sigma(0)$ is the d.c. conductivity. Note that Eq. 2.24 concerns a current density fluctuation within a time scale of τ . As a consequence, the resulting STT and SOT induced by δJ can be given by

$$\vec{\tau}_{STT}^{therm} = -b_j \vec{m} \times \vec{m} \times (\vec{\delta J}_{FM} \cdot \nabla) \vec{m} - \beta b_j \vec{m} \times (\vec{\delta J}_{FM} \cdot \nabla) \vec{m}, \quad (2.29)$$

$$\vec{\tau}_{SHE}^{therm} = \vec{m} \times (\vec{m} \times \frac{\hbar \theta_{SHE}}{2eM_s t} (\vec{\delta J}_{NM} \times \hat{z})), \quad (2.30)$$

respectively. Note that since $\vec{\delta j}$ is randomly generated in both NM and FM layers, only x-component of $\vec{\delta j}$ contribute the DW motion via both STT and SOT. Thus, it is impossible to determine the direction of DW motion induced by current fluctuation.

2.3.3.3 Magnetic field fluctuations

In addition to the electron fluctuation, the thermal fluctuation of magnetization generates the effective field and that can be described by the stochastic LLG equation, also known for the Langevin equation [98], [100], [102],

$$\frac{d\vec{M}}{dt} = -\gamma\vec{M} \times (\vec{H}_{eff} + \vec{H}_{fl}) + \alpha\vec{M} \times \frac{d\vec{M}}{dt} \quad (2.31)$$

where, \vec{H}_{eff} , and $\vec{H}_{fl}(\vec{r}, t)$ are the effective magnetic field, and the random thermal fluctuating magnetic field, respectively. Here \vec{H}_{eff} includes the external field, the intra-layer exchange field, the dipolar field, the DMI field, and the anisotropy field. $\vec{H}_{fl}(\vec{r}, t)$ is typically assumed to be a Gaussian random process satisfying $\langle H_{fl}^i(\vec{r}, t) \rangle = 0$ and $\langle H_{fl}^i(\vec{r}, t) H_{fl}^j(\vec{r}', t') \rangle = \frac{2\alpha k_B T}{\gamma \mu_0 M} \delta_{ij} \delta(\vec{r} - \vec{r}') \delta(t - t')$ ($i, j = x, y, z$) such that

$$\vec{H}_{fl}(\vec{r}, t) = \vec{\zeta}(\vec{r}, t) \sqrt{\frac{2\alpha k_B T}{\gamma \mu_0 M dV dt}} \quad (2.32)$$

where, dV , dt , and $\vec{\zeta}(\vec{r}, t)$ are the fluctuating element volume, fluctuating time interval, and stochastic random unit vector, respectively. δ_{ij} is the Kronecker delta. $\delta(\vec{r} - \vec{r}')$ and $\delta(t - t')$ are Dirac delta functions. dV can be approximated to be the DW volume in a given geometry, $w t_{FM} \pi \Delta$ (width of wire : w , thickness of FM: t_{FM} , DW width parameter: Δ). Here note that only the easy-axis component of \vec{H}_{fl} has been considered since the other components (hard-axis) cannot move the DWs (see section 2.1.4.1).

Chapter 3 Experimental methods

In this chapter, we will introduce the experimental methods conducted in this study. The device fabrication process, especially, based on the magnetron sputtering thin film deposition, and nanofabrication techniques will be discussed. Furthermore, we present the measurement technique being used for the detection of domain wall motion by magneto-optic Kerr effect as well.

3.1 Film deposition and characterization

3.1.1 Magnetron sputtering

The magnetic thin films employed in this study were grown by the standard magnetron sputtering method. Magnetron sputtering is one of the physical vapor depositions (PVDs) method which is widely applied for thin film deposition not only in the research but also in the industry due to its high efficiency and uniformity for large scale production [109]. We prepared magnetic thin multilayers on Si (100) wafer covered with 250 Å thick thermally oxidized amorphous SiO₂ layer. This SiO₂ layer introduces very smooth surface roughness of ~1 Å and electrically insulating. We used our homemade sputtering system called as multi-source, atomically engineered, next generation, alloys and compounds (MANGO), which consists of main chamber with a base pressure of 10^{-9} torr, one turret-type magnetron sputtering chamber including twelve targets, and four sub-chambers each having three targets (see Figure 3.1b). The film structures employed in this study is consist of seed/capping layer, heavy metal (HM) layer, and FM multi layers. The perpendicularly magnetized single layer FM and SAF based racetrack structures are: 20 TaN / 30 Pt / 3 Co / 7 Ni / 1.5 Co / 30 TaN for single layer FM [6], and 20 TaN / 30 Pt / 3 Co / 7 Ni / 1.5 Co / 9.5 Ru / 3.5 Co / 7 Ni / 3 Co / 30 TaN for SAF [8] – units in Å. The seed and capping layer of TaN was deposited by reactive magnetron sputtering with an Ar/N₂ (85/15) gas mixture. The rest of metallic layer was deposited under 3 mTorr Ar pressure.

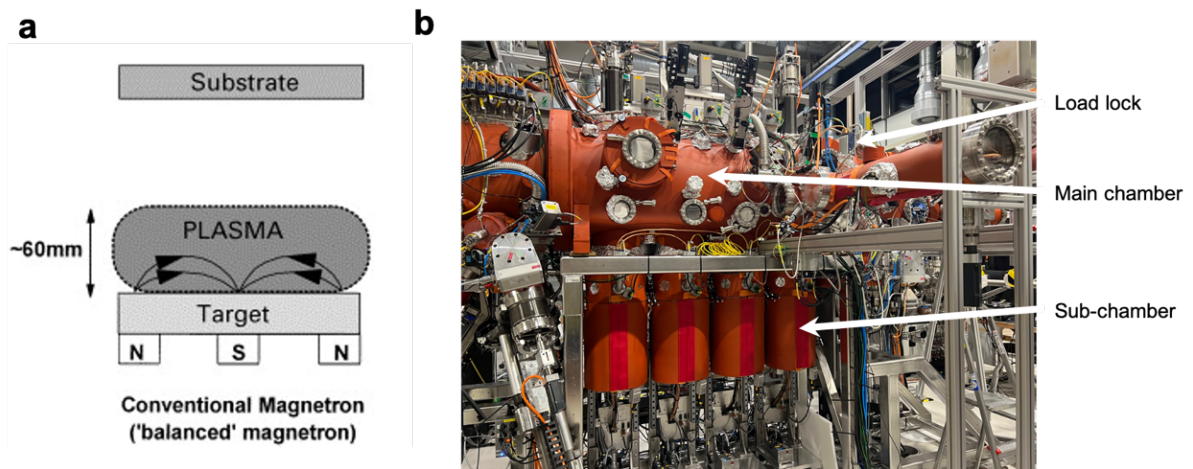


Figure 3.1. Magnetron sputtering deposition. (a) Schematic representation of conventional magnetron sputtering deposition. Target material is bombarded by energetic ions (e.g., Ar Plasma) and condense on the substrate as a thin film. **(b)** Image of Multi-source, atomically engineered, next generation, alloys and compounds (MANGO) deposition system. Figure is adapted from [109] with permission from Elsevier.

3.1.2 Vibrating sample magnetometry

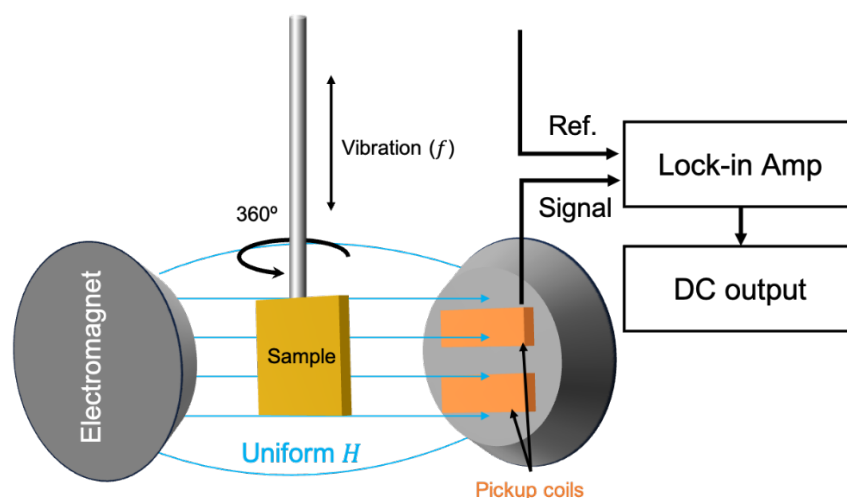


Figure 3.2. Schematic illustration of vibrating sample magnetometer. Magnetic sample is prepared by the size of 5×6 mm in order to position within the uniform field H generated from electromagnets. Sample is vibrated perpendicular to the field direction with a frequency of f (50~100 Hz). Lock-in amplifier collects the induced voltage from the pickup coils and convert to the DC output.

Magnetic properties of as-grown samples were characterized by vibrating sample magnetometer (VSM) at room temperature. VSM technique collects the induced electrical voltage from the change in the magnetic flux (Φ) based on Faraday's law of induction [110] (see figure 3.2). The sample vibrates continuously into and out of the pickup coils where the signal is collected with a frequency (f) in the presence of an external magnetic field. While the magnetic moments of sample align to the direction of field, the oscillation of voltage resulting from the change of Φ is collected and integrated by lock-in measurement. As a result, this electrical signal is proportional to the total magnetic moment of the sample. Based on the total magnetic moment and sample dimension, we can readily convert to the magnetization value. Determination of sample dimension, however, needs to be carefully considered with respect to the pickup coils area. Therefore, we prepared each sample with finite dimension of 5×6 mm which is sufficiently fit into pickup coils area for reliable measurement. In this study, we focused on the characterization of single layer FM and SAF films by measuring M-H hysteresis loops (see section 4.1).

3.2 Device fabrication

3.2.1 Lithography

For the first step of device fabrication, we patterned the device structures on the characterized film using a standard electron-beam (e-beam) and photolithography process. Prior to the patterning, the e-beam or photo resist was deposited by a spin coating process. Note that depending on post process, either deposition or etching, a positive or negative tone resist was employed, respectively (Table 3.1).

	Resist	Type	Thickness	Bake condition	Developer	Remover
E-beam	AR-P 6200.09	Positive	~ 200 nm	150 °C / 1 min	AR 600-546 (Amyl acetate)	AR 300-76
	AR-N 7520.18	Negative	~ 400 nm	85 °C / 1 min	AR 300-47 (TMAH)	AR 300-70
	AR 300-80N	Adhesion	~ 15 nm	65 °C / 2 min	-	Acetone
Photo	AR-P 3540 T	Positive	~ 1.4 μm	100 °C / 1 min	AR 300-44 (TMAH)	AR 300-76
	AR-N 4340	Negative	~ 1.4 μm	90 °C / 1 min	AR 300-475 (TMAH)	AR 300-76

Table 3.1. List of e-beam and photoresists and corresponding process conditions.

Most of main racetrack nanowire structures investigated in this thesis were prepared by an e-beam lithography (EBL), which is widely adapted to not only research but industry for reliable patterning of nm-scale high resolution structures [111]. The typical e-beam diameter is characterized to be in a range of few to hundreds of nanometers scale that can be modulated by varying an amplitude of beam probing current and corresponding aperture size of a condenser lens in electron-optical system. After beam calibration, the beam is directly exposed on the surface of the resist following the designed pattern structure which is designed by computer-aided design software. It is noteworthy that the resolution limit of our EBL system (JEOL JBX-8100FS) is guaranteed down to 8 nm line structure, thus it is able to achieve finest line edge roughness of straight nanowire (Fig 3.3b). In addition, EBL promises high precision of mask alignment overlay within ~20 nm accuracy. This is especially essential for our devices

due to the requirement of multiple exposure steps. After patterning of nanowires, we employed a photolithography process with positive tone resist for patterning of electrical contact pads which is typically larger than an area of $100 \times 100 \mu\text{m}^2$.

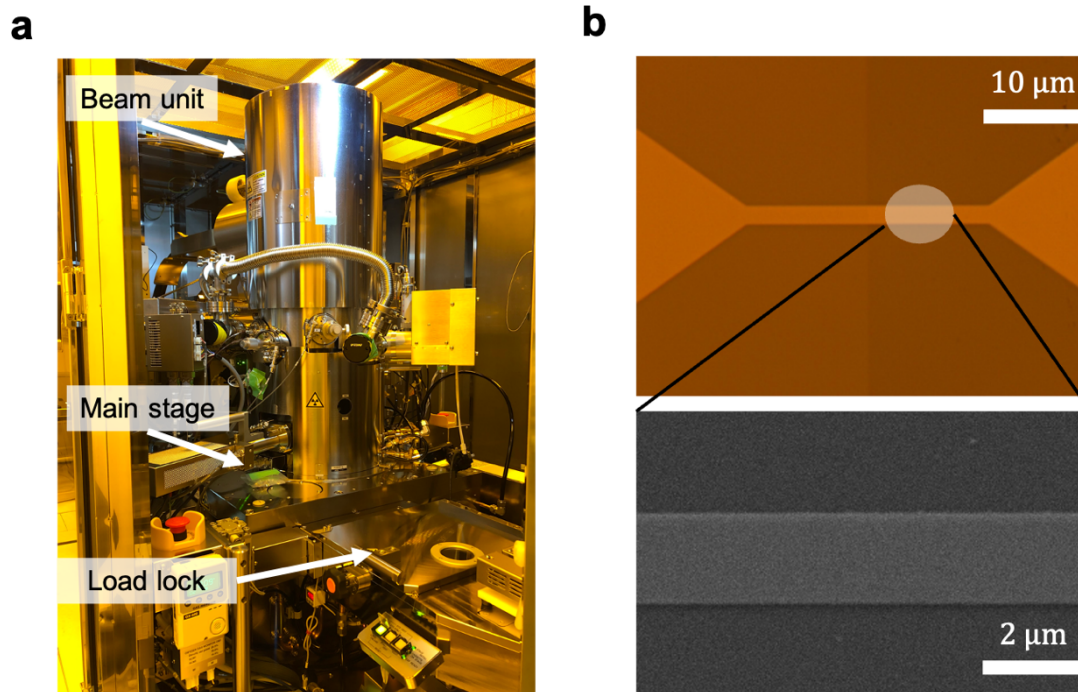


Figure 3.3. Electron beam lithography system and patterned racetrack nanowire. (a) JEOL JBX-8100 FS electron beam lithography system (100 kV beam acceleration voltage). Beam unit includes the emitter, apertures, and deflectors. **(b)** Representative racetrack nanowire structure with a wire width of $2 \mu\text{m}$. Both optical microscope (upper panel) and scanning electron microscope (SEM) images confirm sharp and smooth line edge roughness of wire.

3.2.2 Ion-beam etching/deposition

After the lithography steps, the racetrack nanowire structures are etched by Ar ion-beam etching (IBE) technique. Ion-beam etching (or milling) is a one of the most popular dry etching techniques in which energetic ions, typically Ar⁺ ions, are accelerated and physically bombarded towards the sample by the applied bias voltage so called an acceleration voltage in between sample stage and source [112]. As a result, materials from the sample are etched away by the accelerated Ar⁺ ions through the energy transfer between atoms. Therefore, compared to the chemical wet etching process, IBE is applicable to all substances. In addition, it also gives the degree of freedom in etching profile by varying an incident beam angle with respect to the sample. This is possible since the beam profile is highly anisotropic. Hence, it is suitable technique in many aspects for structuring of multilayers system likewise FM and SAF studied in this thesis.

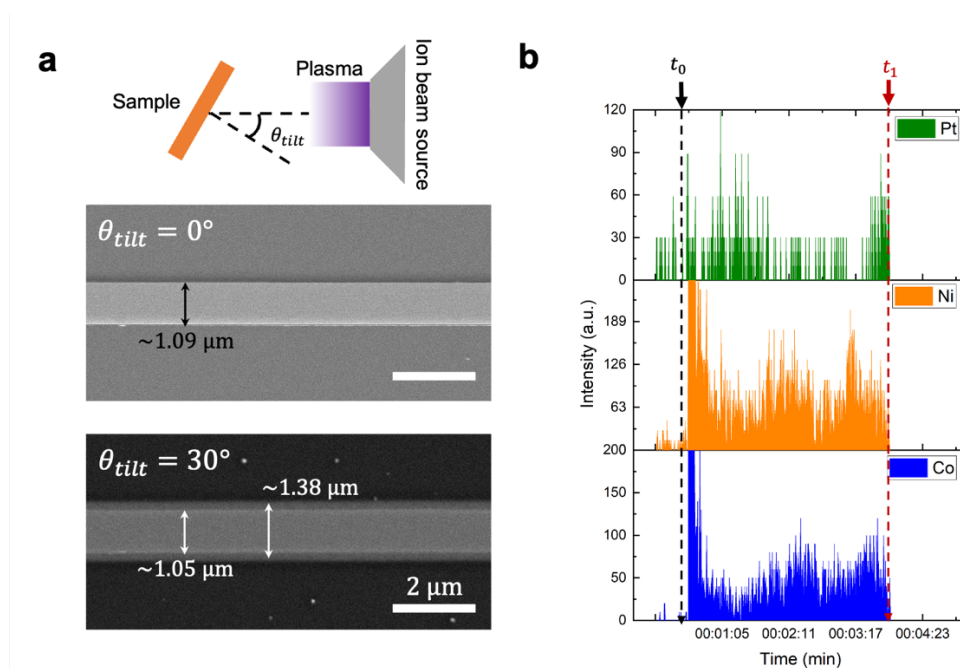


Figure 3.4. Incident angle dependent ion-beam etching profile and secondary-ion mass spectrometry. (a) Etching profile comparison between $\theta_{tilt} = 0^\circ$ and 30° on racetrack nanowire. Wide slope is observed at the edge of wire ($\theta_{tilt} = 30^\circ$). (b) Representative secondary-ion mass spectrometry profiles during multilayer racetrack etching process. Co, Ni, and Pt layers are clearly distinguished. t_0 and t_1 represents the etching start and end points, respectively.

To achieve the high-profile racetrack nanowire, we performed IBE with a zero-tilting angle ($\theta_{tilt} = 0^\circ$) in which the beam source faces the front of the sample as depicted in Fig. 3.4a. The etching is conducted in the presence of developed resist masks. Note that the typical etching rate of the resist is found to be much slower than the metallic thin films, thereby protecting the region underneath. During the IBE process, the secondary-ion mass spectrometry (SIMS) was utilized to monitor the etched secondary ions from the sample. This enables us to avoid an under or over etching of the sample. The representative SIMS profile during the etching process of SAF film is shown in Fig. 3.4b. After the etching process, the etched region is refilled with the aluminum oxide (AlO_x) layer for the passivation by *in-situ* ion-beam deposition (IBD).

Overview of entire device fabrication processes including lithography and etching is summarized in Fig. 3.5.

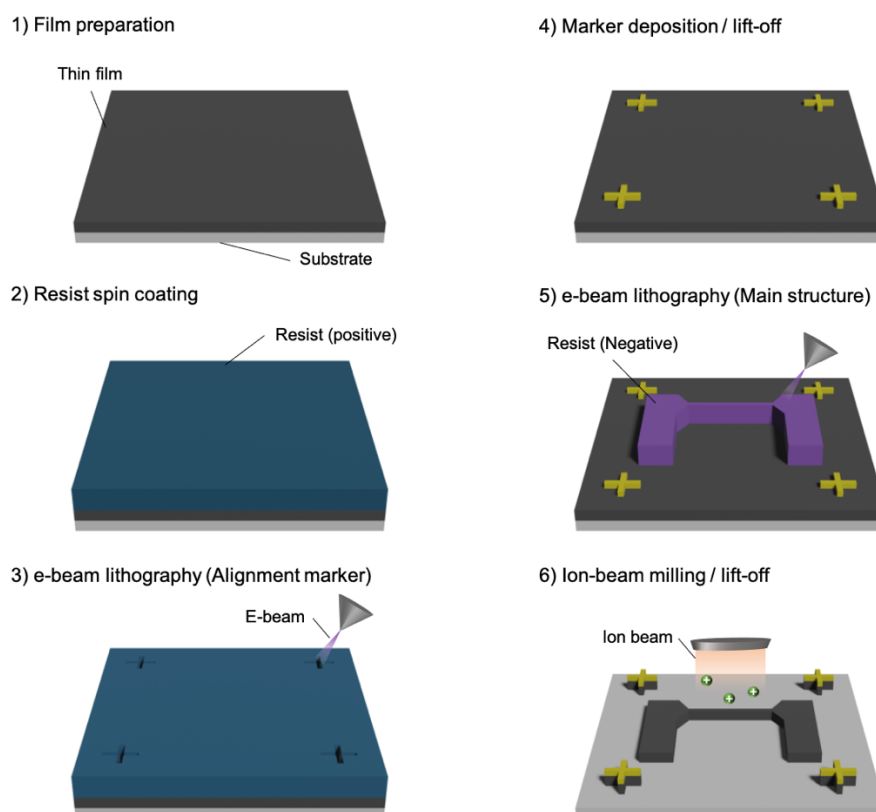


Figure 3.5. Schematic illustrations of racetrack device fabrication process flow. Overview of conventional racetrack nanowire device fabrication processes including two steps of lithography (alignment marker and main structure) and ion-beam etching.

3.3 Detection of magnetic domain wall motion

In order to study the magnetic DW motion in fabricated FM and SAF racetrack nanowire devices, we employed the optical method based on magneto-optical Kerr effect (MOKE). By utilizing the Kerr microscope in differential mode, the current- and field-driven DW motion were successfully captured in a range of spatial resolution down to sub- μm scale. In addition to that, a highly customized LabView software enables us to analyze the captured images and calculate the corresponding domain wall velocity as well.

3.3.1 Magneto-Optical Kerr Effect

Magneto-optical (MO) effect is the one of the prominent phenomena originated from the interaction between the light and quasistatic magnetic field. The fundamental origin of MO effects is based on the Zeeman exchange splitting together with spin-orbit interaction [113]. Once linearly polarized light which is superposition of left and right circular polarization propagates into the magnetic medium, the opposite sign of angular momentum from each circularly polarized light transfers to electrons thereby triggering an excitation between two different energy levels which arise from Zeeman exchange splitting [114]. This is projected as the deviation on complex Fresnel reflection coefficients of each circularization state with respect to the incident light, and results to a rotation of polarization plane and a change of ellipticity. Depending upon the analysis of either reflected or transmitted light from the sample, in general, MO effects can be classified into a Kerr effect or a Faraday effect, respectively [115]. Here, in this study, we rely on magneto-optical Kerr effect (MOKE) instead of Faraday effect, because our sample is grown on the standard silicon substrate, which can only yield the reflection of light. In particular, we adopted polar-MOKE (p-MOKE) configuration in which the orientation of magnetization is aligned parallel to the plane of incidence light in order to analyze perpendicularly magnetized FM and SAF structures.

The strength of MOKE signal is typically linearly proportional to the magnitude of magnetization and its orientation, but also strongly depends on the SOC as mentioned above [116]–[118]. In case of our FM and SAF, a strength of SOC is predominant at the Pt/Co interface due to the $3d$ - $5d$ orbital hybridization, which also contributes a substantial proximity induced magnetization [119]. As a consequence, this enables us to still detect the relevant MOKE signal from SAF structure although a remnant net magnetic moment is nearly zero.

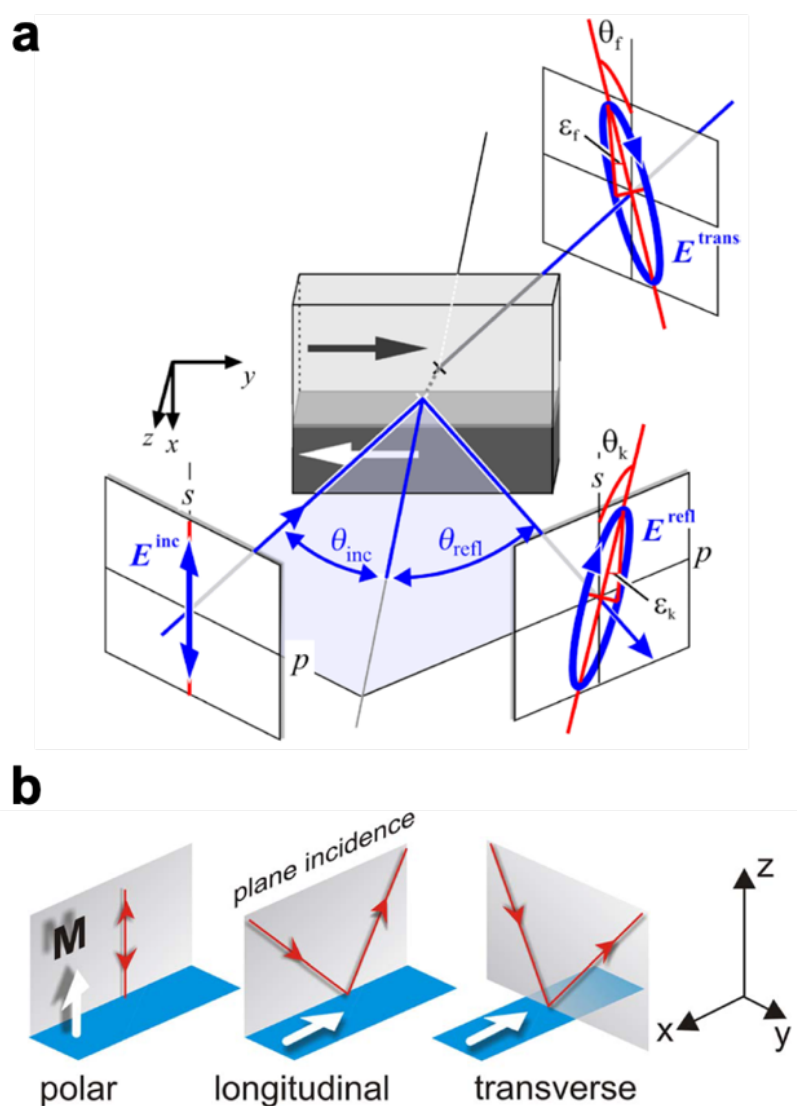


Figure 3.6. Magneto-Optical Kerr effect. (a) Illustrations of longitudinal Faraday (transmitted) and Kerr effect (reflected). Linearly polarized incident light is reflected from magnetic medium and transformed to an elliptically polarized light with Kerr rotation θ_k . (b)

Chapter 3

Variation of Kerr microscopy depending upon the magnetic sample configuration. Figures are adopted from [120] and [121] respectively.

3.3.2 Differential Kerr microscopy

The p-MOKE can also be used as powerful method to directly visualize the magnetic domain structures by integration of microscope. This is called the Kerr microscope (Fig. 3.7). In conventional Kerr microscope, a regular wide-field microscope is employed to capture the image of the lateral distribution of magnetization from the region of interest on the sample. Single objective lens is commonly utilized for both the incident linearly polarized light, and the reflected circular polarized light at the same time. By using a beam splitter, the only reflected light enters through the analyzer and oppositely magnetized domains can be visualized as dark or bright image contrast based on the changes of Kerr rotation θ_k . We preset the analyzer in a way that a dark and bright contrast corresponds to \uparrow and \downarrow domain configuration of Co layer, respectively.

However, in some cases, the difference in contrast corresponding to each opposite domain configuration is not sufficient to distinguish their changes. Also, non-magnetic defects on the sample sometimes contribute to an undesirable contrast thereby leading to the difficulties on the reliable measurement. Both issues can be resolved by utilizing a differential mode in a Kerr microscopy. In a differential mode, a reference image defined at the initial magnetic state is first captured and then digitally saved by camera integrated on microscope. The subsequent image captured from the camera is then digitally subtracted from the reference image. As a result, the non-magnetic defects are eliminated and only change of magnetic contrast are shown in the processed image. In case of DW motion, a displacement of DWs yields to the expansion or reduction of one side of domain, thereby resulting a change in magnetization compared to the initial state. Consequently, the differential image shows a dark or bright contrast only in the area where DWs are displaced. Exemplary differential Kerr images of DW motion in FM and SAF are shown in Fig. 3.8. By increasing a number of averaging on images, the contrast and the quality of image can be further improved [1].

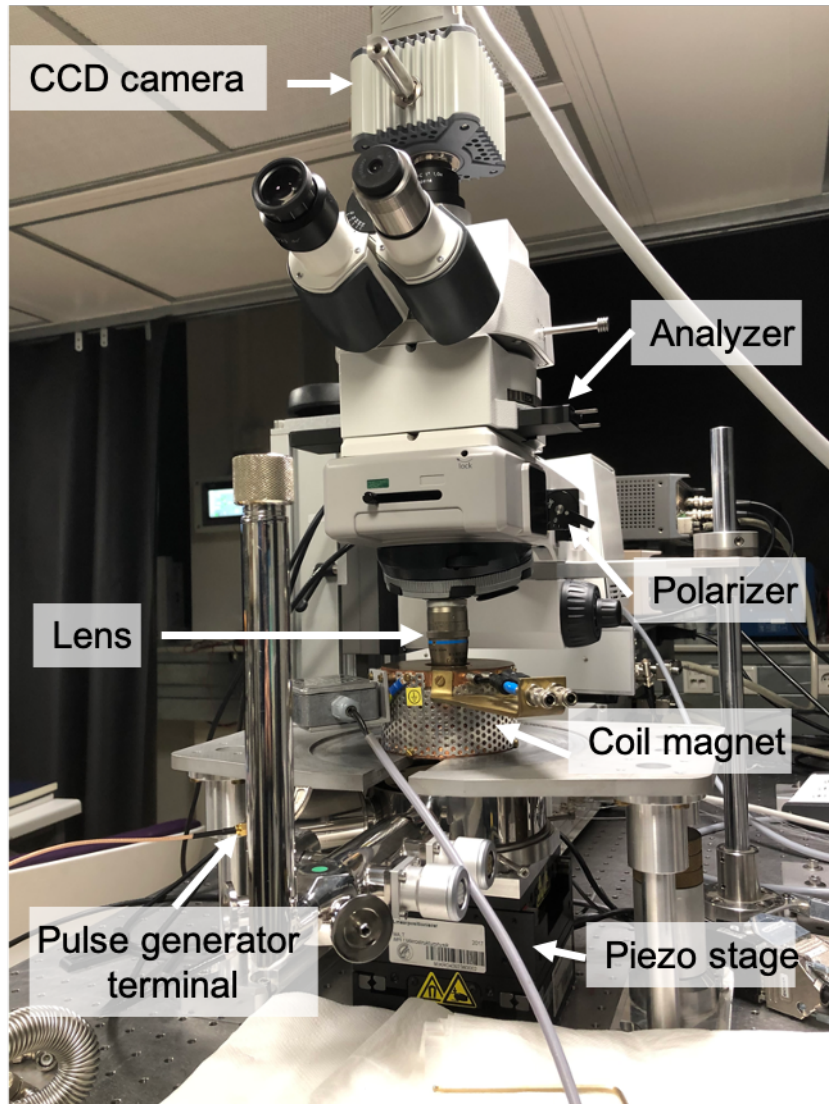


Figure 3.7. Kerr microscope setup. LED light source is connected to the polarizer via optical fibers, and the linearly polarized light illuminates to magnetic sample on the piezo stage. Reflected light passes through analyzer with Kerr rotation and captured by charge-coupled device camera.

3.3.3 Measurement of domain wall velocity

For CIDWM experiments, racetrack nanowire devices were loaded on the customized holder, which has two terminal pads, source and ground, available for applying a DC and RF source. We prepared the two big contact pads linked to the nanowire racetrack on the device for each connection. One of the pads is connected to the pulse generator, and another is electrically grounded. Different pulse generators are chosen depending on the range of pulse length applied to the sample. For the short pulse length in a range of 1-100 ns, Tektronix PSPL 10300B pulse generator is employed, while Keithley 2600 is used for applying a long pulse length in a range of 1-1000 ms. By utilizing a biased tee, the resistance of device is monitored by multimeter with a small DC current of 10 μ A. Combined with the electrical set-up, an electromagnetic coil magnet can be installed to the sample for applying an out-of-plane magnetic field up to magnitude of ± 0.05 T. The magnet is designed to closely surround sample inside, thus applying a uniform field. On the other hand, the specialized magnet setup is required in order to apply a further higher magnetic field up to magnitude of ± 0.5 T.

The procedure for the DW velocity measurement is following. Firstly, the initial position of DW is captured for the reference image at the stationary state using differential mode in Kerr microscope. Afterwards, a series of electrical pulses having a pulse length t_p in varying voltages are sent by pulse generator and DW moved with the distance d from the initial position. Although DW motion responses to a roughly same time scale as nanoseconds range of pulses, the image capture rate of camera in Kerr microscope is in milliseconds range. Hence, the final image is only collected after the completion of applying current pluses, and the total distance of DW motion is measured by the subtraction of reference image (see Fig. 3.8). As a result, the DW velocity v is calculated by the following equation as $v = \frac{d}{t_p}$. This procedure was repeated for ten times at each condition and averaged for statistics.

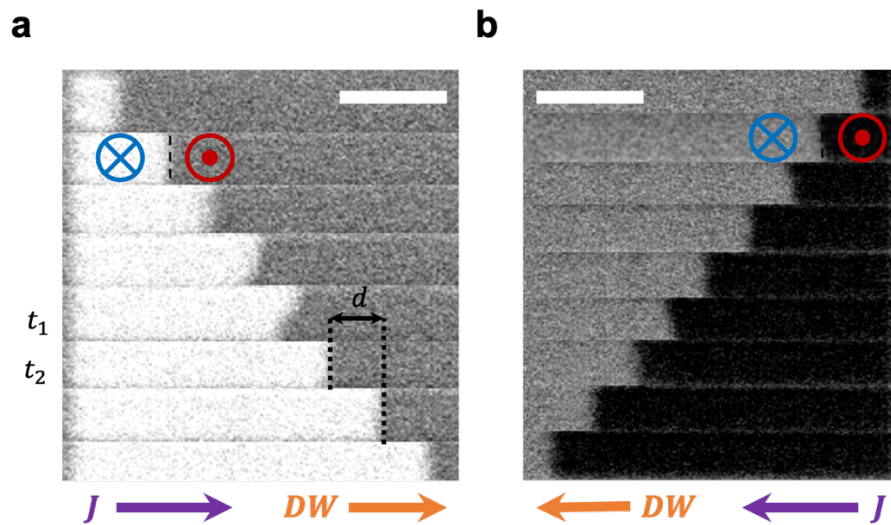


Figure 3.8. Exemplary differential Kerr microscopy images of domain wall motion. CIDWM in FM racetrack nanowire with a down-up ($\otimes|\odot$) domain configuration. Note here that white and black contrast correspond to down and up configuration, respectively. Domain wall moves towards right (a) and left (b) depending upon the current flow direction. DW displacement d is observed after applying series of pulses with a pulse length $\tau_p = t_2 - t_1$. Scale bars represent $5 \mu\text{m}$.

Chapter 4 Experimental results

In this chapter, we present the experimental results of the first demonstration of chiral magnetic domain wall motion in synthetic antiferromagnet (SAF)-ferromagnet (FM) lateral junction. First, we discuss the magnetic properties of SAF in comparison to FM structure (section 4.1) and the transformation from SAF to FM via oxidation process (section 4.2). On the basis of this finding, we introduce the concept and realization of SAF-FM lateral junction in racetrack nanowire (section 4.3). At last, we show the demonstration of chiral domain wall motion in FM, SAF, and SAF-FM lateral junction by electrical current (section 4.4) and magnetic field (section 4.5) to compare their dynamics in each region, respectively.

4.1 Magnetic properties of ferromagnets and synthetic antiferromagnets

The magnetic hysteresis loops of FM and SAF structures are obtained by performing vibrating sample magnetometer (VSM) at room temperature to investigate their magnetic properties of blanket films. The film structures of each sample are as following. Both SAF and FM have a common underlayer with 20 TaN | 30 Pt grown on Si | SiO₂ substrates (all thicknesses are given in Å). Here, note that Pt layer hosts a strong interfacial perpendicular magnetic anisotropy (PMA) and a proximity-induced magnetization on adjacent Co layer [25]. In case of FM, the magnetic layers are composed of multi stacks of 3 Co | 7 Ni | 3 Co, and they behave as a single magnet. As shown in Fig. 4.1a, the hysteresis loop of FM clearly shows the strong PMA with a coercivity $H_c^{FM} \sim 0.1$ kOe along the out-of-plane orientation. Field scanning along the in-plane orientation confirms that there is no hysteresis with a strong effective anisotropy field $H_{K_{eff}} \sim 10$ kOe as shown in Fig. 4.1.b. The saturation magnetization is obtained to $M_s^{FM} \sim 610$ emu/cc converted from the saturation moment $m_s^{FM} \sim 20$ μ emu by dividing total area and thickness of magnetic layer.

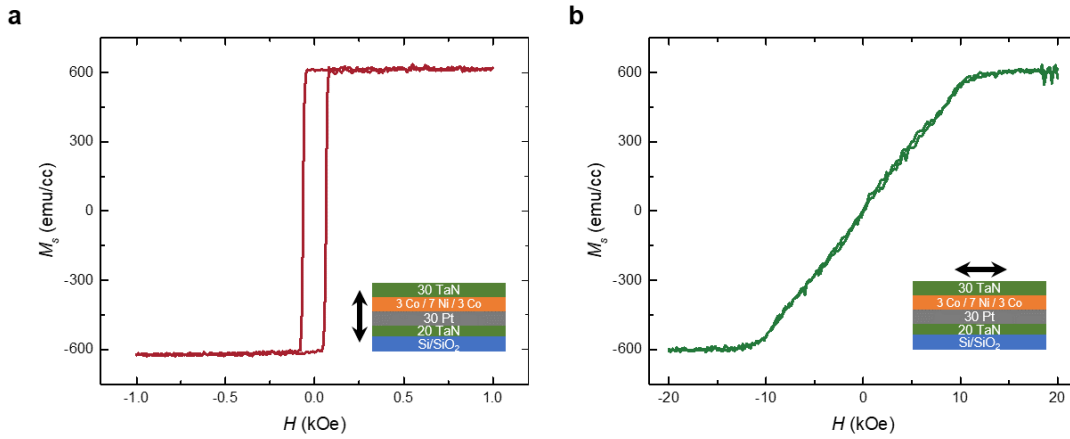


Figure 4.1. M - H hysteresis loops of single layer FM structure. M versus H loops of FM film along the magnetic (a) easy-axis and (b) hard-axis. Insets illustrate the detailed film structures with an applied magnetic field direction, respectively.

The magnetic hysteresis loop of SAF structure is more complicated than FM case. In equilibrium, SAF is composed of two FM layers which are antiferromagnetically coupled to each other through an atomically thin non-magnetic spacer. For the simplicity, here, we define two FM layers as lower magnetic layer (LM: 3 Co | 7 Ni | 1.5 Co), and upper magnetic layer (UM: 3.5 Co | 7 Ni | 3 Co). The non-magnetic layers are typically chosen among 3d, and 4d transition metals, such as Ru, Ir, and Rh [34]. Note that the strength of AF coupling is extremely sensitive to the thickness of spacer layer by following interlayer RKKY interaction. In this study, we employed the 9.5 Ru as a spacer layer for achieving SAF structure.

As shown in Fig. 4.2, magnetic hysteresis loops of grown SAF structure clearly show AF coupling state by measuring plateau region with nearly zero net moment at a zero field. In AF state, here, moments of LM and UM are aligned to antiparallel configuration ($m_{LM}^{\uparrow} - m_{UM}^{\downarrow}$ or $m_{LM}^{\downarrow} - m_{UM}^{\uparrow}$). To break antiparallel AF state, a very large magnetic field is required which is a spin-flop transition field $H_{sf}^{SAF} \sim 3$ kOe. This spin-flop transition clearly shows that the AF exchange coupling is large compared to the anisotropy of the FM layers. At zero field, m_{LM} and m_{UM} are nearly compensated so that the remnant moment is almost zero, m_R^{SAF} ($|m_{LM}^{SAF} - m_{UM}^{SAF}| \sim 1 \mu\text{emu}$). To achieve nearly compensated SAF, we designed slightly thicker UM compared to LM, in which proximity induced magnetization is induced by Pt | Co bottom interface. Consequently, we obtained the ratio of the LM to UL moment $\frac{m_{UM}}{m_{LM}} \sim 1.05$. The

saturation field, namely an exchange field, is observed $H_{ex} \sim 10$ kOe along magnetic easy axis with the saturation magnetic moment of $m_s^{SAF} \sim 40$ μemu . In saturation regime, total moments of both LM (m_{LM}^{SAF}) and UM (m_{UM}^{SAF}) are parallel to one another so that m_s^{SAF} can be simply calculated by the relation of $m_s^{SAF} = m_{LM}^{SAF} + m_{UM}^{SAF}$.

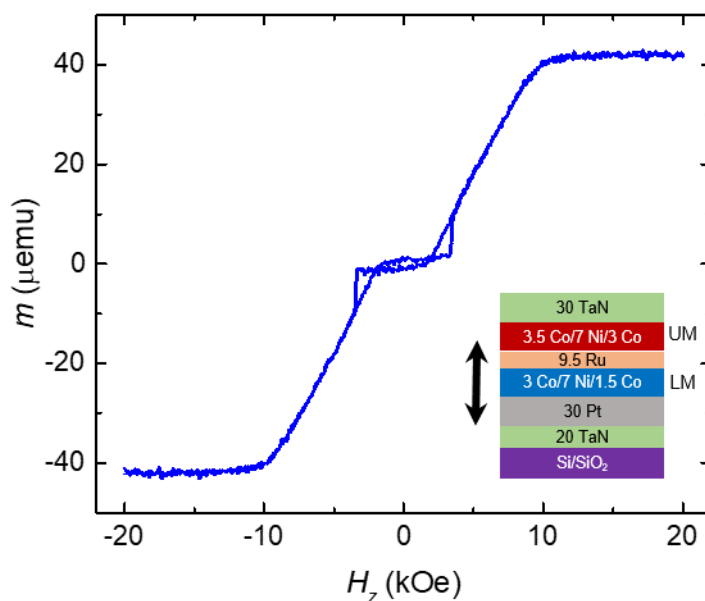


Figure 4.2. Magnetic easy-axis hysteresis loop of SAF structure. Magnetic hysteresis loops, with moment m versus field H_z of SAF structure. Inset illustrates the detailed film structure with an applied field direction.

4.2 Effect of oxidation on the magnetic properties of synthetic antiferromagnets

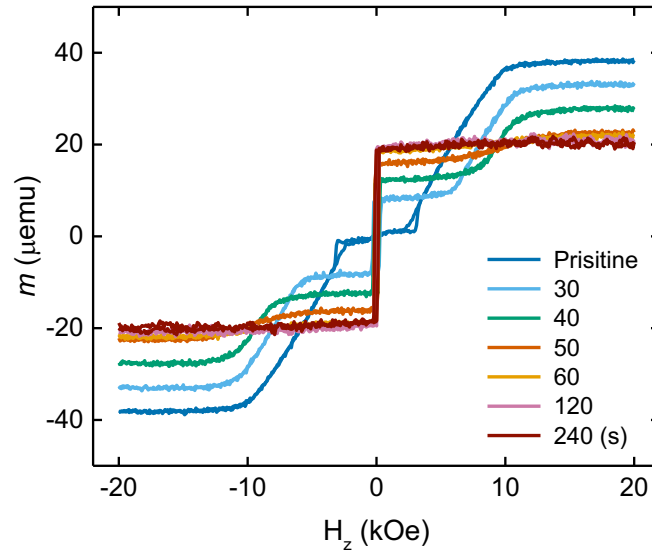


Figure 4.3. Effect of oxidation process upon the SAF structure. Magnetic hysteresis loops of SAF film along the magnetic easy-axis as a function of plasma oxidation process time. Figure is adopted from [50]

As shown in previous section, atomically thin layers and their interfaces play key roles to determine distinct magnetic properties. Considering the structural similarity of SAF and FM, we found that the manipulation of degree of surface oxidation SAF can give rise to transformation from SAF to FM by post plasma oxidation process. Fig. 4.3 shows M-H hysteresis loops of SAF as a function of plasma oxidation process time along the magnetic easy-axis. The plasma oxidation process was carried out on blanket film using reactive ion etching (RIE) tool at room temperature. By increasing the process time, the remnant moment of SAF m_R^{SAF} gradually increases while the exchange field H_{ex} still remains ~ 10 kOe up to 50 sec of process time (orange line). This indicates that the oxidation changes the moment compensation by reducing the magnetic moment of UM but it does not affect to the exchange coupling strength. Eventually, both m_S^{SAF} and m_R^{SAF} gradually decrease and increases, respectively, and converge to $20 \mu\text{emu}$ after 50 sec of process time. As for 60 sec oxidation process (yellow line), the hysteresis loop shows a clear transition from SAF to FM state that is

confirmed by the disappearance of AF coupling. Contrary to the gradual changes of m_s^{SAF} and m_R^{SAF} , H_c abruptly appears even through the relatively short process time around 30 sec by reducing more than one order of magnitude compared to H_{sf}^{SAF} and converges to ~ 0.1 kOe over 60 sec as well. After 60 sec, interestingly, it is found that magnetic properties do not significantly change and maintain as it is similar to 60 sec over even further oxidation time up to 240 sec (red line). As a result, we observed complete SAF to FM transformation.

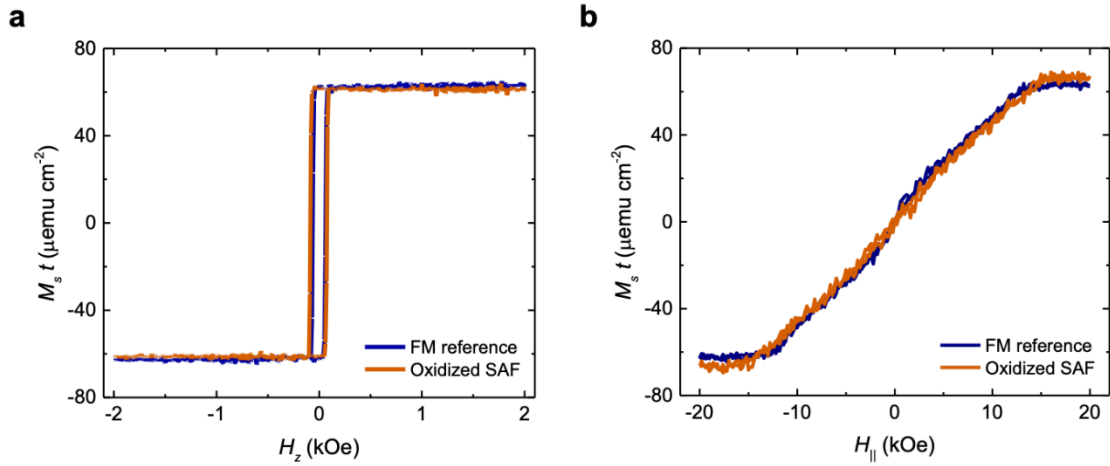


Figure 4.4. Comparison of magnetic properties between oxidized SAF and as-grown FM. Magnetic hysteresis loops of oxidized SAF (orange) and reference FM (dark blue) measured along (a) easy axis, and (b) hard axis. Saturation magnetization per unit area ($M_s t$) is obtained for direct comparison. Figure is adopted from [50]

For direct comparison, we prepared a control FM film which is identical to the LM of SAF (20 TaN | 30 Pt | 3 Co | 7 Ni | 1.5 Co | 9.5 Ru | 30 TaN). Note that Ru layer is inserted in between Co and TaN capping layer to preserve the interfacial anisotropy of LM as same as reference SAF. As shown in Fig. 4.4a and b, the magnetic properties of the oxidized SAF (process time of 60 sec) are identical to the FM control film both along the easy and hard axis. Note that we compared the saturation magnetization per unit area, $M_s t$, instead of magnetization due to the presence of oxidized UM layer of SAF. Both oxidized SAF and reference FM film, $M_s^{Ox.SAF} t \approx M_s^{FM} t \sim 60 \mu\text{emu cm}^{-2}$ were measured and show the coercivities $H_c^{Ox.SAF} \approx H_c^{FM} \sim 0.1$ kOe along the easy axis (Fig. 4.4a). Moreover, the hard axis measurement of oxidized SAF clearly show the linear response to field ramping with no hysteresis loop and large anisotropy field $H_K^{Ox.SAF} \sim 12$ kOe. These results provide strong

Chapter 4

evidence that the oxidation process does not affect the magnetic properties of the LM at all, such as anisotropy [9], [122], while completely suppressing the FM properties of the UM of SAF.

4.3 Synthetic antiferromagnet-ferromagnet lateral junctions

Based on the findings presented above, we introduce the novel concept of device, namely SAF-FM lateral junction. The junction is readily defined by the conventional lithography combined with plasma oxidation process. The oxygen plasma is globally applied to entire sample, but only the SAF region where the resist mask is uncovered is oxidized thus transforming to FM.

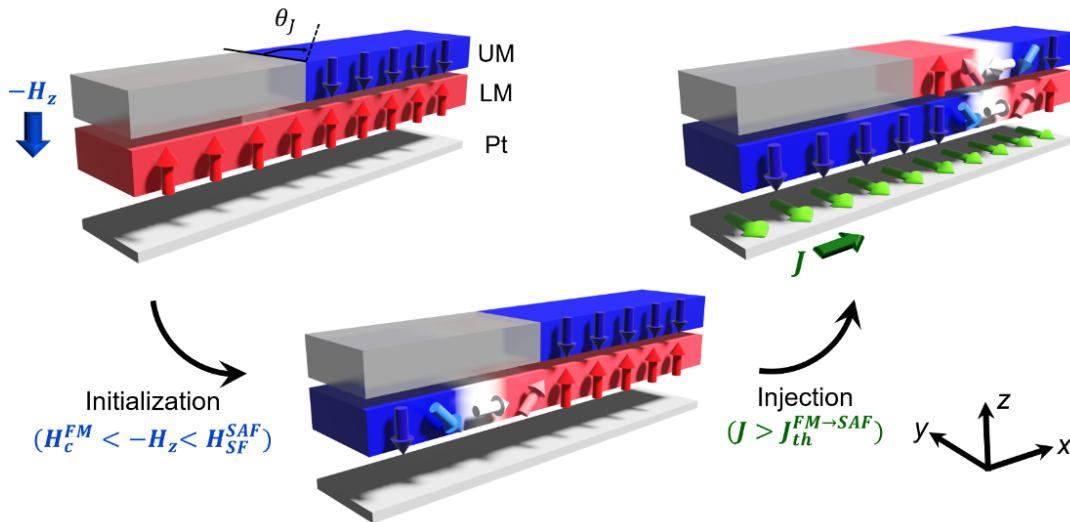


Figure 4.5. Schematic illustrations of working principle of SAF-FM lateral junction. Chiral DW is initialized by applying an external magnetic field H_z along the magnetic easy-axis opposite to the initial orientation of moment of the lower magnetic layer (LM). After initialization, the DW is injected into SAF region by an electrical current. Figure is adopted from [50]

Working principle of SAF-FM lateral junction is discussed as below. Let us assume that the junction is integrated in racetrack nanowire device where the chiral magnetic DW can be manipulated by an electrical current. Note that Néel type DW is configured in both SAF and FM due to the interfacial DMI at Pt | Co interface. At the junction, DW can be readily generated

by applying an external magnetic field H_z along the easy-axis. As the direction of H_z is opposite to the initial orientation of the LM, the magnetic moment reversal occurs solely in the FM region as shown in Fig.4.5. Note that the magnitude of H_z is larger than H_c^{FM} but smaller than H_{sf}^{SAF} . While the FM region is switched, the LM of SAF still maintain its initial state due to the strong interlayer AF coupling to the UM. Hence, the DW is generated in the LM region at the junction boundary. Afterwards, initialized DW can potentially move into both FM region and SAF region by an electrical current, thereby allowing us deterministic DW injection in SAF. The experimental demonstrations including DW initialization, and its motion will be presented in following sections.

4.3.1 Fabrication of SAF-FM junction in racetrack nanowire

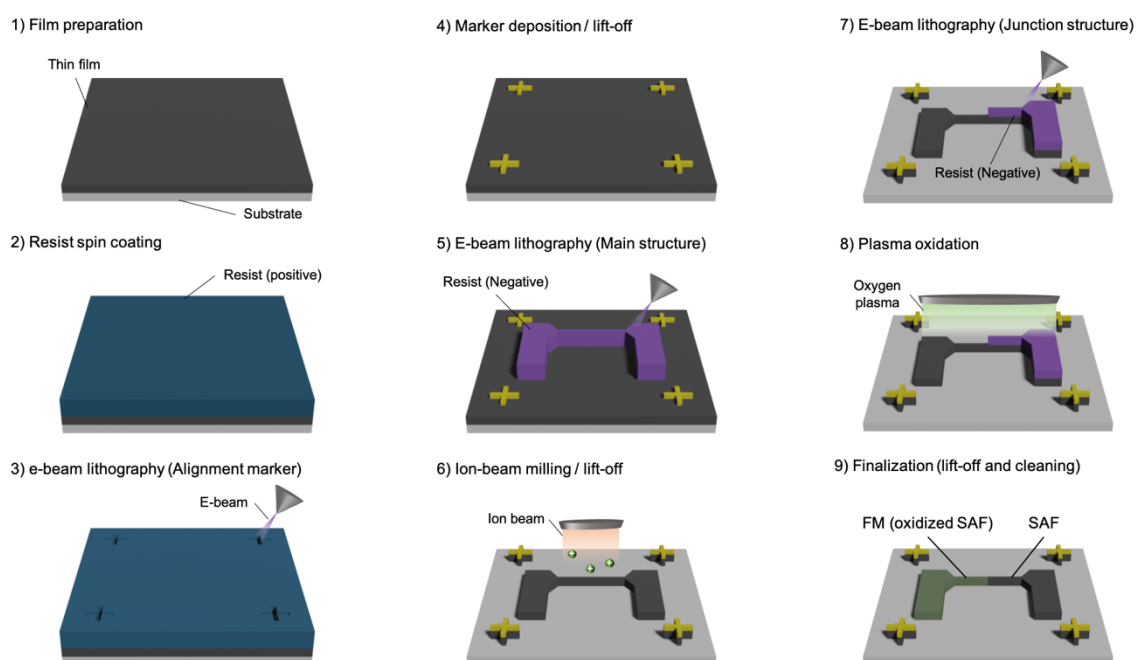


Figure 4.6. SAF-FM lateral junction fabrication process flow. SAF-FM lateral junction is integrated in racetrack nanowire by an e-beam lithography and plasma oxidation process. Resist mask protects the SAF region (grey), whereas the uncovered area is oxidized and becomes the FM region (green) during the process.

Detailed fabrication process flows of racetrack wire and the junction are shown in Fig. 4.6. Prior to junction integration, we first prepared the racetrack device with pristine SAF film by conventional e-beam lithography and ion beam etching process (step 5 and 6). To avoid undesirable oxidation during plasma process, alumina (AlOx) was refilled on etched region as a passivation layer. Secondary e-beam lithography was applied to define the junction pattern on the top of racetrack wire (step 7). Due to the flexibility in lithography, the shape of resist masks can be potentially varied by the design. In this study, prepared the junction with various junction tilting angles θ_j ($0^\circ < \theta_j < 60^\circ$) with respect to the direction transverse to the wire. Afterwards, oxygen plasma process was performed on the entire sample for 60 sec in the presence of resist masks (step 8). Here, the typical thickness of e-beam resist mask being used in this study is around 400 nm, and the etching rate of the resist by plasma process is measured to be ~ 3 nm/sec, hence it is sufficient to protect SAF underneath a mask during process. The region where the resist mask is uncovered becomes FM state (green region in step 9), whereas others still preserve SAF properties (grey region in step 9). As a result, we successfully fabricated the SAF-FM lateral junction along the racetrack nanowire.

4.3.2 Field-induced deterministic domain wall initialization

In general, the device has been characterized to single domain state after fabrication in which the orientation of magnetization of the LM of the SAF and the FM (oxidized SAF) are all aligned in same direction (Fig. 4.7a). Thus, the DW initialization is challenge and it has been generally performed in a stochastic manner relying on random nucleation process by applying either large current or field. At this junction, however, we demonstrated the deterministic DW initialization by simply applying an external magnetic field. Here, the direction of field is opposite to the initial orientation of LM of SAF which is common to the FM region. Initial orientation of LM was set to be upwards to the film plane ($+m_z^{LM}(\uparrow)$, $+z$ -direction) as shown in Fig. 4.7b. Thus, the field was applied to the direction of $-H_z$ with the magnitude of ~ 120 Oe, which is slightly above the H_c^{FM} (~ 100 Oe). As discussed in section

4.3, the magnitude of field can be chosen within the range of $H_c^{FM} < |H_z| < H_{sf}^{SAF}$. Consequently, a single DW is successfully initialized at the junction boundary with the DW configuration of $\downarrow\uparrow$. This initialization process applies in the opposite configuration as well (Fig. 4.7c). Black and white color contrast in Kerr image correspond to the moment oriented to up (+z), and down (-z), respectively.

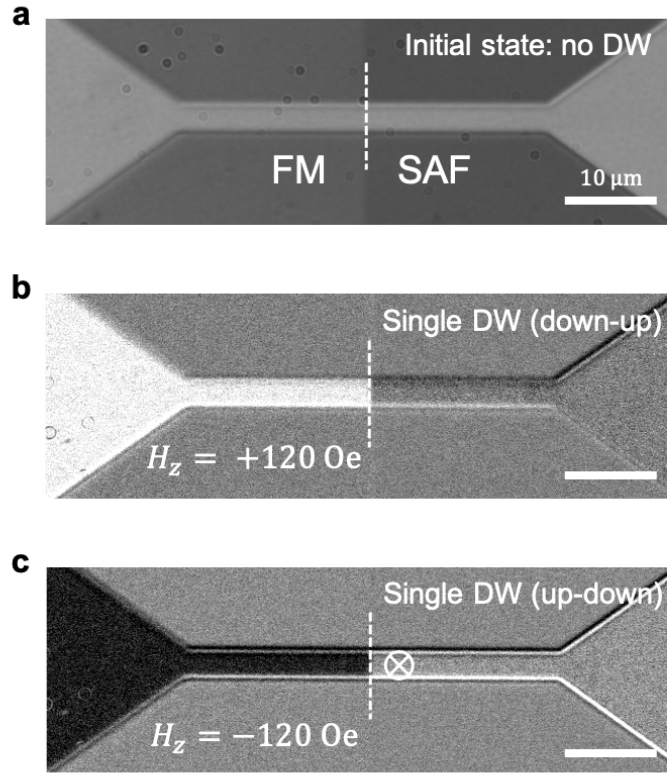


Figure 4.7. Field-induced deterministic DW initialization. (a) Microscope image of SAF-FM lateral junction device with no DW. Kerr images of single DW initialized at the junction with (b) $\odot|\otimes$ (up-down) and (c) $\otimes|\odot$ (down-up) configuration. Dashed lines depict the junction boundary and scale bars represent 10 μm .

After initialization, the DW readily moves into FM region from the junction by applying an electrical current (see left panel in Fig. 4.8). Here, the minimum current density required to initiate DW motion is defined as the threshold current density J_{th} , thus the applied current density J is above that threshold in this case ($J > J_{th}^{un \rightarrow FM}$). The further current was applied in the forward direction, the more the DW moved inside FM region ($J > J_{th}^{FM}$). Interestingly, we found that the DW can also be injected into SAF from the junction by

applying current to opposite direction ($J > J_{th}^{J_{un} \rightarrow SAF}$) and it further moves inside SAF as well ($J > J_{th}^{SAF}$) (see right panel in Fig. 4.8). In this case, the $J_{th}^{J_{un} \rightarrow SAF}$ seems to be substantially higher than those of both FM and SAF case. In following sections, we will discuss about the current-induced DW motion in the junction and the relation of current densities depending upon the region in more details.

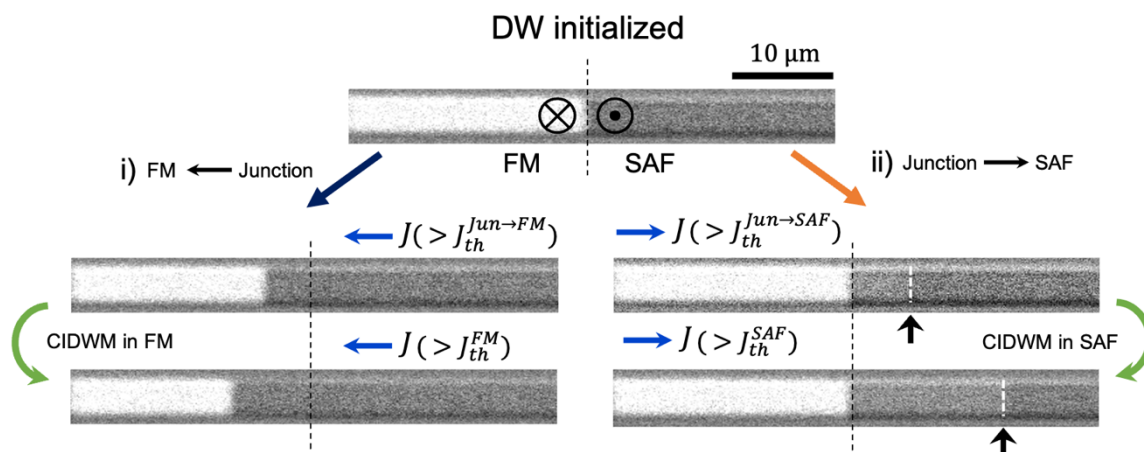


Figure 4.8. Demonstration of CIDWM in FM, SAF, and SAF-FM junction. After field-induced DW initialization at the junction, DW moves towards i) FM region, and ii) SAF region by corresponding current direction. Note that the DW is initialized to $\otimes|\odot$ (down-up) configuration. Black dashed lines represent the junction boundary, and white dashed lines with black arrows indicate the DW in SAF region. Scale bar is common for all images.

4.4 Current-induced domain wall motion in SAF-FM lateral junctions

At the junction integrated racetrack device, we performed the electrical current-induced DW motion (CIDWM) in the FM, the SAF, and the junction, respectively. The DW motion can be mainly defined by two different dynamic regimes, the flow and creep regimes. In flow regime, the DW motion is dominated by the current driven torque with no assistance from thermal fluctuations. Typical time scale of energy transfer by current driven torque is known to be short in FM based system, within nano second range of pulse length, thereby needed a relatively large current density. On the other hand, the thermally assisted DW motion is mainly governed by the thermal activation in which the DW depins above the activation energy barrier. In general, the time scale for the thermally assisted DW motion is very long compared to the flow motion. Therefore, CIDWM has to be performed in both flow and thermally assisted regime with a various range of pulse length to understand the DW dynamics of the system in a thorough manner. In this study, we employed the various pulse lengths for CIDWM in a range of from 5 to 100 ns for flow motion, and 10 ms to 5 s for thermally assisted motion, respectively.

4.4.1 Ferromagnet region

4.4.1.1 Domain wall motion in flow regime

First, we demonstrated the CIDWM in the FM region which is formed by the oxidation on SAF. Despite the identical magnetic properties, it is essential to evaluate the DW motion compared to the pristine FM since the DW motion is critical to local defects which can be potentially created during fabrication process. The racetrack nanowire device is formed by the dimension of $3 \times 40 \mu\text{m}$ and the resistance of device is measured to be approximately $1.6 \text{ k}\Omega$ at room temperature (see Fig. 4.9a). Fig. 4.9b depicts the current density J dependence of DW velocity v^{FM} in the FM region. To investigate the high velocity motion in flow regime, we applied series of current pulses with a short pulse length τ_p^J range from 5 to 100 ns. Interestingly,

the maximum velocity v_{max}^{FM} is achieved up to $\sim 90 \text{ ms}^{-1}$ at $J \sim 1.0 \times 10^8 \text{ A cm}^{-2}$ with $\tau_p^J = 5 \text{ ns}$ and this result corresponds to the previous reports obtained from similar structures of pristine FM [6], [25].

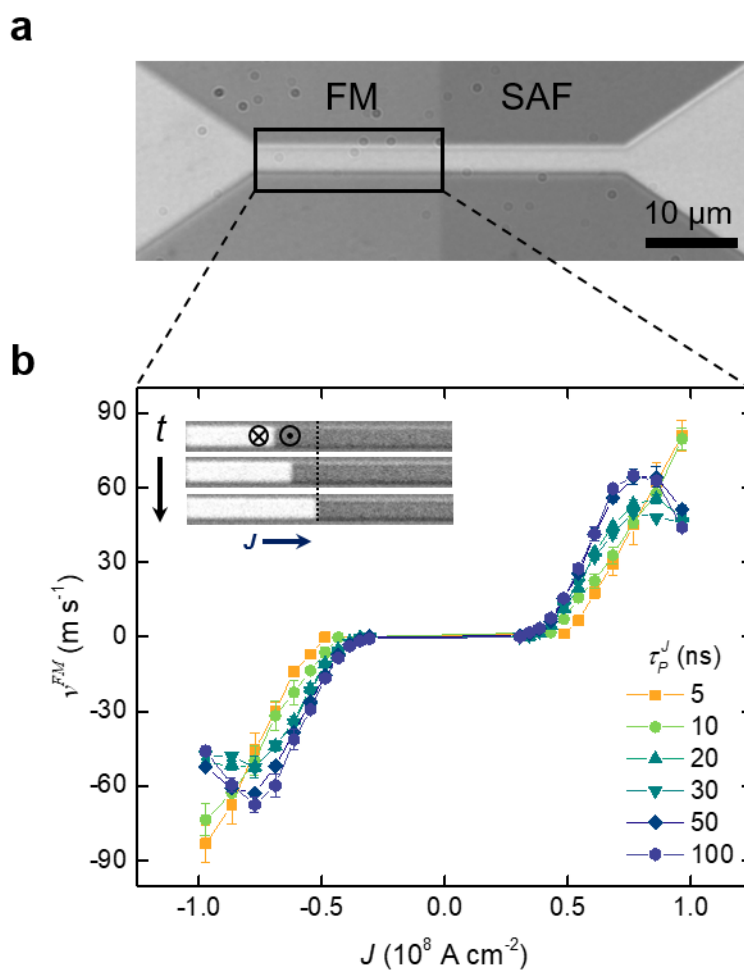


Figure 4.9. Current density dependence of the DW velocity in the FM region. **a**, Optical microscope image of SAF-FM lateral junction integrated racetrack nanowire. CIDWM is performed within the FM region (black solid box). **b**, DW velocity versus the current density at various pulse duration ($\tau_p^J = 5, 10, 20, 30, 50,$ and 100 ns). Inset shows exemplary Kerr microscope images of sequential DW motion performed in the FM region. Dashed line defines the boundary of the SAF-FM junction, and the dark blue arrow indicates the current flow

direction corresponding to images. Each point is averaged out of 10 times of measurement, and error bars are standard deviation.

The v_{max}^{FM} and the profile of v^{FM} as a function of J exhibit overall similar tendency at $\tau_p^J = 5$ and 10 ns by showing the positive derivative of v^{FM} in all range of J . In case of longer pulse duration ($\tau_p^J \geq 20$ ns), however, the variation of v^{FM} is no longer monotonic as J increases, but it decreases down to $v^{FM} \sim 50 \text{ ms}^{-1}$ at above $J > 0.7 \times 10^8 \text{ A cm}^{-2}$. In particular, the decrement of the velocity Δv^{FM} is more significant at $\tau_p^J \geq 50$ ns, compared to $\tau_p^J = 20$, and 30 ns.

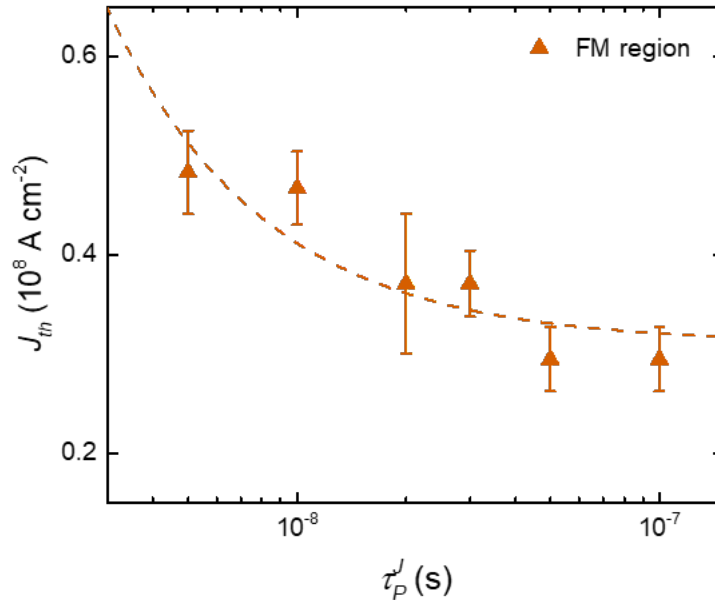


Figure 4.10. Pulse length dependence of the threshold current density for flow DW motion in the FM region. $J_{th,flow}^{FM}$ versus τ_p^J (5, 10, 20, 30, 50, and 100 ns) of flow DW motion in FM region. The dashed curve represents to fit and error bars correspond to the standard deviation.

In addition, the pulse length dependence of threshold current density in flow regime is shown in Fig. 4.10. In flow regime, the threshold current density $J_{th,flow}^{FM}$ can be defined as the minimum J corresponds to those of $v^{FM} \geq 5 \text{ ms}^{-1}$. We observe that the $J_{th,flow}^{FM}$ gradually decreases as τ_p^J increases thereby resulting $J_{th,flow}^{FM} \sim 0.3 \times 10^8 \text{ A cm}^{-2}$ at $\tau_p^J = 100$ ns, which

Chapter 4

is reduced by 40% from those measured at $\tau_p^J = 5$ ns ($J_{th,flow}^{FM} \sim 0.5 \times 10^8$ A cm⁻²). The data is fitted by the relation $J_{th,flow} - J_{th_0,flow} = \frac{1}{\tau_p^J}$ (orange dashed line) [107], and this fit yields $J_{th_0,flow}^{FM} \sim (0.31 \pm 0.02) \times 10^8$ A cm⁻² which is the intrinsic threshold current density in FM region considering with no thermal fluctuation.

4.4.1.2 Domain wall motion in thermally assisted regime

In thermally assisted regime, the DW motion does not rely on the current driven torque efficiency, but it is dominated by the thermal activation phenomena. As discussed in section 2.3.3, the current driven torque is dominant when the applied current density is large enough, therefore the thermal assisted DW motion typically occurs at relatively lower applied current density with longer time scale. This main difference gives rise to the very slow DW motion in thermally assisted regime, typically $v_{DW} < 5 \text{ ms}^{-1}$, compared to the flow regime and the DW moves like “creeping” by overcoming the pinning barrier. Therefore, we performed the DW depinning measurement to evaluate the thermally assisted DW motion in FM region.

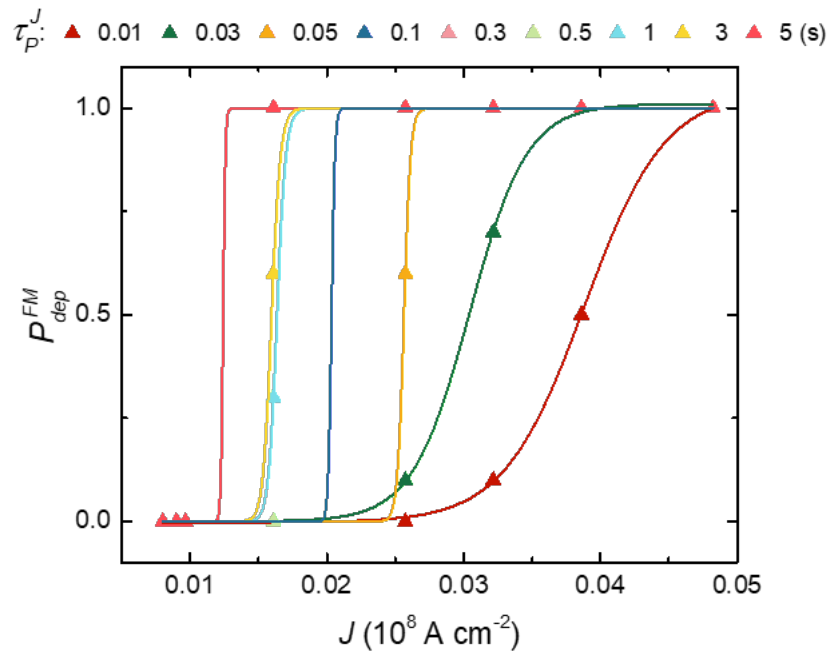


Figure 4.11. DW depinning probability versus applied current density in the FM region. Current-induced DW depinning probability as a function of current density for various current pulse lengths τ_p^J (10 ms to 5 s). Solid curves fit to standard error function profile. Figure is adopted from [50]

Fig. 4.11 shows the depinning probabilities P_{dep}^{FM} as a function of applied current density for various τ_p^J (10 ms to 5 s). The DW depinning was observed by differential mode Kerr

microscopy, thus detecting the displacement of DW before and after the single pulse. Overall, we found that the depinning occurs at relatively low current level compared to flow regime. Note that we applied single current pulse for each measurement to avoid additional Joule heating effects. For the reliable quantification, the DW depinning measurements were carried out at many different points within FM region for ten times at each position. This procedure allowed us to exclude the effect of any local defects, such as line edge roughness of wire. The P_{dep}^{FM} versus J distributions for short τ_p^J (< 50 ms) are broader than those for long τ_p^J (> 50 ms), which implies that the thermal contributions for depinning become more dominant as τ_p^J increases.

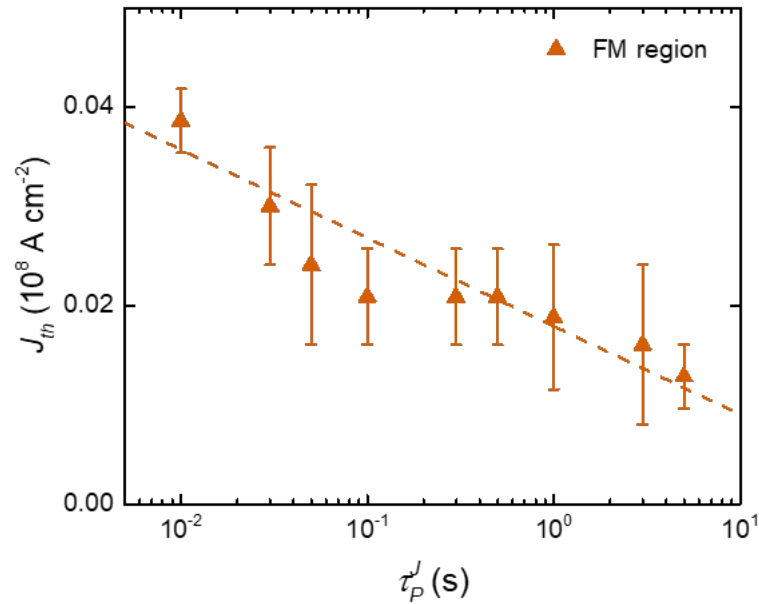


Figure 4.12. Pulse length dependence of the threshold current density for thermally assisted DW depinning in the FM region. $J_{th,flow}^{FM}$ versus τ_p^J (10 ms to 5 s) of thermally assisted DW depinning in FM region. The dashed line represents to fit and error bars correspond to the 25/75% probabilities.

Based on depinning probabilities shown in Fig. 4.11, we determine the threshold current density for thermally assisted DW depinning $J_{th,therm}^{FM}$ as the value of J corresponds to the $P_{dep}^{FM} = 0.5$ at each τ_p^J (see Fig. 4.12). Compared to the flow regime, $J_{th,therm}^{FM}$ reduces about one order of the magnitude ($J_{th,therm}^{FM} \sim 0.04 \times 10^8 \text{ A cm}^{-2}$ at $\tau_p^J = 10$ ms), which is even

smaller than intrinsic threshold current density in flow regime ($J_{th,flow}^{FM} \sim 0.3 \times 10^8 \text{ A cm}^{-2}$). This clearly indicates that the thermal activation gives rise to the DW depinning not a highly efficient current driven torque. In addition, we observe that the $J_{th,therm}^{FM}$ decreases linearly as τ_p^J increases on a logarithmic scale by fitting data. Since the thermal activation is known to be based on the Arrhenius-law, thereby allowing us to fit to exponential relation ($J_{th,therm}^{FM} \propto \ln \tau_p^J$).

4.4.2 Synthetic antiferromagnet region

4.4.2.1 Domain wall motion in flow regime

The DW motion in SAF region was performed in flow regime as shown in Fig. 4.13. Due to the exchange coupling torque (ECT), the DW moves in SAF much faster than conventional single FM thereby showing the maximum velocity up to $v_{max}^{SAF} \sim 400 \text{ ms}^{-1}$ at $J \sim 1.0 \times 10^8 \text{ A cm}^{-2}$ with $\tau_p^J = 5 \text{ ns}$ as shown in Fig. 4.13b (yellow square). This is four times faster than the FM case at same applied current density and pulse length (see section 4.4.1.1). Inset depicts the differential Kerr images of DW motion in SAF, which show very low contrast due to the nearly compensated net moment between LM and UM ($m_{UM}/m_{LM} \approx 1.05$). Note that the Kerr contrast of SAF originates from the strong spin-orbit coupling at the Pt/Co bottom interface, thereby representing the LM configuration. By comparing v_{max}^{SAF} for various τ_p^J , it gradually decreases down to $v_{max}^{SAF} \sim 200 \text{ ms}^{-1}$ as τ_p^J increases up to 100 ns without significant downturn which is contrast to the FM region.

Interestingly, the high efficiency of SAF stands out not only in increasing the velocity but also in lowering threshold current density compared to FM. As shown in Fig. 4.14, the threshold current density of DW motion in flow regime in the SAF $J_{th,flow}^{SAF}$ is found to be overall lower than $J_{th,flow}^{FM}$ under the same τ_p^J , thus showing $J_{th,flow}^{SAF} \sim 0.2 \times 10^8 \text{ A cm}^{-2}$ at $\tau_p^J = 100 \text{ ns}$. In addition, we obtained the intrinsic threshold current density for flow regime in the SAF $J_{th,flow}^{SAF} \sim (0.21 \pm 0.08) \times 10^8 \text{ A cm}^{-2}$ by fitting to the relation $J_{th,flow} - J_{th,flow} = \frac{1}{\tau_p^J}$ as same as in section 4.4.1.1 (blue dashed curve).

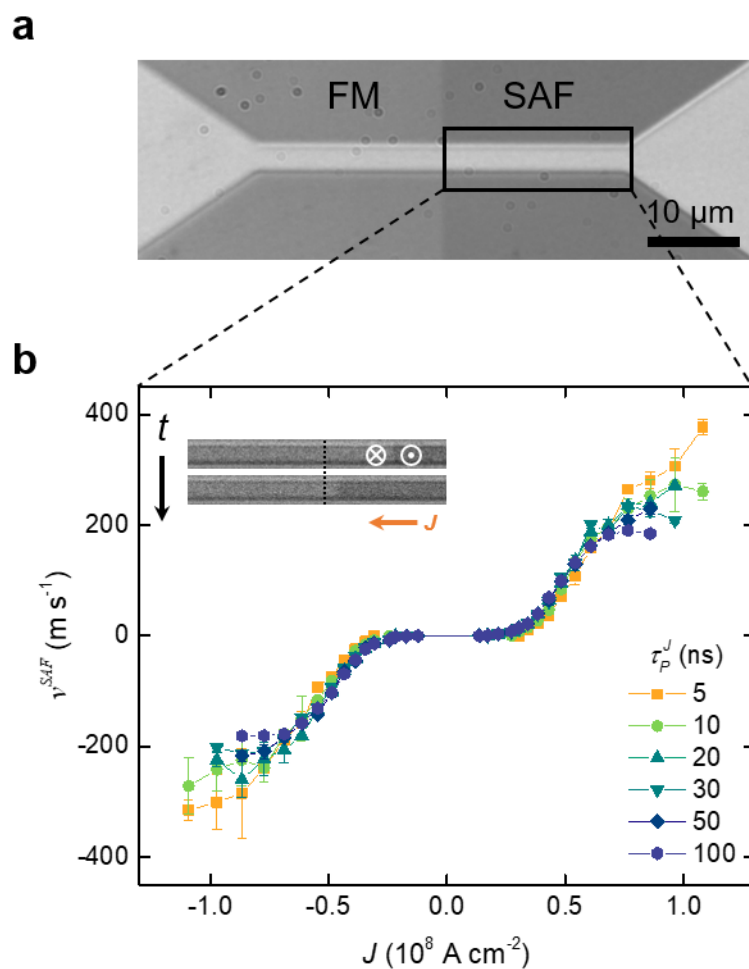


Figure 4.13. Current density dependence of the DW velocity in the SAF region. **a**, Optical microscope image of SAF-FM lateral junction integrated racetrack nanowire. CIDWM is performed within the SAF region (black solid box). **b**, DW velocity versus the current density at various pulse duration ($\tau_p^J = 5, 10, 20, 30, 50,$ and 100 ns). Inset shows exemplary Kerr microscope images of sequential DW motion in SAF region. Dashed line defines the boundary of the SAF-FM junction, and the orange arrow indicates the current flow direction. Error bars are standard deviation.

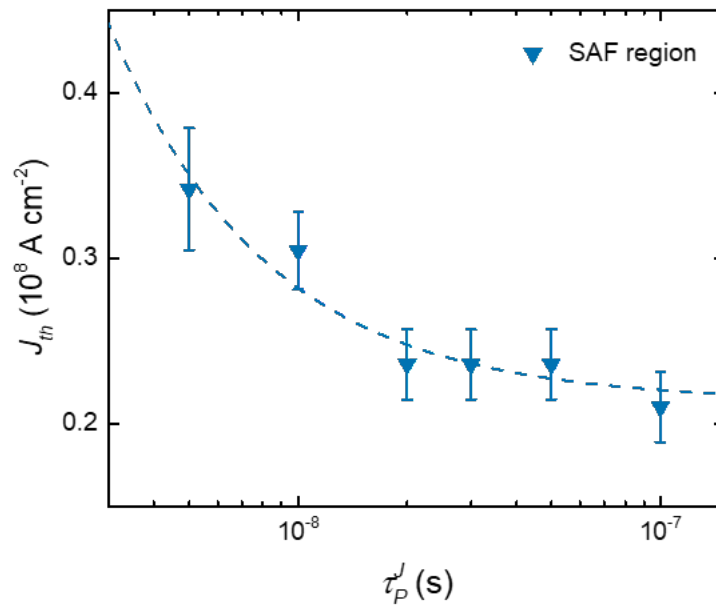


Figure 4.14. Pulse length dependence of the threshold current density for flow DW motion in the SAF region. $J_{th,flow}^{FM}$ versus τ_p^J (5, 10, 20, 30, 50, and 100 ns) of flow DW motion in SAF region. The dashed curve represents to fit and error bars correspond to the standard deviation.

4.4.2.2 Domain wall motion in thermally assisted regime

Thermally assisted DW motion in SAF region was investigated by applying a single current pulse with varying the τ_p^J from 10 ms to 5 s. As similar to the FM case, thermal activated DW depinning in SAF occurred at much lower current densities compared to those of the flow regime. Overall, applied current densities are even further lower than $J_{th0,flow}^{SAF} \sim (0.21 \pm 0.08) \times 10^8 \text{ A cm}^{-2}$, thereby confirming the thermal activation dominated mechanism. For statistics, we repeated the depinning measurements ten times under each condition as same as discussed in section 4.4.1.2. Fig. 4.15 depicts the DW depinning probabilities P_{dep}^{SAF} versus applied current density J at various τ_p^J .

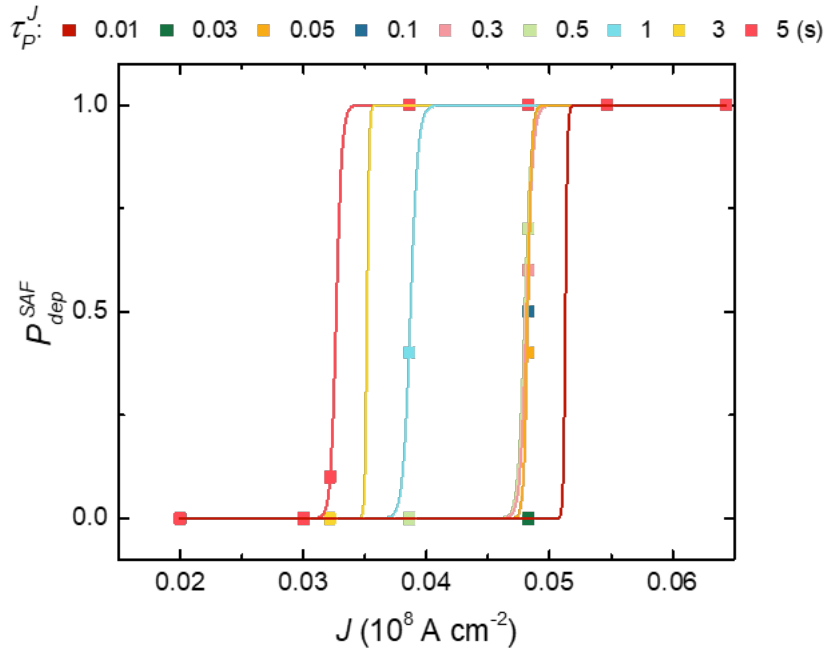


Figure 4.15. DW depinning probability versus applied current density in the SAF region. Current-induced DW depinning probability as a function of current density for various current pulse lengths τ_p^J (10 ms to 5 s). Solid curves fit to standard error function profile. Figure is adopted from [50].

Fig 4.16 shows the $J_{th,therm}^{SAF}$ as a function of τ_p^J varying from 10 ms to 5 s. Note that the $J_{th,therm}^{SAF}$ was determined by taking the values of J corresponding to $P_{dep}^{SAF} = 0.5$ at each τ_p^J in the same manner as discussed in section 4.4.1.2. Interestingly, the DW in the SAF region depins surprisingly at higher $J_{th,therm}^{SAF}$ compared to the FM region under same τ_p^J ($J_{th,therm}^{SAF} > J_{th,therm}^{FM}$), which is the opposite to the results observed from the flow regime ($J_{th,flow}^{SAF} < J_{th,flow}^{FM}$). Furthermore, the decrease in $J_{th,therm}^i$ ($i = FM$ or SAF) as τ_p^J increases from 10 ms to 5 s appears smaller in the SAF than FM, therefore the exponential relation fitting ($J_{th,therm}^{FM} \propto \ln \tau_p^J$) in the SAF results the smaller slope than FM as well (blue dashed line).

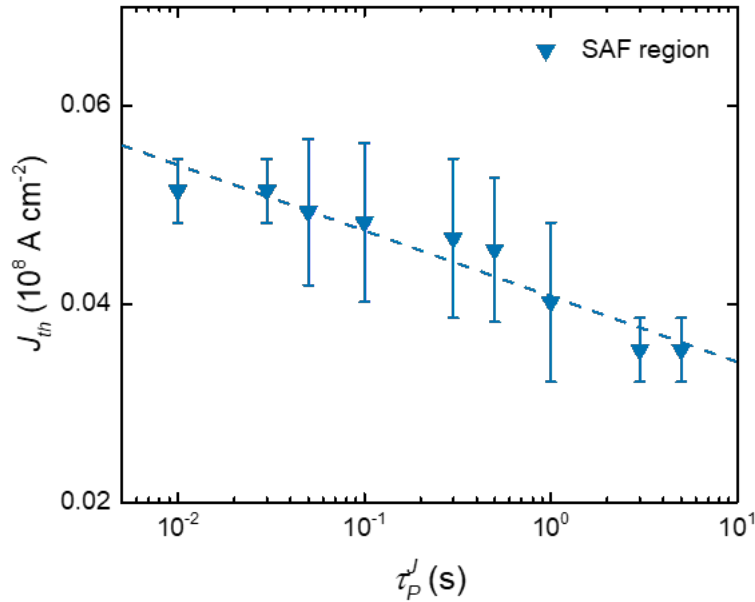


Figure 4.16. Pulse length dependence of the threshold current density for thermally assisted DW depinning in the SAF region. $J_{th,flow}^{FM}$ versus τ_p^J (10 ms to 5 s) of thermally assisted DW depinning in SAF region. The dashed line represents to fit and error bars correspond to the 25/75% probabilities.

4.4.3 SAF- FM junction

4.4.3.1 Domain wall injection in flow regime

After the demonstration of CIDWM in the FM and SAF regions at two different regimes, flow and thermally assisted regimes, we performed the DW motion across the SAF-FM lateral junction, which is formed to be perpendicular to the wire direction. In section 4.3.2, we assumed that the DW is positioned at the junction boundary after the field-induced initialization. In equilibrium, however, the DW does not preferred to be stabilized at the intermediate region, where the magnetic anisotropy energy is not clearly defined. The results shown in Fig 4.8, especially, imply that the transition region of the junction in between FM and SAF region seems to be very narrow, at least relevant to the width of DW itself. From now on, therefore, we consider that the DW is stabilized and positioned either at the FM or SAF region adjacent the junction boundary after initialization. Since DW motion across the junction needs to be investigated two ways depending upon its initial position, from FM to SAF region, and from SAF to FM region, hereafter, we use the term as the DW injection instead of motion in those cases.

Let us first determine the initial position of DW after the initialization. As discussed in previous sections, it is clear that DWs in the FM and SAF region move at different J_{th} in both flow ($J_{th,flow}^{FM} > J_{th,flow}^{SAF}$) and thermally assisted regime ($J_{th,therm}^{FM} < J_{th,therm}^{SAF}$). Thus, this can be simply determined depending on whether the DW moves with respect to corresponding applied current density. Fig. 4.17 shows Kerr microscope image of DW motion in four different cases with corresponding J_{th} , respectively. Note here that the DW motion was performed in flow regime ($\tau_p^J = 5$ ns) by applying series of short pulses as described in previous sections. When DW is initialized by field, it can freely move into the FM region (left-hand-side) with $J > J_{th,flow}^{FM}$. However, DW cannot move into SAF region under same condition ($J > J_{th,flow}^{FM}$) which is already larger than $J_{th,flow}^{SAF}$ as shown in second image of green shaded box (Fig. 4.17a). As we further increased J , DW can eventually be injected into SAF region (red shaded box in Fig. 4.17a). As a result, we recognize that the magnitude of DW injection from FM to SAF in flow regime $J_{th,flow}^{FM \rightarrow SAF}$ is much larger than both $J_{th,flow}^{FM}$, and $J_{th,flow}^{SAF}$. Surprisingly, on the other hand, $J_{th,flow}^{SAF \rightarrow FM}$ for the DW injection from SAF to FM appears to be similar to those of value in

the SAF region ($J_{th,flow}^{SAF \rightarrow FM} \cong J_{th,flow}^{SAF}$). Yellow shaded box in Fig. 4.17b shows DW injection from SAF to FM region. As soon as DW injected into both the FM and SAF region, DW motion continues by applying J above $J_{th,flow}^{FM}$, and $J_{th,flow}^{SAF}$, respectively (green and blue shaded box in Fig. 4.17). This asymmetric behavior is noteworthy and has an analogy to DW diode [123]. Therefore, we further focused on, in particular, the DW injection from FM to SAF region.

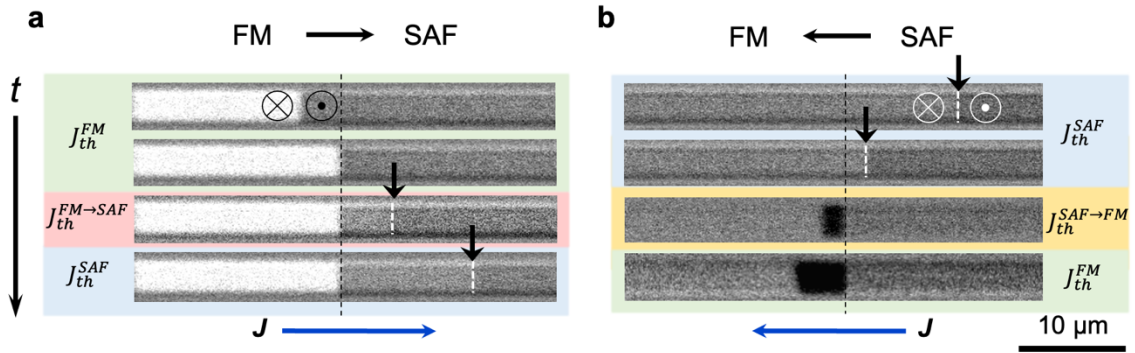


Figure 4.17. DW motion in the SAF-FM lateral junction. Kerr microscopy image of corresponding current-induced single DW motion from (a) FM to SAF region, and (b) SAF to FM region across the SAF-FM junction. DW motion is defined by four distinguished region, FM (green shaded), FM \rightarrow SAF (red shaded), SAF (blue shaded), and SAF \rightarrow FM (yellow shaded), respectively. DW moves with the applied current density J above J_{th}^i ($i = FM, SAF, FM \rightarrow SAF, or SAF \rightarrow FM$) depending upon the region. White and black Kerr contrast image correspond to down (\otimes or \downarrow) and up (\odot or \uparrow) DW configuration, respectively. Black dashed lines define the junction boundary and white dashed lines displays the DW in SAF region. Figure is adopted from [50].

Fig. 4.18 shows the DW injection probability $P_{inj}^{FM \rightarrow SAF}$, from FM to SAF region, as a function of applied J at various τ_p^J (5 to 100 ns) in flow regime. We performed each injection event right after the field-induced initialization process in the absence of external field. Measurements were repeated ten times for each condition to obtain the probability. Note that only single current pulse was applied for performing each injection measurement. Contrary to FM and SAF cases, the flow regime of DW is not determined by the velocity, but the success of injection in short pulse range. Here, we confirmed the success of the DW injection by rigorous method as presented in Appendix A2. We can see that the distribution of $P_{inj}^{FM \rightarrow SAF}$ is

broader at short τ_p^J , but it becomes narrower as τ_p^J increases, which is similar to the distribution of P_{dep}^{FM} in section 4.4.1.2. Overall, the injection occurs at higher J compared to the FM and SAF cases.

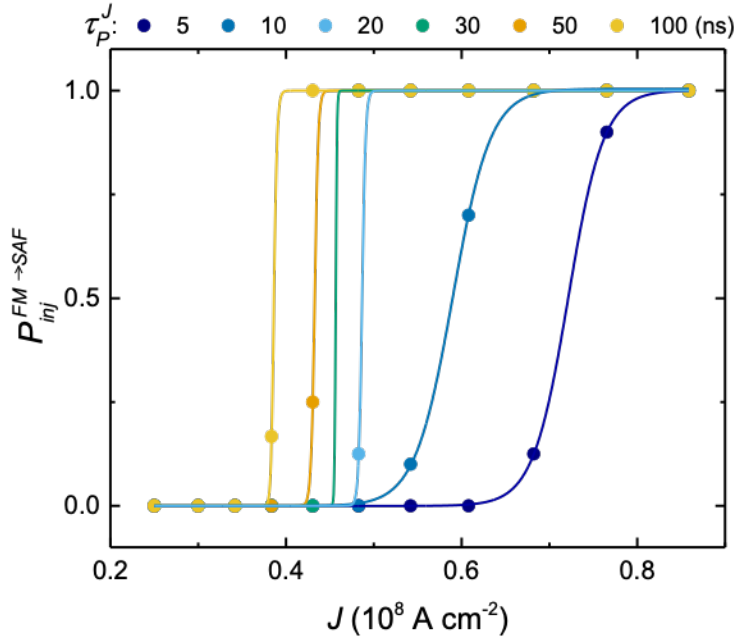


Figure 4.18. DW injection (FM \rightarrow SAF) probability versus applied current density in flow regime. Current-induced DW injection (FM \rightarrow SAF) probability $P_{inj,flow}^{FM \rightarrow SAF}$ as a function of current density in flow regime for various current pulse lengths τ_p^J (5, 10, 20, 30, 50, and 100 ns). Solid curves fit to standard error function profile. Figure is adopted from [50].

The threshold current density for DW injection from FM to SAF in flow regime $J_{th,flow}^{FM \rightarrow SAF}$ is obtained by taking the values of J corresponding to $P_{inj}^{FM \rightarrow SAF} = 0.5$ at each τ_p^J and those values are plotted in Fig. 4.19. As we expected, $J_{th,flow}^{FM \rightarrow SAF}$ monotonically reduces as τ_p^J increases which is the same as $J_{th,flow}^{FM}$ and $J_{th,flow}^{SAF}$. Moreover, we confirmed that $J_{th,flow}^{FM \rightarrow SAF}$ is larger than $J_{th,flow}^{FM}$ and $J_{th,flow}^{SAF}$ in all τ_p^J , thus resulting the relation $J_{th,flow}^{FM \rightarrow SAF} > J_{th,flow}^{FM} > J_{th,flow}^{SAF}$. Even at $\tau_p^J = 100$ ns, for instance, this relation does not change ($J_{th,flow}^{FM \rightarrow SAF} \sim 0.4 \times 10^8 \text{ A cm}^{-2} > J_{th,flow}^{FM} \sim 0.3 \times 10^8 \text{ A cm}^{-2} > J_{th,flow}^{SAF} \sim 0.2 \times 10^8 \text{ A cm}^{-2}$). By fitting the data, we obtained the intrinsic DW injection (FM \rightarrow SAF) threshold current density in flow regime

$J_{th_0,flow}^{FM \rightarrow SAF} \sim (0.41 \pm 0.01) \times 10^8 \text{ A cm}^{-2}$. The fitting curve represents the relation $J_{th,flow} - J_{th_0,flow} = \frac{1}{\tau_p^J}$ as same in previous sections.

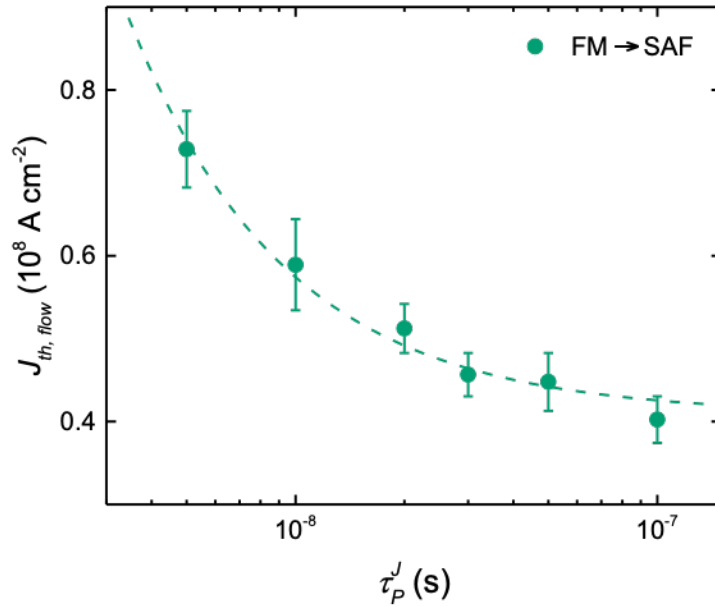


Figure 4.19. Pulse length dependence of the threshold current density for DW injection (FM → SAF) in flow regime. $J_{th,flow}^{FM \rightarrow SAF}$ versus τ_p^J (5, 10, 20, 30, 50, and 100 ns) of DW injection from FM to SAF region in flow regime. The dashed curve represents to fit and error bars correspond to the 25/75% probabilities.

4.4.3.2 Domain wall injection in thermally assisted regime

We further investigated the DW injection from FM to SAF region in thermally assisted regime by applying longer current pulse length ($\tau_p^J > 100$ ns). As similar to the FM and SAF cases, the DW injection occurs at relatively lower J compared to the flow regime, thereby proving thermal activation dominated mechanism. As with previous measurements, only single pulse was applied for each trial of DW injection.

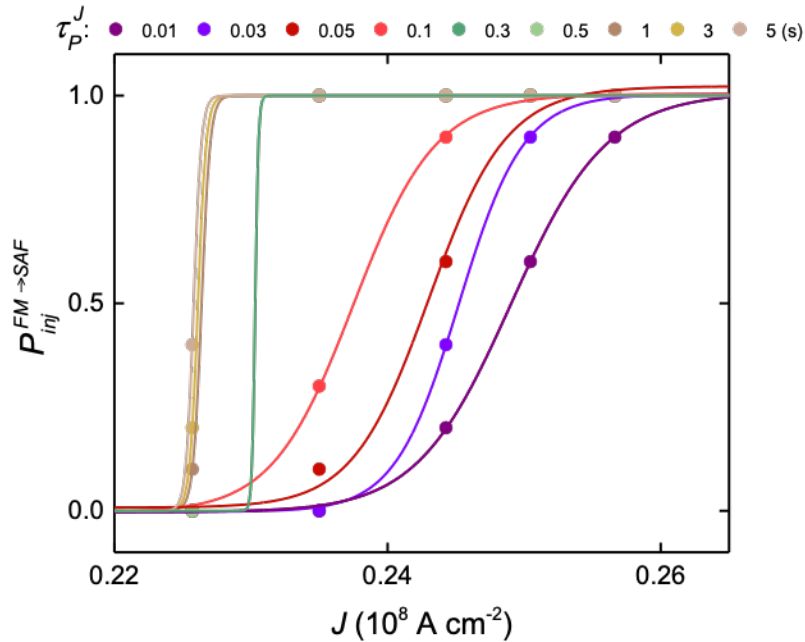


Figure 4.20. DW injection (FM \rightarrow SAF) probability versus applied current density in thermally assisted regime. Current-induced DW injection (FM \rightarrow SAF) probability $P_{inj,therm}^{FM \rightarrow SAF}$ as a function of current density in thermally assisted regime for various current pulse lengths τ_p^J (10 ms to 5 s). Solid curves fit to standard error function profile. Figure is adopted from [50].

By repeating each DW injection measurement for ten times, $P_{inj,therm}^{FM \rightarrow SAF}$ was obtained as a function of J at various τ_p^J (Fig. 4.20). The distributions of $P_{inj,therm}^{FM \rightarrow SAF}$ exhibit sharp profiles in a range of very long τ_p^J (≥ 1 s), and they are almost overlapped each other, while it becomes

wider in relatively short $\tau_p^J (< 0.5 \text{ s})$. This broad distribution of $P_{inj,therm}^{FM \rightarrow SAF}$ is more pronounced compared to the cases of FM and SAF discussed earlier.

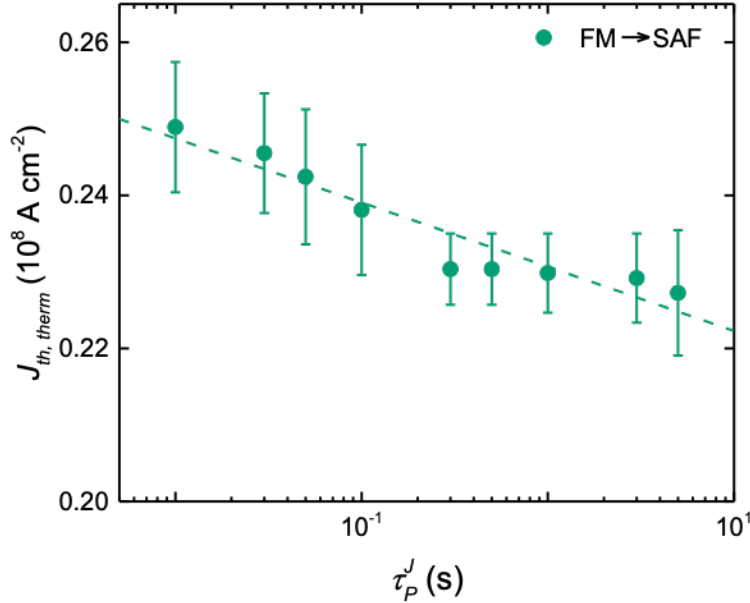


Figure 4.21. Pulse length dependence of the threshold current density for DW injection (FM \rightarrow SAF) in thermally assisted regime. $J_{th,therm}^{FM \rightarrow SAF}$ versus τ_p^J (10 ms to 5 s) of thermally assisted DW depinning in SAF region. The dashed line represents to fit and error bars correspond to the 25/75% probabilities.

Also, the threshold current densities of DW injection (FM \rightarrow SAF) in thermally assisted regime $J_{th,therm}^{FM \rightarrow SAF}$ show larger values, even an order of magnitude more than those of $J_{th,therm}^{FM}$ and $J_{th,therm}^{SAF}$ in all range of τ_p^J (Fig. 4.21). Based on these results, we found that the DW injection phenomenon needs to be understood in different mechanism in addition to conventional DW motion. Despite the increase of $J_{th,therm}^{FM \rightarrow SAF}$, the data fit to exponential relation ($J_{th,therm}^{FM \rightarrow SAF} \propto \ln \tau_p^J$), which indicates that the DW injection is clearly driven by the thermal activation energy (green dashed line).

4.4.3.3 Junction angle dependent domain wall injection

As introduced in section 4.3, the fabrication of SAF-FM junction highly relies on the lithography technique. This gives us a degree of freedom in designing the shape of junctions. Nevertheless, in previous sections 4.4.3.1 and 4.4.3.2, we only discussed the case of DW injection from FM to SAF region through the junction which is perpendicularly formed to the wire length. Thus, in this section, we show the results obtained from the current-induced DW injection from FM to SAF region through various shapes of junctions. We fabricated the junction with tilting angle with respect to the wire length (direction of DW motion), and the tilting angle of junction is defined to θ_J which is 0° at the perpendicular to the wire length. The θ_J varies from 0 to 60° with each 15° steps as shown in Fig. 4.22.

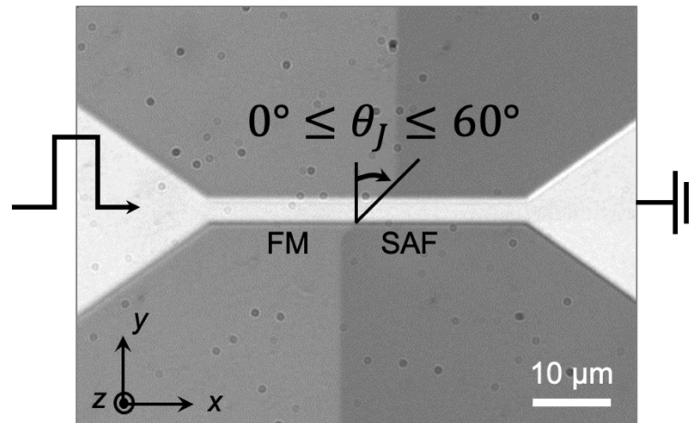


Figure 4.22. SAF-FM lateral junction with junction tilting angle. Optical microscopy image of representative SAF-FM junction formed in racetrack nanowire device. The junction tilting angle θ_J is defined as the angle with respect to the perpendicular to the wire length. Here, the $\theta_J = 60^\circ$.

The DW initialization process is identical to the case for $\theta_J = 0^\circ$ as introduced in section 4.3.2, and was prepared before each current-induced injection measurement. The shape of initialized DW was formed by following the shape of the junction boundary in the presence

of external field (Fig. 4.23b). As soon as the field disappears, however, the DW was restabilized by moving spontaneously backwards from the boundary of junction to minimize the DW energy (Fig.4.23c). Despite the deformation, the DW was still in contact with part of boundary of the junction.

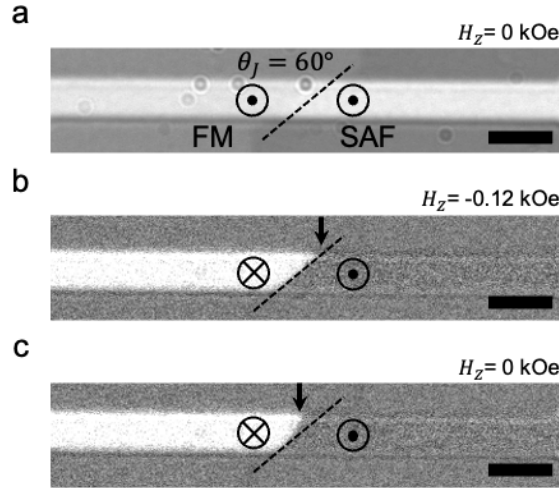


Figure 4.23. Field-induced domain wall initialization at tilted junction. Kerr microscopy images of DW initialization procedure at representative SAF-FM junction with $\theta_j = 60^\circ$. (a) Single domain is initially formed in both FM and SAF side at zero-field (no DW). (b) DW is initialized in the presence of external field along easy-axis ($H_z = -0.12$ kOe) by following the shape of junction, but (c) is restabilized in the absence of field by moving away from junction. Note that the dashed lines display the junction boundary and black arrows correspond to DW position, respectively. Scale bars represent $5 \mu\text{m}$.

After initialization, we performed DW injection at $\theta_j = 15, 30, 45,$ and 60° and compared their injection threshold current densities $J_{th}^{FM \rightarrow SAF}$ with those of value obtained from $\theta_j = 0^\circ$, respectively. Note that the injection measurement was demonstrated in the absence of magnetic field. In addition, we determined the success of DW injection as soon as the portion of DW is injected into SAF region. By measuring the DW injection probability $P_{inj}^{FM \rightarrow SAF}$ in short ($\tau_p^J \leq 100$ ns) and long pulse regime ($\tau_p^J > 100$ ns), we obtained the $J_{th}^{FM \rightarrow SAF}$ as a function of τ_p^J at various θ_j in flow and thermally assisted regime, respectively. Fig. 4.24 shows the θ_j dependence of $J_{th,flow}^{FM \rightarrow SAF}$ in flow regime. At short pulse regime, interestingly, $J_{th,flow}^{FM \rightarrow SAF}$ depends sensitively on θ_j , overall decreasing with increasing θ_j for $\theta_j > 30^\circ$.

$J_{th,flow}^{FM \rightarrow SAF}$ is nearly constant for $\theta_j \leq 30^\circ$. As a result, $J_{th,flow}^{FM \rightarrow SAF}$ reduces approximately 50% as θ_j increases from 0 to 60° . All fitting curves agree with the data by following the relation $J_{th,flow} - J_{th_0,flow} = \frac{1}{\tau_p^J}$ as discussed in previous sections as well (dashed curves).

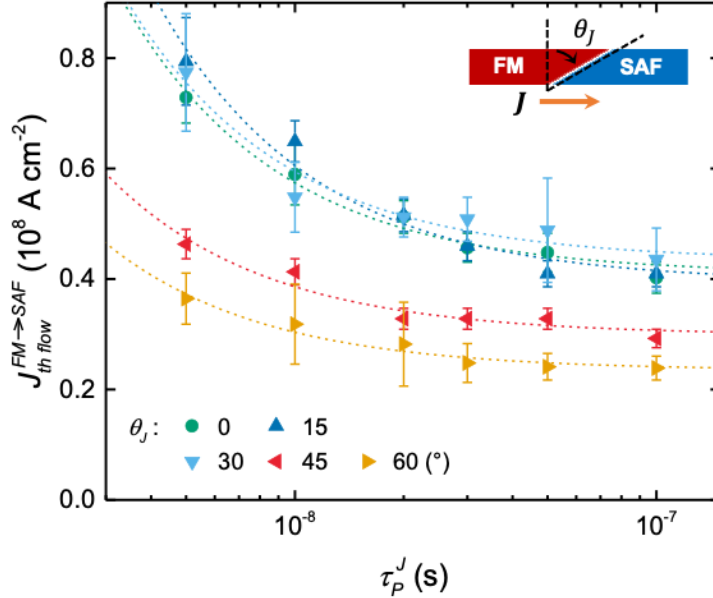


Figure 4.24. Junction angle dependence of pulse length versus the threshold current density for DW injection (FM \rightarrow SAF) in flow regime. $J_{th,flow}^{FM \rightarrow SAF}$ versus τ_p^J (5 to 100 ns) of DW injection (FM \rightarrow SAF) in flow regime at various $\theta_j = 0^\circ$ (green circle), 15° (dark blue triangle), 30° (light blue triangle), 45° (red triangle) and 60° (yellow triangle). The dashed curves represent to fit and error bars correspond to the 25/75% probabilities, respectively.

Similar trends can also be seen in a thermally assisted regime, that $J_{th,therm}^{FM \rightarrow SAF}$ overall reduces at large θ_j (see Fig. 4.25). At $\theta_j = 60^\circ$ (yellow triangle), consequently, $J_{th,therm}^{FM \rightarrow SAF}$ further decreased thereby resulting $J_{th,therm}^{FM \rightarrow SAF} \sim 0.03 \times 10^8 \text{ A cm}^{-2}$, which is comparable to those of values of $J_{th,therm}^{SAF}$. On the other hand, the $J_{th}^{FM \rightarrow SAF}$ exhibits almost no significant change until $\theta_j = 30^\circ$, and even increases slightly compared to $\theta_j = 0^\circ$. It is very noteworthy that this significant decrease of $J_{th}^{FM \rightarrow SAF}$ in both flow and thermally assisted regime occurs simply by changing the shape of junction. This means that the DW can move into SAF from FM region as if there were no junction boundary. In addition, all data nicely fit to exponential relation ($J_{th,therm}^{FM \rightarrow SAF} \propto \ln \tau_p^J$) thus well supporting thermal activation mechanism.

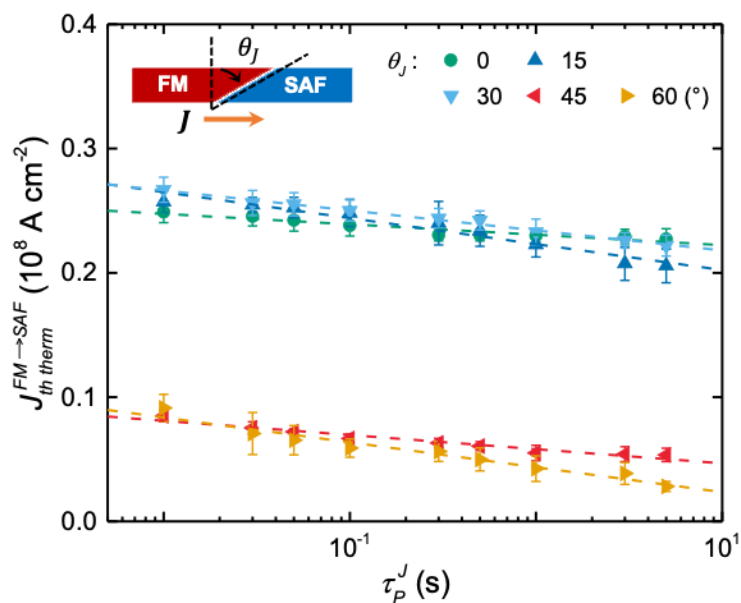


Figure 4.25. Junction angle dependence of pulse length versus the threshold current density for DW injection (FM \rightarrow SAF) in thermally assisted regime. $J_{th,flow}^{FM \rightarrow SAF}$ versus τ_p^J (10 ms to 5 s) of DW injection (FM \rightarrow SAF) in flow regime at various $\theta_J = 0^\circ$ (green circle), 15° (dark blue triangle), 30° (light blue triangle), 45° (red triangle) and 60° (yellow triangle). The dashed lines represent to fit and error bars correspond to the 25/75% probabilities, respectively.

4.5 Field-induced domain wall motion in SAF-FM lateral junctions

The DW motion can also be driven by external magnetic fields which align to an easy-axis component of magnet. Compared to the CIDWM, which is driven by the spin polarized current generated from adjacent heavy metal, field-induced DW motion (FIDWM) is mostly governed by the Zeeman energy that enables DW to overcome pinning energy barrier. Since the field is globally applied to the system rather than locally to the DW, an entire energy landscape is changed with respect to DW configuration. In this section, we performed the FIDWM by applying single pulse of magnetic field with a pulse duration τ_p^H in each three regions, including FM, SAF, and SAF-FM junction interface, respectively. The DW depinning and injection probabilities P_{dep}^i ($i = FM, SAF$ and $FM \rightarrow SAF$) was obtained by repeating measurements of ten times in each condition. Then, the threshold field for the DW depinning, namely the depinning field H_{th}^i ($i = FM, SAF$ and $FM \rightarrow SAF$) at each region is discussed as a function of pulse duration τ_p^H . Note that the FIDWM was only performed in the long pulse regime ($\tau_p^H > 100$ ns), which correspond to the thermally assisted regime, due to the limit of apparatus.

4.5.1 Ferromagnet region

4.5.1.1 Domain wall depinning in thermally assisted regime

As discussed in section 4.1.1.1, a magnetization reversal generally occurs in FM when the magnitude of applied field is above the coercivity $H_c^{FM} \sim 0.1$ kOe. In the absence of DW, the switching process simultaneously occurs entire area which is shown to sharp transition in hysteresis loop (see Fig. 4.1a). However, the reversal process can also occur at relatively lower magnitude of field than H_c^{FM} in the presence of DW. Since the DW propagation mostly requires

less energy than switching itself, this gives rise to a gradual change of magnetization at lower field instead of sharp transition. We performed all the FIDWM in the presence of DW after the initialization by applying field H_z so that it is expected to be moved at lower magnitude of field as well.

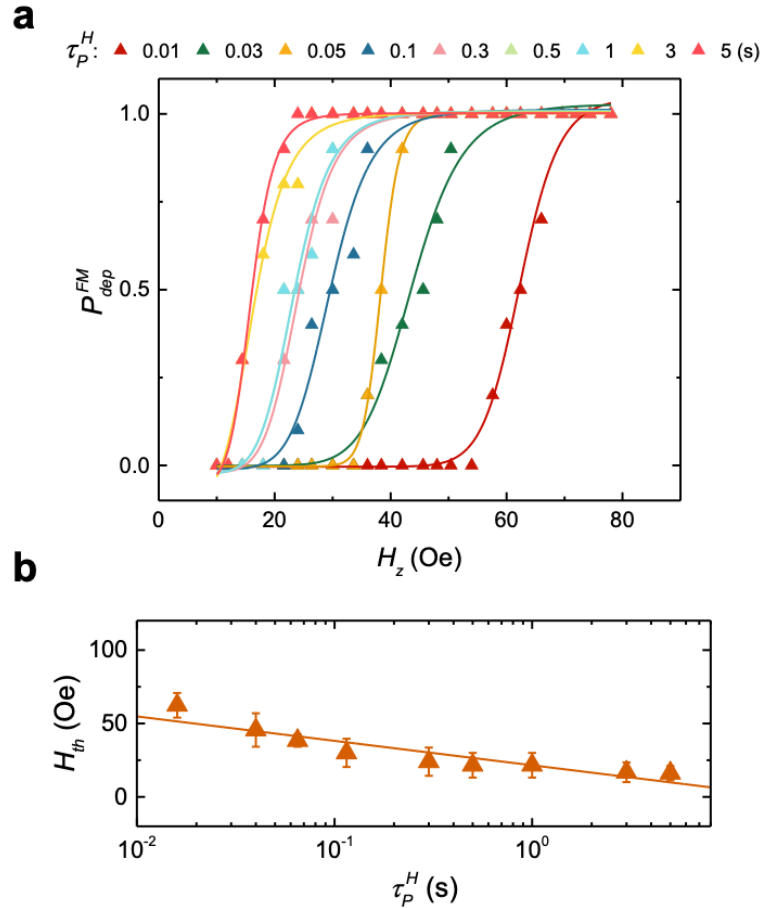


Figure 4.26. Field-induced DW depinning in the FM region. (a) DW depinning probability P_{dep}^{FM} versus applied current density in the FM region at various field pulse duration τ_p^H (16 ms to 5 s). **(b)** Threshold depinning field H_{th}^{FM} as a function of τ_p^H . Solid curves and line fit to standard error function and exponential relation, respectively. Error bars correspond to the 25/75% probabilities. Figure is adopted from [50].

Similar to the current induced depinning case, the DW depinning measurement was demonstrated by applying a single field pulse with a various length τ_p^H from 16 ms to 5 s. Here, we found that there is a discrepancy between the input and output of τ_p^H due to the inductance of coil magnet used for the experiment. In particular, this is remarkable at short pulse regime below $\tau_p^H \sim 100$ ms. For example, the input electrical pulse with a length of 10 ms results the

actual field pulse $\tau_P^H \sim 16$ ms, including rising and falling time. Therefore, we verified the effective field pulse lengths corresponding to the input pulses by oscilloscope prior to measurements (see Appendix A.3). Afterwards, the DW depinning probability P_{dep}^{FM} was obtained as a function of the magnitude of magnetic field H_z as shown in Fig. 4.26a. As we expected, the DW started depinning at significantly lower magnitude of field compared to H_c^{FM} , for instance, moving by pulse $H_z \sim 80$ Oe with $\tau_P^H \sim 16$ ms. Moreover, the depinning even occurred at much lower H_z (~ 20 Oe) with longer $\tau_P^H \sim 5$ s.

Based on the P_{dep}^{FM} measurement, we derived the threshold DW depinning field H_{th}^{FM} as a function of τ_P^H as shown in Fig. 4.26b. The H_{th}^{FM} is defined by those of value corresponding to $P_{dep}^{FM} = 0.5$ at each τ_P^H . It is clearly confirmed that the H_{th}^{FM} for the DW depinning was gradually lowered through the quantitative results as well as previous estimation. Furthermore, the exponential linear fitting greatly agrees with the H_{th}^{FM} as a function of τ_P^H , thus proving the thermal activation driven depinning in this measurement.

4.5.2 Synthetic antiferromagnet region

4.5.2.1 Domain wall depinning in thermally assisted regime

Let us continue the DW depinning measurement in SAF region. In general, the FIDWM is hardly possible in perfectly compensated ideal AF system since the net moment is zero. However, we were able to perform FIDWM in our SAF system due to the tiny uncompensated moment which leads to non-zero remanent ($m_R^{SAF} \sim 1$ μ emu) at AF state. This is one of the biggest advantages of multilayer based SAF structure that one can easily tailor the degree of compensation. In order to perform the FIDWM in SAF, we injected single DW into SAF region by current pulse as presented in previous sections. The DW in SAF is initialized by up-down configuration along the easy-axis as same as the case for the FM.

Fig. 4.27 shows the field-induced DW depinning probabilities in SAF P_{dep}^{SAF} as a function of the magnitude of magnetic field H_z at various τ_P^H , and the corresponding threshold depinning field H_{th}^{SAF} as well. Compared to the FM, the magnitude of DW depinning fields in

SAF are overall significantly larger than those of values at same τ_p^H , and even larger than H_c^{FM} . At $\tau_p^H = 16$ ms, the depinning requires $H_z > 750$ Oe, which is almost one order of magnitude larger than FM case. But it is still smaller than H_{sf}^{SAF} . At SAF-FM lateral junction, in this case, we assume that the switching of FM region occurs while the DW in SAF does not move at all when the field is applied to opposite direction. This again emphasize the robustness of SAF against the external field. In addition, the depinning threshold field H_{th}^{SAF} is plotted as a function of τ_p^H in Fig. 4.27b. Even at $\tau_p^H = 5$ s, which is longest duration, H_{th}^{SAF} is larger than both H_{th}^{FM} and H_c^{FM} . By fitting the exponential linear relation (blue solid line), we can estimate that the DW depinning can eventually occurs in SAF region under the field with magnitude of H_c^{FM} (~ 100 Oe) at $\tau_p^H > 100$ s.

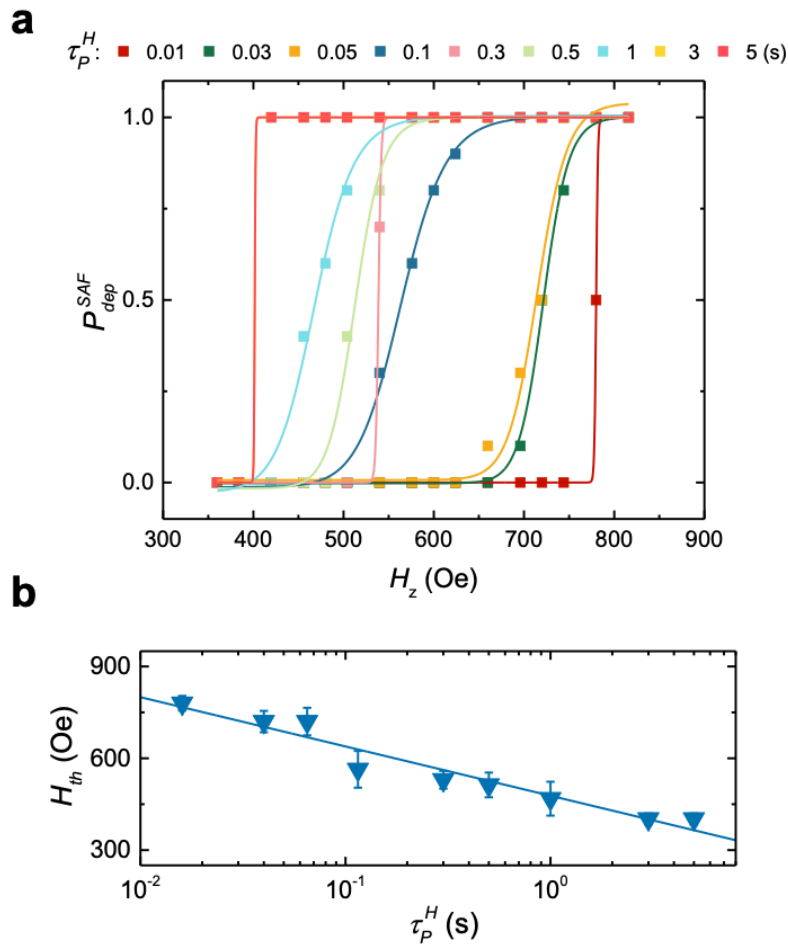


Figure 4.27. Field-induced DW depinning in the SAF region. (a) DW depinning probability P_{dep}^{SAF} versus applied current density in the SAF region at various field pulse duration τ_p^H (16 ms to 5 s). **(b)** Threshold depinning field H_{th}^{SAF} as a function of τ_p^H . Solid curves and line fit to

standard error function and exponential relation, respectively. Error bars correspond to the 25/75% probabilities. Figure is adopted from [50]

During the field-induced depinning measurement in SAF, very interestingly, we observed that the direction of DW motion in the FM and SAF region is opposite to each other under the same orientation of external field as shown in Fig. 4.28. In the FM region, for instance, the external field was applied to $+H_z$ direction, thus the DW with up-down configuration moves to the right-hand side (see Fig. 4.28a). On the other hand, the same DW (up-down) moves to the left-hand side (see Fig. 4.28b).

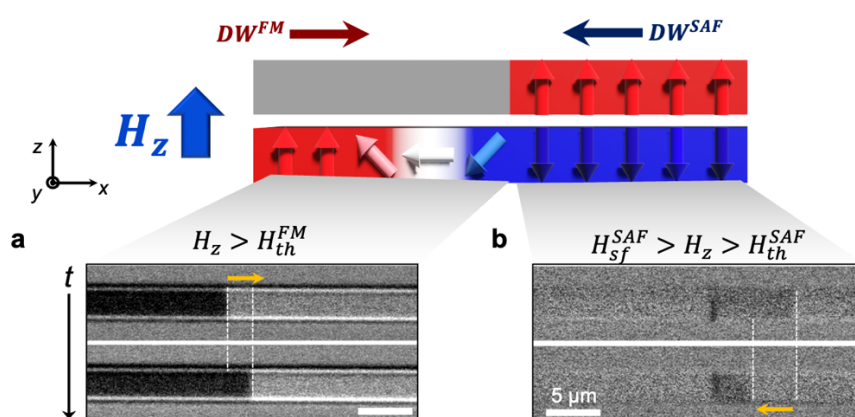


Figure 4.28. Comparison of field-induced DW motion in the FM and SAF region. Differential Kerr microscopy images of field-induced DW depinning in (a) the FM and (b) SAF region. DW is initialized to up-down (black-white, $\uparrow\downarrow$) configuration in both regions. The direction of DW motion is opposite in the FM (towards right) and SAF (towards left) in the presence of $+H_z$. Figure is adopted from [50].

4.5.3 SAF-FM junction

4.5.3.1 Domain wall injection in thermally assisted regime

As we discussed in section 4.5.2, the motion of DW to the external field is opposite to each other in FM and SAF with respect to same DW configuration. This interesting finding leads us to question how the DW behaves at the SAF-FM junction boundary. In case of CIDWM, we observed the asymmetric DW injection across the junction boundary which results to significantly high injection threshold current density when the DW moves from FM to SAF region ($J_{th}^{FM \rightarrow SAF}$) ($J_{th}^{SAF \rightarrow FM}$). Furthermore, the degree of asymmetry of J_{th}^i ($FM \rightarrow SAF$ and $SAF \rightarrow FM$) is reduced by designing the angle of the junction thereby resulting those of values nearly the same in both directions at large θ_j .

To compare the field-induced DW injection with current-induced injection case, we first positioned the DW in the FM region with up-down DW configuration. Here, the $\theta_j = 0^\circ$. Then, the external field was applied to $+H_z$ ($> H_{th}^{FM}$) in order to move DW towards the junction boundary (see Fig. 4.28a). Surprisingly, the DW did not move further into SAF region, even as the applied field continues to increase up to 3 kOe, which is close to H_{sf}^{SAF} . We also further extended τ_p^H up to two hours (7200 s) that is already beyond the ‘‘pulse’’ range. However, the DW was still not able to be injected into SAF region under $+H_z = 3$ kOe with $\tau_p^H = 7200$ s, thus resulting the field-induced injection probability $P_{inj}^{FM \rightarrow SAF} = 0$. Even more remarkable is that this phenomenon is independent of the shape of the junction so that the none of DWs at all of junctions ($0^\circ \leq \theta_j \leq 60^\circ$) could not inject to the SAF region, but stayed at the junction boundary (see Fig. 4.29). On the other hand, the DW could inject from SAF to FM region across the junction when the H_z is larger than the threshold ($> H_{th}^{SAF}$), but did not continue to move further inside FM region. Consequently, the DW was ‘‘trapped’’ at the junction boundary in the presence of external field.

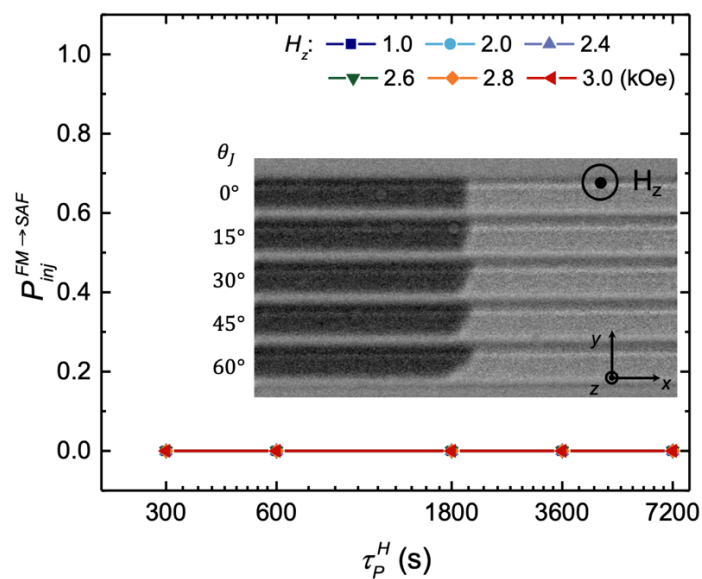


Figure 4.29. Field-induced DW injection (FM → SAF) probability versus τ_p^H at various junctions. Field-induced DW injection (FM → SAF) probability $P_{inj}^{FM \rightarrow SAF}$ as a function of τ_p^H (300 to 7200 s). The magnitude of external field H_z corresponds to 1.0 kOe (blue square), 2.0 kOe (light blue circle), 2.4 kOe (violet triangle), 2.6 kOe (green triangle), 2.8 kOe (orange diamond), and 3 kOe (red triangle), respectively. Inset depicts the representative Kerr microscopy image of field-induced DW injection from FM to SAF at multiple junctions with θ_j ($0^\circ \leq \theta_j \leq 60^\circ$) in the presence of $+H_z = 3$ kOe. Here note that the DW configuration is up-down ($\odot|\otimes$, black-white) for all cases. Figure is adopted from [50].

Chapter 5 Discussions

In this chapter, we will discuss forementioned unconventional phenomena in more depth. First, we investigate the oxidation states of multilayers in SAF which give rise to SAF to FM transition by measuring depth-profiling x-ray photoemission spectroscopy (XPS) in section 5.1. In addition, the structural analysis of junction will be discussed based on the measurement of atomic force microscopy (AFM) and cross-section transmission electron microscopy (TEM) as well (section 5.2). In section 5.3, afterwards, we evaluate the energy barriers for the DW motion in FM, and SAF region based on current- and field-induced motion performed in section 4.4 and 4.5. Taking the energy barriers into account, we discuss the origin of asymmetric current-induced DW injection and field-induced DW pinning at SAF-FM junction (section 5.4). The reduction of threshold current density for DW injection in tilted junction will be also discussed together. In order to reveal the correlation between energy barriers and thermal stability of DW, furthermore, the temperature dependent energy barriers are evaluated and compared in each FM, SAF, and SAF-FM junction, respectively, in section 5.5. At last, the discussion concludes with presenting the potential application of SAF-FM junctions such as multi DWs injection and high stability of SAF-FM-SAF bi-junctions (section 5.6).

5.1 Oxidation state of upper magnetic layer of synthetic antiferromagnet multilayers

As shown in section 4.1, the magnetic properties of SAF can be clearly transformed to single FM by oxygen plasma process. Remarkably, the SAF to FM transition gradually proceeded as a function of oxidation process time, and then eventually became saturated even at longer process time (see Fig. 4.3). To understand the underlying mechanism, we conducted X-ray photoemission spectroscopy (XPS) depth-profile measurement to analyze the oxidation

state of each layer. The degree of oxidation through the UM of SAF is further investigated in comparison with pristine SAF structure as well.

5.1.1 X-ray photoemission spectroscopy depth-profile analysis

According to the magnetic hysteresis loop shown in Fig. 4.4, it appears as if the only lower magnetic layer of SAF contributes to the entire magnetic properties of system. In particular, the comparison of $M_s t$ and H_k between pristine and oxidized SAF clearly supports this quantitatively. To confirm the suppression of upper magnetic layer of SAF, XPS depth profile measurements were carried out, using Ar ion etching, on the unpatterned pristine SAF film and FM film that had been obtained by oxidization for 60 sec of a SAF film (see Fig. 4.4). Note that the etching proceeded from top to bottom layer so that TaN capping layer was initially etched away. The etching conditions are following: Ar⁺ energy 500 eV, 0.5 μ A beam current, 5 x 2 mm² etching area, 20 sec per cycle. XPS spectra were measured after each cycle of etching process.

During the measurement, as shown in Fig. 5.1, we found that it takes longer to etch the TaN capping layer for the oxidized SAF than for the pristine case, thus assuming that either TaN becomes thicker on oxidation by forming tantalum oxynitride (TaO_xN_y) or the etching rate of TaO_xN_y is slower. The depth profiles show that the atomic ratio of oxygen (green solid line) is significantly increased in the TaN, and the Co and Ni upper layers in the oxidized SAF film. Since the penetration depth of X-ray is considered to be at least few nano meters, the intensity of signals is averaged from entire stack including lower magnetic layer.

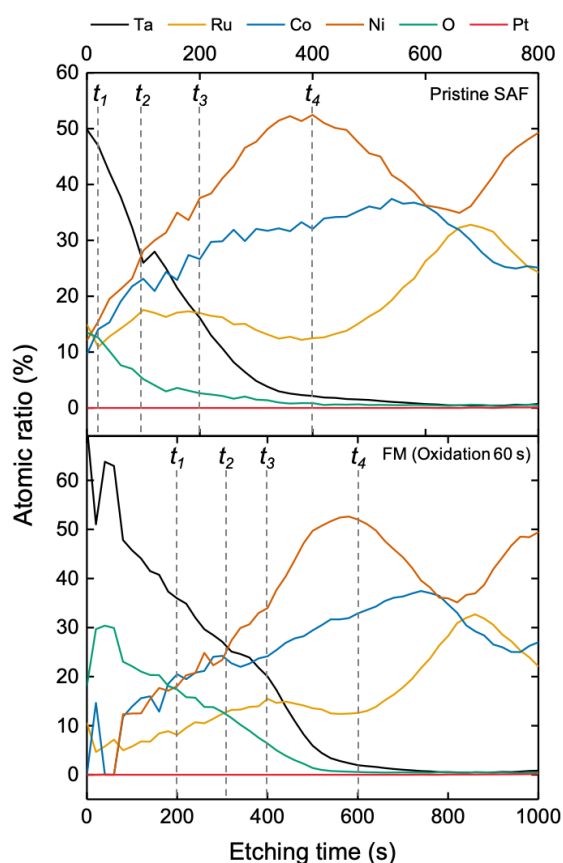


Figure 5.1. XPS profile of atomic concentrations of elements with etching time. Depth profile spectra of pristine (upper panel) and oxidized SAF (lower panel). The four points t_1 , t_2 , t_3 , and t_4 that are shown in the figure refer to the points where the Co and Ni 2p spectra are investigated, as shown in Fig. 5.2. Figure is adopted from [50]

We further investigate the oxidation state of magnetic elements, Co and Ni, by comparing the binding energy shift between pristine and oxidized SAF at four different measurement points. First two measurement points are determined by the point where the intensities of atomic ratio of Co, and Ni are equivalent to oxygen (t_1), and tantalum (t_2), respectively. At this step, the spectra are mostly collected from the upper layer. We also measured the spectra at two points in the middle of upper layer (t_3), and the peak of the Ni intensity (t_4).

As shown in Fig. 5.2, metallic Co 2p_{3/2} (~778.2 eV) and Ni 2p_{3/2} (~852.6 eV) spectra are observed in the pristine SAF (solid line) film, thus showing that the 30 Å TaN capping layer effectively protects Co and Ni in the upper layer against natural oxidation. On the other hand, the oxidized SAF (dashed line) shows chemical shifts of ~ 0.5 eV of spectral peaks towards

higher binding energies. Although the identification of precise oxidation states of Co and Ni is limited at this stage, we clearly confirm that the oxidation of Co and Ni in the upper layer. Since the atomically thin CoO_x and NiO_x layers are considered to be magnetically dead layers, this concludes that there is no contribution as UM of SAF. Interestingly, as the film is further etched away, thus allowing analysis of the lower FM layer, Co and Ni are clearly seen to be metallic (unoxidized) (t_4). In this regard, we find that the Ru spacer layer acts as a passivation layer that protects the lower FM layer against oxidation even after extended oxidation times [124].

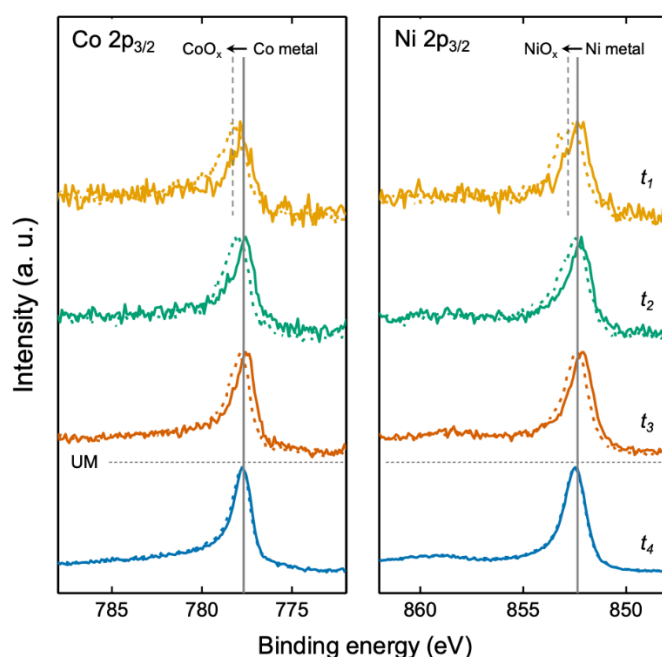


Figure 5.2. XPS spectra of Co and Ni at different etching times. $2p_{3/2}$ spectra of Co (left panel) and Ni (right panel) in pristine SAF (solid line) and oxidized SAF (dashed line) are plotted at t_1 , t_2 , t_3 and t_4 as designated in Fig. S3. Peak positions for metallic Co and Ni are indicated, as a guide, by grey solid lines, while those from the oxidized film are displayed by grey dashed lines. Figure is adopted from [50]

5.2 Transition region in SAF-FM lateral junctions

5.2.1 Vertical and lateral structure formation

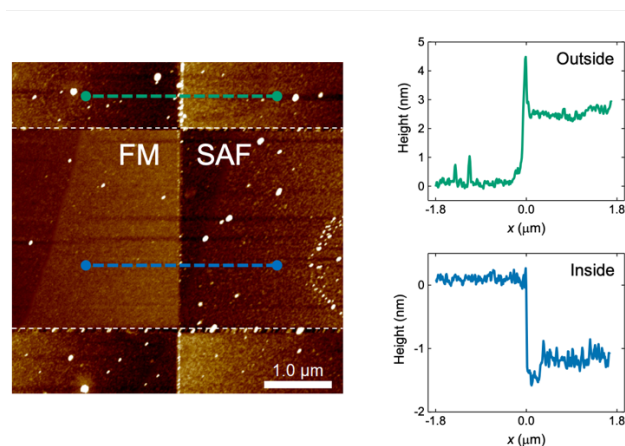


Figure 5.3. Atomic force microscopy (AFM) images of SAF-FM junction ($\theta_J = 0^\circ$) in a racetrack. The edges of the racetrack wire are defined by the white dashed lines. The SAF-FM junction boundary is clearly seen from the color contrast within the nanowire. Step heights are measured on the racetrack across the junction (blue dashed line) and off the racetrack that is encapsulated with alumina (green dashed line). Figure is adopted from [50]

As discussed in section 5.1, the oxidation on TaN capping layer results in TaO_xN_y which may increase the thickness due to the oxygen intercalation. In order to prove that, the thickness could be directly measured by atomic force microscopy (AFM) at the boundary of SAF-FM junction. Here, the width of racetrack wire is 3 μm. AFM imaging shows that the oxidation process results in a local increase in the thickness of the racetrack by ~1-2 nm as shown in Fig. 5.3 (blue solid line), which allows us to readily confirm the formation of junction boundary after fabrication. On the other hand, the alumina encapsulation region outside the racetrack nanowire is found to become thinner due to chemical etching of the alumina by the developer for lithography process, which is diluted tetramethylammonium hydroxide (TMAH) (green solid line in Fig. 5.3). The etching rate of alumina is estimated to be ~ 5 nm/min at room temperature. This leads to the distinct color contrast in the optical microscopy image, as can be seen in Fig. 4.7 and 4.22.

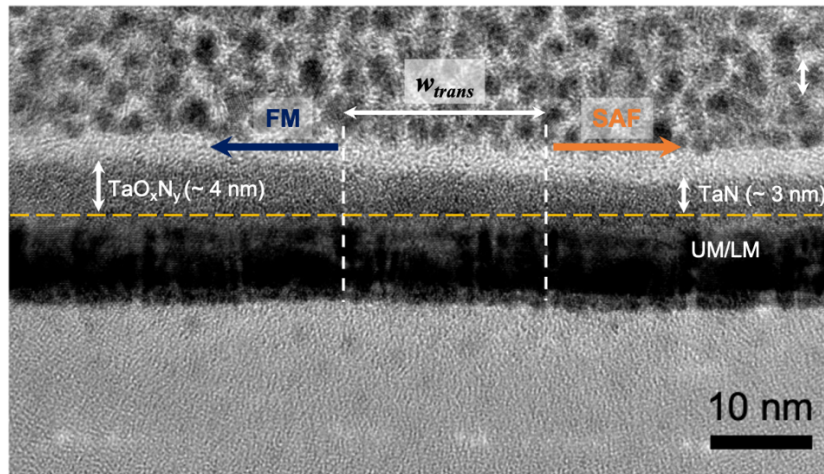


Figure 5.4. Cross-sectional transmission electron microscopy (TEM) image of SAF-FM junction. The FM (left-hand side) and SAF (right-hand side) region can be clearly distinguished by the height difference between TaO_xN_y (~ 4 nm) and TaN (~ 3 nm), respectively. The SAF-FM junction boundary is determined by including the transition region width of $w_{trans} \sim 20$ nm. White dashed lines define the transition region, and yellow line guides the interface between capping layer and UM of SAF.

Although the sharp step is observed in Fig. 5.3, the transverse transition region across the junction could not be clearly defined due to the limit of lateral resolution in AFM measurement. Since the lateral diffusion and scattering of oxygen inside the layer is inevitable during the process, the transition region, which is the intermediate state of SAF and FM, is expected to be formed at the boundary of junction. To verify this, cross-sectional transmission electron microscopy (TEM) was performed across the junction ($\theta_j = 0^\circ$). Note that the TEM lamella was prepared by focused ion beam (FIB) with Ga^+ ion source. Fig. 5.4 clearly shows the FM (blue, left-hand side) and SAF (orange, right-hand side) region that can be distinguished by thick TaO_xN_y (~ 4 nm) and thin TaN (~ 3 nm) capping layer, respectively. The transition region is broadly formed between FM and SAF region with a width of $w_{trans} \sim 20$ nm (white arrows). The definite magnetic state of transition region cannot be firmly established at this stage. However, we can assume that the gradient of uncompensated SAF is continuously formed by following the thickness variation based on the discussion in section 4.2. Furthermore, the w_{trans} is comparable to the width of typical Néel type DW (tens of nano meters), thus allowing the DW motion across the junction without annihilation as observed in section 4.4.

5.3 Determination of energy barriers for the domain wall motion

In section 4.4, we showed that the DW motion is induced by applying electrical currents or magnetic fields. To initiate the DW motion, namely depinning, either the minimum magnitude of current or field is required, that is called threshold current density J_{th} or field H_{th} , respectively. We further investigated the J_{th} in two different regimes, flow and thermally assisted, by varying the applied pulse length. In principle, the $J_{th,flow}$ in flow regime exhibit larger than those of values in thermally assisted regime, since the $J_{th,flow}$ relies on the torque efficiencies, which are the spin-orbit torque, and exchange coupling torque. But, the origin of $J_{th,flow}$ still remains elusive. In thermally activated regime, on the other hand, the $J_{th,therm}$ is strongly correlated to the thermal activation energy, thereby depinning the DW over the thermal energy barrier. This is also the same for the field-induced DW motion. Although the underlying mechanism for DW motion is different from current-induced case, the thermal activation energy gives rise to DW depinning as an applied field is above $H_{th,therm}$ in thermally assisted regime as well. In this section, thus, we will discuss how to determine the energy barriers for the DW motion by taking into account the $J_{th,therm}$ and $H_{th,therm}$ in three different regions, FM, SAF, and FM \rightarrow SAF ($\theta_j = 0^\circ$), respectively.

5.3.1 Energy barriers derived from current-induced domain wall motion

To investigate the energy barriers for DW depinning and injection, we carried out the current-induced DW depinning measurements in the thermally activated regime and determine the corresponding $J_{th,therm}^i$ ($i = \text{FM or SAF}$), and $J_{inj,therm}^{FM\rightarrow SAF}$ as discussed in section 4.4. Of particular interests are the findings of the inversion of J_{th}^{FM} and J_{th}^{SAF} in between flow and thermally assisted regime, and significantly larger $J_{inj}^{FM\rightarrow SAF}$ compared to both FM and SAF regardless of regimes. Fig. 5.5 depicts the summary of J_{th}^i ($i = \text{FM, SAF, or FM}\rightarrow\text{SAF}$) as a

function of pulse length including flow and thermally activated regime. Here note that the $\theta_j = 0^\circ$ in this case.

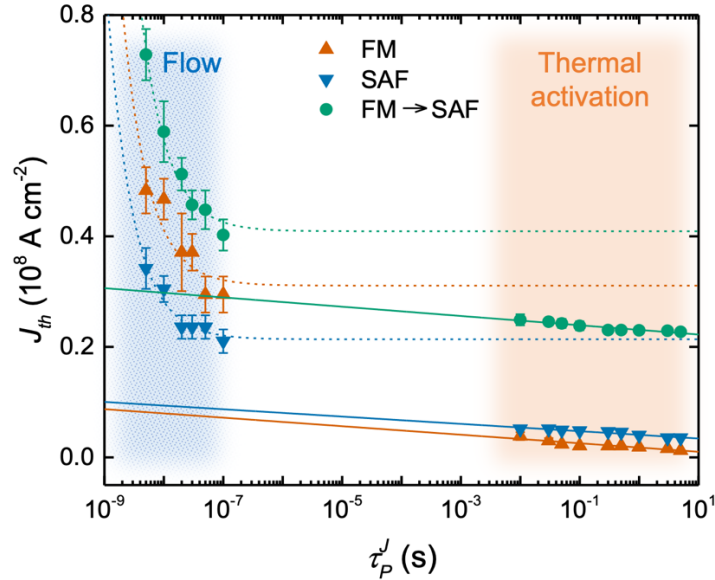


Figure 5.5. Threshold current density as a function of pulse length in FM, SAF, and FM→SAF ($\theta_j = 0^\circ$) regions. The flow and thermally activated regimes of CIDWM are highlighted by blue and orange shaded backgrounds, respectively. The dashed and solid curves correspond to fits to the relation $J_{th,flow}^i - J_{th0,flow}^i \propto 1/\tau_P^J$ ($i = FM, SAF, \text{ or } FM \rightarrow SAF$) and $J_{th,therm}^i \propto 1 - (1/E_j^i) \ln(\tau_P^J/\tau_0)$, in the flow and thermally activated regime, respectively. Note that the $\theta_j = 0^\circ$ in this case. The error bars in the flow, and thermally activated regimes correspond to the standard deviation, and 25/75% probabilities, respectively. Figure is adopted from [50]

Prior to the discussion of the thermally activated regime, we first need to clarify the DW motion and corresponding $J_{th,flow}^i$ ($i = FM, FM \rightarrow SAF, \text{ or } SAF$) in flow regime. In case of the magnetization switching, driven by either STT or SOT, the intrinsic switching is only possible in very short time scale, typically in nano or even sub-nano seconds, due to strong dependence on the efficiency of angular momentum transfer from current to the magnet. In this regime, thus, the stochastic thermal fluctuation does not play a key role in switching. This feature typically appears as the strong dependence of J_{th} on τ_p , thus showing the inverse

proportion relation as $J_{th} = J_{th0} + \frac{q}{\tau_p}$, where J_{th0} is the intrinsic threshold switching current density and q is an effective charge which represents the efficiency of the angular momentum transfer [107].

Taking into account the DW motion in flow regime, similar behavior is observed for our cases as shown in Fig. 5.5. Since the angular momentum transfer from spin current to the adjacent magnetic layer gives rise to the local magnetization switching of the DW, the intrinsic DW motion can be considered as the analogy of intrinsic switching in short pulse regime as well ($\tau_p^J \leq 100$ ns). The main difference is the presence of DW thus no additional in-plane field is required contrary to SOT switching. In this regard, the relation for the $J_{th,flow}$ on τ_p^J of the DW motion in flow regime is derived as following $J_{th,flow} = J_{th0,flow} + \frac{A}{\tau_p^J}$, where $J_{th0,flow}$ is the intrinsic threshold current density for DW motion, and A is an effective constant. Note that the quantification of A is not straightforward in this case unlike the switching. Because there are many uncertainties which contribute to the DW motion such as an ECT, the strength of DMI, and etc. By fitting the relation to the data, nevertheless, we can confirm that the relation nicely fits to the flow regime in all three regions, FM (orange), SAF (blue), and FM→SAF (green), respectively (Fig. 5.5). This trend has already been observed phenomenologically in previous studies with similar system as well [38]. Interestingly, we found that the dependence of $J_{th,flow}$ on τ_p^J in FM→SAF, is more significant compared to others, which is more similar to the switching behavior.

Let us focus on the thermally activated regime (orange shaded background in Fig. 5.5). In this case, the DW can move by external current flow in addition to the thermal fluctuations at finite temperature. The time scale for the thermal activation is typically much longer than the intrinsic flow regime (τ_p^J)100 ns). As soon as the energy delivered from the current is equivalent to the thermal activation energy barrier height, the DW depinning occurs. Therefore, we can evaluate the thermal activation energy barrier based on the Arrhenius relation as following $\tau_p^J = \tau_0 \exp(E_J^{eff}/k_B T)$, where τ_p^J is applied current pulse length, and τ_0 is thermal attempt time [39], [47], [125]. The effective energy barrier E_J^{eff} driven by CIDWM is given by $E_J^{eff} = E_J(1 - J_{th,therm}/J_{th0,therm})^\alpha$ with threshold current density J_{th0} to depin DW within infinitely long time and at zero temperature. Here, we define E_J as the thermal activation energy barrier at room temperature by assuming a finite thermal attempt time $\tau_0 =$

1 ns. The exponent α corresponds to the magnetization reversal mechanism which is either $\alpha = 1$ (DW propagation dominant), or $\alpha = 2$ (DW nucleation dominant)[43], [126]. In our study, we employed $\alpha = 1$ since DW depinning and injection is mainly governed by propagation dominant mechanism. By plotting an exponential fit (solid lines in Fig. 5.5) with the equation $J_{th,therm} = J_{th0,therm} (1 - \frac{k_B T}{E_J} \ln(\frac{\tau_P}{\tau_0}))$ ($T = 300 K$), consequently, E_J can be determined.

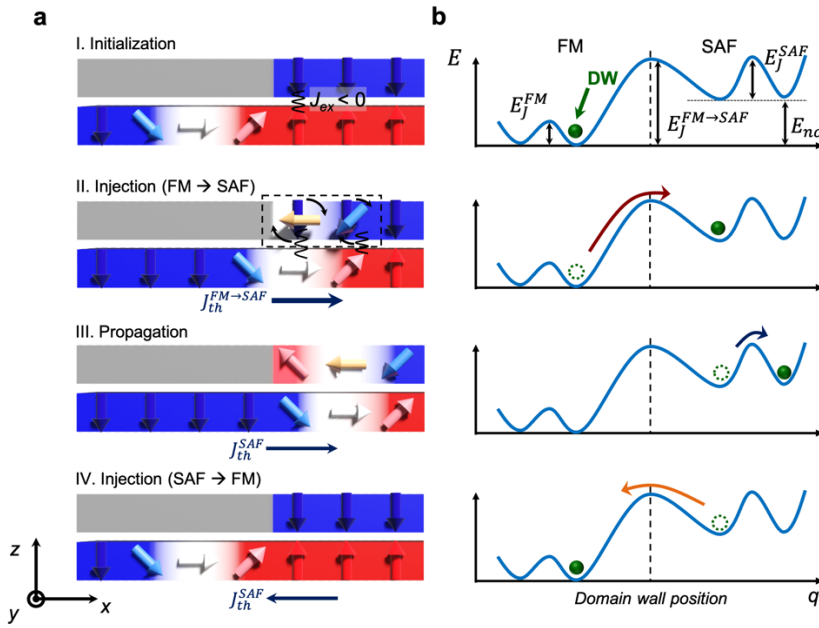


Figure 5.6. Energy landscape of DWs in SAF-FM junction ($\theta_j = 0^\circ$). Schematic illustrations of the (a) DW motion at the SAF-FM junction and (b) the corresponding energy landscape of DWs in each position at zero field. The energy barrier heights E_J^{FM} , E_J^{SAF} and $E_J^{FM \rightarrow SAF}$ are scaled with respect to measured values. Figure is adopted from [50].

As a result, the thermal activation energy barriers of the DWs demonstrated by current in the FM, SAF, and FM \rightarrow SAF region, are obtained as $E_J^{FM} \sim 26 k_B T$, $E_J^{SAF} \sim 35 k_B T$, and $E_J^{FM \rightarrow SAF} \sim 85 k_B T$, respectively. Fig. 5.6 depicts schematic illustrations of an energy landscape in the vicinity of the SAF-FM junction with respect to the DW position. Here note that the $\theta_j = 0^\circ$ in this case. Interestingly, the energy barrier of SAF is higher than those of value in FM ($E_J^{SAF} > E_J^{FM}$) which indicates the high thermal stability in SAF, whilst

$J_{th,flow}^{SAF} < J_{th,flow}^{FM}$ measured in the flow regime that is technologically more useful to the development of high-speed devices (Fig. 5.5). This is because the ECT is more effective at higher J (the flow regime) than at lower J (the thermally activated regime) [8]. In case of DW injection from FM to SAF, furthermore, the $E_j^{FM \rightarrow SAF}$ is surprisingly higher than FM and SAF, thereby supporting the large $J_{th}^{FM \rightarrow SAF}$ in both flow and thermally activated regimes. In addition, the discrepancy in $J_{th}^{FM \rightarrow SAF} > J_{th}^{SAF \rightarrow FM}$ originates from the unconventional asymmetric energy barrier (see II and IV in Fig. 5.6). This is due to the nucleation energy E_{nc} which requires to create one additional DW in the UM of SAF. Note that there is only one DW in FM, whilst SAF hosts one pair of DWs, one each in LM, and UM. Hence, the $E_j^{FM \rightarrow SAF}$ can be described as $E_j^{FM \rightarrow SAF} = E_{nc} + E_j^{SAF}$. As DW injects from SAF to FM, on the other hand, there is no need to nucleate additional DW, but the DW from the UM of SAF annihilates instead as shown in Fig. 5.6 IV. Therefore, the DW injection (FM \rightarrow SAF) can be understood by the combination of DW propagation (LM of SAF) and switching (UM of SAF) via interlayer exchange coupling ($J_{ex} < 0$). This also explains the strong dependence of $J_{th,flow}$ on τ_p^J in FM \rightarrow SAF which is feature of conventional switching.

5.3.2 Energy barriers derived from field-induced domain wall motion

In section 4.5, we also demonstrated the FIDWM in thermally activated regime. Fig. 5.7 shows the $H_{th,therm}^i$ versus τ_p^H obtained from the DW depinning measurement in FM and SAF region. In case of FIDWM, the DW depinning is governed by the Zeeman energy, not a spin current, thus external field induces the tilting of entire energy landscape with respect to DW. Despite the different mechanism, similar to the current case, E_H can be obtained from the fits to the equation $H_{th,therm} = H_{th0,therm} (1 - \frac{k_B T}{E_H} \ln(\frac{\tau_p^H}{\tau_0}))$ ($T = 300$ K) (solid lines in Fig. 5.7). $H_{th,therm}$ corresponds to collected threshold field H_{dep}^i ($i = \text{FM, and SAF}$) from DW depinning in each region, and $H_{th0,therm}$ refers to the field to depin DW within infinitely long time at zero temperature. τ_p^H is applied field pulse length, and τ_0 is thermal attempt time ($\tau_0 = 1$ ns). Based on the equation, we obtained the energy barriers for the FM and SAF regions as

$E_H^{FM} \sim 24 k_B T$, and $E_H^{SAF} \sim 28 k_B T$, respectively. Here note that the field-induced DW depinning was only able to perform in FM and SAF region, not in FM \rightarrow SAF. Therefore, the evaluation of energy barrier derived from the FIDWM at junction is impossible at this stage.

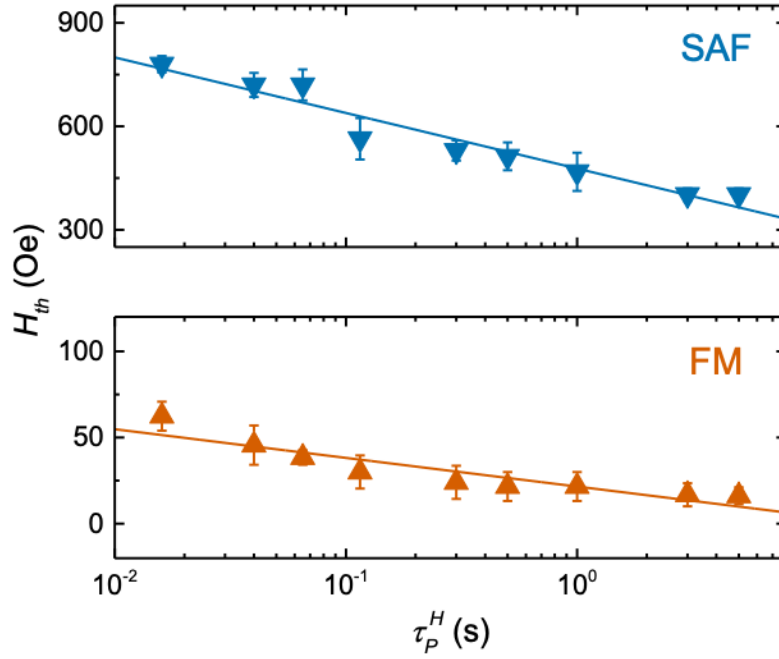


Figure 5.7. Threshold field as a function of pulse length in FM and SAF regions. Threshold DW depinning field H_{th}^i ($i = \text{FM or SAF}$) versus pulse length τ_p^H . Solid curves correspond to fits to the relation $H_{th,therm}^i \propto 1 - (1/E_H^i) \ln(\tau_p^H/\tau_0)$. The error bars correspond to the 25/75% probabilities. Figure is adopted from [50].

5.3.3 Comparison of energy barriers in current- and field-induced domain wall motion

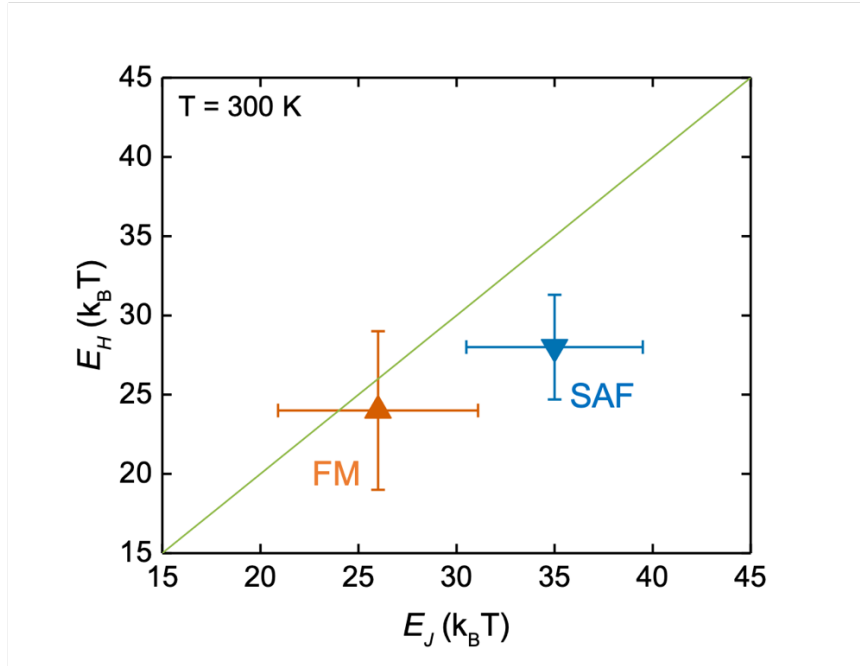


Figure 5.8. Comparison of current- and field-induced DW energy barriers. E_J versus E_H of FM (orange) and SAF (blue) region in thermally activated regime at $T = 300$ K. Green solid line corresponds to $E_J = E_H$. The error bars represent the standard deviation. Figure is adopted from [50]

For both the current and field case, we evaluated the energy barriers for FM and SAF, and those are compared in Fig. 5.8. Here, it clearly shows that $E_J^{SAF} > E_J^{FM}$ and $E_H^{SAF} > E_H^{FM}$ at room temperature. Thus, the DW in the SAF regions is more stable against currents, fields and thermal agitations. However, the DWs still can be more efficiently depinned by short current pulses (flow regime) in the SAF as compared to the FM regions, which highlights the technological supremacy of SAF. The physical origin why $E^{SAF} > E^{FM}$ is not very clear at present. We suppose that it may be because: (1) the DW volume of SAF is larger than FM, or (2) the reduced net magnetization in SAF makes the SAF less sensitive to the external excitations such as fields and current pulses in the thermally excited region in which the ECT is not large.

As summarized in Fig. 5.8, there is a clear difference between the SAF and FM cases. The ratio of the energy barriers for field versus current depinning is ~ 1 for the FM SOT case but is considerably reduced for the SAF case. This result is in accordance with the previous report that proves the existence of only single energy barrier of DWs in SOT driven FM unlike STT driven system [32], [38]. In case of STT driven DW motion, there exists both intrinsic and extrinsic barriers, thus achieving together high thermal stability and high current-induced motion efficiency by using two barriers [39]. However, it is not available in conventional SOT case due to the presence of single barrier which originates from an extrinsic pinning. On the other hands, the deviation between two measured energy barriers in SAF is observed as $E_j^{SAF} \gtrsim E_H^{SAF}$. The origin of is still not clear, but we suppose that it may be due to the degree of magnetization compensation and strength of interfacial anisotropy between LM and UM.

5.4 Two energy barriers in SAF-FM lateral junctions

In section 5.3, we discussed the origin of diode-like DW injection ($J_{th}^{FM \rightarrow SAF} \gg J_{th}^{SAF \rightarrow FM}$) behavior at the junction ($\theta_j = 0^\circ$) by showing the asymmetric energy barriers ($E_j^{FM \rightarrow SAF} \gg E_j^{SAF \rightarrow FM}$) derived from the current-induced motion in thermally activated regime. Contrary to FM and SAF, on the other hand, the demonstration of field-induced DW injection (or depinning) from FM to SAF was forbidden, thus the $E_H^{FM \rightarrow SAF}$ could not be evaluated. Although the $E_j^{FM \rightarrow SAF}$ gives rise to the highly asymmetric energy landscape at the junction ($\theta_j = 0^\circ$), it is not sufficient to explain the strong DW pinning over long time ($\tau_p^H \sim 2$ h) in the presence of large magnetic field ($H_z \sim 3$ kOe). In this section, we will discuss the origin of the strong field-induced DW pinning at the junction, based on the proposal of two energy barriers, namely local and global barriers. The local barrier is strongly correlated to the current-induced motion at zero field, whilst the global barrier only appears in the presence of field. Prior to main discussion of junction, we will first show how the external fields affect to the entire energy landscape of DW in FM and SAF region. At last, the junction tilting angle θ_j dependent DW injection energy barriers will be discussed as well.

5.4.1 Field-induced energy landscape for domain wall

For a better understanding, let us clarify the current-, and field-induced DW motions. For the FM and SAF cases, here, we consider SOT as a main source for spin current generation. The DW angle corresponds to the azimuthal angle ϕ since the polar angle $\theta = \frac{\pi}{2}$ in the middle of DW. Importantly, note that the energy landscape and barrier is a function of DW position q solely by definition as shown in Fig. 5.9.

In case of current cases, SOT drives a DW by a combined mechanism of DMI induced in-plane field and spin-orbit spin-current induced STT. Here the spin-orbit spin-current induced STT changes the DW angle ϕ . As an applied $J > J_{th}$, this increases the magnetic energy against the DMI, thereby changing θ and depinning the DW. Hence, the SOT does not affect the energy landscape or local barrier, as shown in Fig. 5.9b. Since the polarization of accumulated spin is always perpendicular to the DW angle ϕ , the direction of DW depinning is solely determined by the direction of applied current regardless of DW configuration.

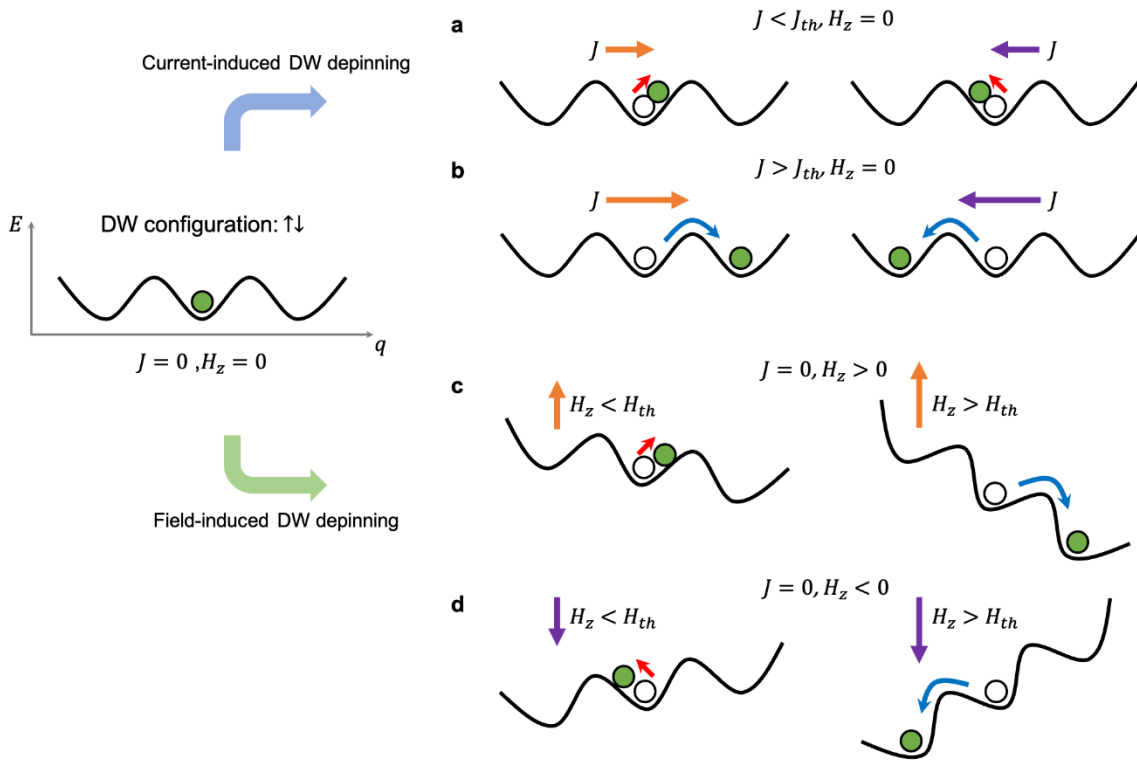


Figure 5.9. Illustration of DW depinning and energy landscapes for $\uparrow\downarrow$ DW configuration for the FM and SAF cases. (a, b) Current-induced DW depinning from a local energy barrier in the absence of external magnetic field. The DW stays at initial position q when applied $J < J_{th}$ (a), but depins only when $J > J_{th}$ (b). **(c, d)** Field-induced DW depinning from local energy barrier by external magnetic field. The entire energy landscape is tilted by applied field, thus DW depinning occurs when $H_z > H_{th}$.

In the steady state, on the other hand, the DW angle ϕ does not change but the DW position defined by θ changes by an easy axis component of field. For the FM or SAF case, an easy axis field that is larger than the H_{th} can depin DWs by tilting the DW energy landscape

and thereby overcoming the local energy barrier (see Fig. 5.9c, d). Note that field components perpendicular to the easy axis do not displace the DWs since they do not affect the energy landscapes. The key point here is that the global energy landscape is uniformly tilted over the whole FM or SAF, which just allows the DW to get out of the local energy barrier. In section 5.3.3, we experimentally showed that this local energy barrier can be obtained by both current- and field-induced DW depinning and proved that the $E_J \approx E_H$ in the FM.

Now let us consider the degree of field-induced tilting of the energy landscape. When the DW is positioned at $x = q$ with in the presence of an external magnetic field $\vec{H}(x, y, z)$, the energy landscape is determined by the Zeeman energy as

$$E_{ZE}(q) = - \int M(q, x) \hat{m}(q, x) \cdot \vec{H}(x, y, z) dx dy dz, \quad (5.1)$$

where $M(q, x)$ and $\hat{m}(q, x)$ are the magnitude of the magnetization and the unit vector along the magnetization at x as a function of q . Note that the volume integration is valid for the magnetic layers only. The racetrack wire direction and the easy magnetization axis are along the x and z -axes, respectively. The magnetizations and thicknesses for the magnetic layer in the FM are M_{FM} , and t_{FM} , respectively. Here we assume that the DW width (tens of nm) is much smaller than the length of FM wire L_{FM} (tens of μm). Thus, the magnetization of DW is negligible. If the DW with $\uparrow\downarrow$ configuration is located at $x = q$ in the FM region ($0 < q < L_{FM}$), consequently, the energy can be described as

$$\begin{aligned} E_{ZE}^{FM}(q) &= -wt_{FM}(-L_{FM} + q)M_{FM}H_z - wt_{FM}qM_{FM}H_z \\ &= -wt_{FM}(L_{FM} + 2q)M_{FM}H_z. \end{aligned} \quad (5.2)$$

Note that this equation does not take into account the local energy barrier. Here, we can clearly see the slope of the energy landscape is defined as

$$\eta_{\uparrow\downarrow}^{FM} = -2wt_{FM}M_{FM}H_z. \quad (5.3)$$

Therefore, an easy-axis component of positive external field $+H_z$ gives rise to the negative η in the total energy landscape, and the degree of tilting is linearly proportional to the $|H_z|$.

5.4.2 Determination of field-induced energy landscape in synthetic antiferromagnet

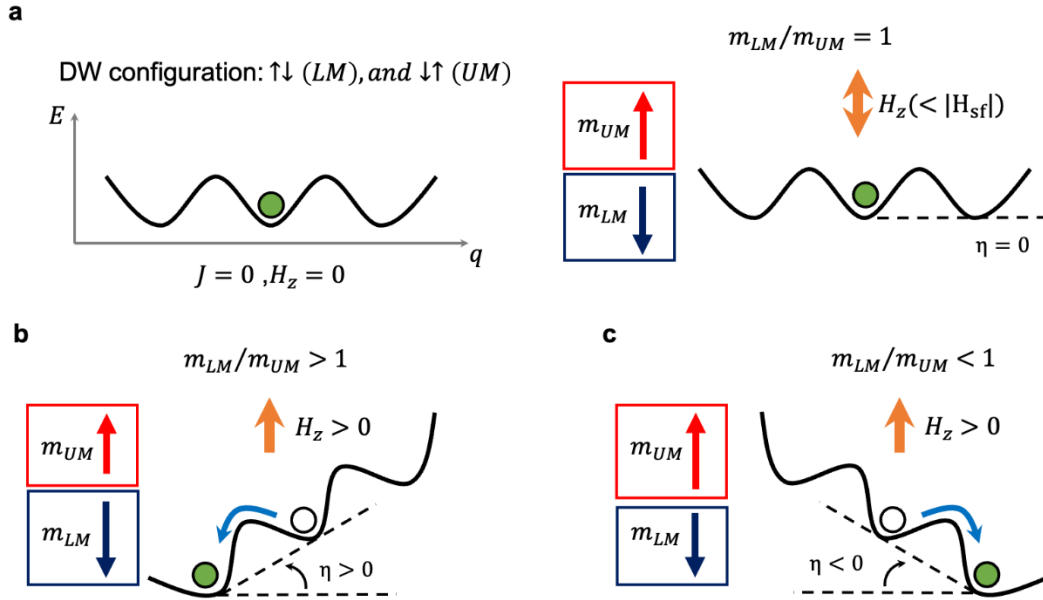


Figure 5.10. Illustration of the field-induced energy landscape for $\uparrow\downarrow$ DW configuration (LM) in the SAF. Steady state of DW with the $\uparrow\downarrow$ configuration (LM) sitting at $x = q$ in SAF, and the energy landscape in the presence of external field H_z for (a) $m_{LM}/m_{UM} = 1$, (b) $m_{LM}/m_{UM} > 1$, and (c) $m_{LM}/m_{UM} < 1$. The slope of energy landscape is described as $\eta_{\uparrow\downarrow}^{SAF} = 2w(t_{UM}M_{UM} - t_{LM}M_{LM})H_z$. Note that the wiggles in the energy landscapes illustrate the local DW pinning potential barrier.

As discussed above, the direction of field-induced DW depinning is governed by the Zeeman energy and corresponding DW configuration. This is easy to understand in case of the FM since the net magnetization M_{FM} simply originates from a single magnetic layer. In contrast, the net moment of SAF varies depending upon the magnitude of each moment in LM (m_{LM}), and UM (m_{UM}), which are oppositely aligned to each other. For that reason, it is essential to know m_{LM}/m_{UM} for establishing the field-induced energy landscape in SAF. Let us first consider the Zeeman energy in the SAF. Similar to the FM, we consider a SAF nanowire with length L_{SAF} and width w . The DW is sitting at $x = q$ ($0 < q < L_{SAF}$), in the presence of

an external magnetic field $\vec{H}(x, y, z)$. Here we assume that the DW configuration with $\uparrow\downarrow$ in the LM, and $\downarrow\uparrow$ in the UM. By following the equation above, the Zeeman energy in SAF is given by

$$\begin{aligned} E_{ZE}^{SAF}(q) &= -wt_{LM}qM_{LM}H_z + wt_{LM}(L_{SAF} - q)M_{LM}H_z + wt_{UM}qM_{UM}H_z \\ &\quad - wt_{UM}(L_{SAF} - q)M_{UM}H_z \\ &= w(2q - L_{SAF})(t_{UM}M_{UM} - t_{LM}M_{LM})H_z. \end{aligned} \quad (5.4)$$

where, M_{LM} , M_{UM} , t_{LM} and t_{UM} , are the magnetizations and thickness for the LM and UM layers in the SAF, respectively. As a result, the slope of the energy landscape is described as

$$\eta_{\uparrow\downarrow}^{SAF} = 2w(t_{UM}M_{UM} - t_{LM}M_{LM})H_z. \quad (5.5)$$

Note that the subscript $\uparrow\downarrow$ represent the DW configuration of LM. Let us compare the m_{LM}/m_{UM} ($= \frac{t_{LM}M_{LM}}{t_{UM}M_{UM}}$) dependence of $\eta_{\uparrow\downarrow}^{SAF}$. In case of $m_{LM}/m_{UM} = 1$, the LM and UM are totally compensated like an ideal AF, thereby resulting $\eta_{\uparrow\downarrow}^{SAF} = 0$. Consequently, an external field does not contribute to the energy landscape. Here the magnitude of H_z must be smaller than $|H_{sf}|$. If $m_{LM}/m_{UM} > 1$, however, the $\eta_{\uparrow\downarrow}^{SAF} < 0$, thus the DW depins to the right-hand side in the presence of positive H_z . On the other hand, the $\eta_{\uparrow\downarrow}^{SAF} > 0$ when $m_{LM}/m_{UM} < 1$ and the DW depins opposite direction under the same condition as shown in Fig. 5.10.

This can eventually explain why the direction of FIDWM is opposite to the FM in the presence of an external field as presented in section 4.5.2. For our SAF structure, the UM is designed to be slightly thicker than LM so that $m_{LM}/m_{UM} = 0.95$ (see section 4.1). Therefore, the positive external field gives rise to the $\eta_{\uparrow\downarrow}^{SAF} > 0$ and the DW with $\uparrow\downarrow$ configuration (LM) moves to the left-hand side. Note that an averaged Kerr contrast of SAF reflects the configuration of LM due to the strong spin-orbit coupling induced by Pt/Co interface despite $m_{UM} > m_{LM}$. It is noteworthy to mention that the SOT in SAF is applied mainly to LM, so that the DW always moves along the applied current direction regardless of m_{LM}/m_{UM} .

5.4.3 Local and field-induced global energy barriers at the junction

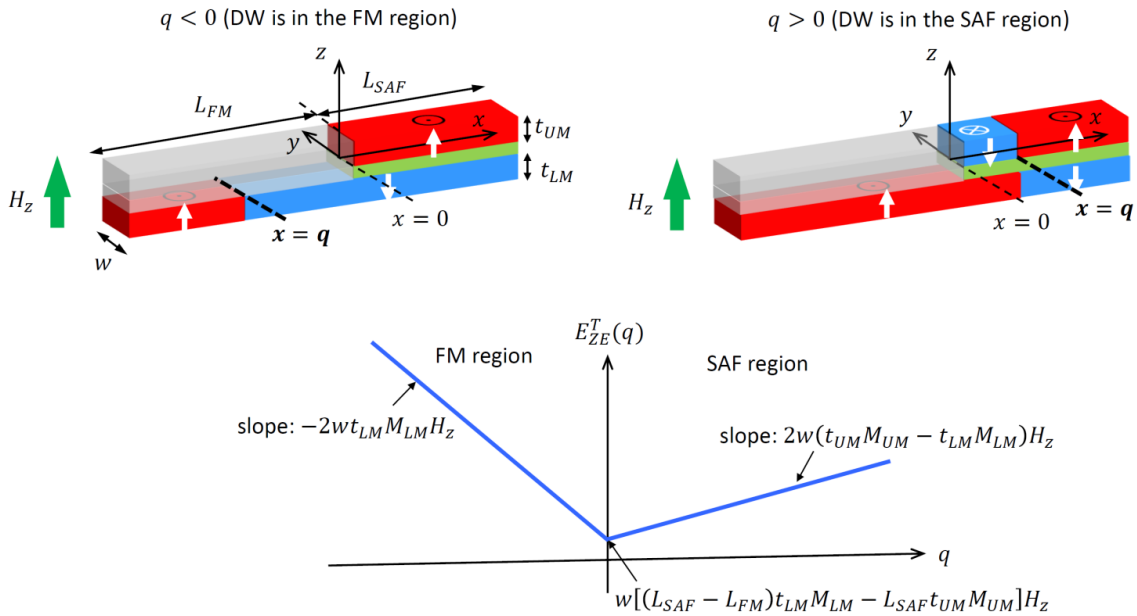


Figure 5.11. Illustration of field-induced energy landscapes and global energy barriers for $\uparrow\downarrow$ domain walls in a SAF-FM junction. Upper left panel: $\uparrow\downarrow$ DW in the FM region ($q < 0$). Upper right panel: $\uparrow\downarrow$ DW in the LM of the SAF region ($q > 0$). Lower panel: Field induced energy landscape in the FM-SAF junction with $t_{UM}M_{UM} > t_{LM}M_{LM}$. Figure is adopted from [50].

So far, we have established the energy barriers for CIDWM and FIDWM in each FM and SAF region based on the local pinning potential and field-induced energy landscape, respectively. In particular, the m_{LM}/m_{UM} dependence of energy landscape for SAF is found to be a unique phenomenon which has never been considered in conventional FM case. In section 5.3.1, we showed the asymmetric local DW pinning barrier ($E_j^{SAF \rightarrow FM} \ll E_j^{FM \rightarrow SAF} = E_{nc} + E_j^{SAF}$) at the junction ($\theta_j = 0$) as the DW injects from FM to SAF. Despite the large E_{nc} , the field-induced DW injection is forbidden that is unusual, hence we need to establish the total energy landscape in a SAF-FM lateral junction in the presence of external field. Let us consider the junction with $\theta_j = 0$ in which the junction boundary is located at $x = 0$ in a wire with length $L_{FM} + L_{SAF}$ (FM region: L_{FM} , SAF region: L_{SAF}) and width w as shown in Fig. 5.11.

The DW with $\uparrow\downarrow$ configuration is located at $x = q$ either in the FM region ($-L_{FM} < q < 0$) or in the SAF region ($0 < q < L_{SAF}$). Note that the DW with $\uparrow\downarrow$ configuration in FM corresponds to $\uparrow\downarrow$ in the LM and $\downarrow\uparrow$ in the UM in SAF. By employing the equation derived in previous sections, the corresponding Zeeman energy for FM and SAF can be rewritten as

$$\begin{aligned} E_{ZE}^{FM}(q) &= -wt_{LM}(L_{FM} + q)M_{LM}H_z - wt_{LM}qM_{LM}H_z \\ &= -wt_{LM}(L_{FM} + 2q)M_{LM}H_z \end{aligned} \quad (-L_{FM} < q < 0), \quad (5.6)$$

$$\begin{aligned} E_{ZE}^{SAF}(q) &= -wt_{LM}qM_{LM}H_z + wt_{LM}(L_{SAF} - q)M_{LM}H_z \\ &\quad + wt_{UM}qM_{UM}H_z - wt_{UM}(L_{SAF} - q)M_{UM}H_z \quad (0 < q < L_{SAF}). \quad (5.7) \\ &= w(2q - L_{SAF})(t_{UM}M_{UM} - t_{LM}M_{LM})H_z \end{aligned}$$

Hence, the total energy landscapes for the cases that the DW is located in the FM and SAF regions are, respectively,

$$\begin{aligned} E_{ZE}^T(q < 0: FM) &= E_{ZE}^{FM}(q) + E_{ZE}^{SAF}(0) \\ &= -w[2qt_{LM}M_{LM} + (L_{FM} - L_{SAF})t_{LM}M_{LM} + L_{SAF}t_{UM}M_{UM}]H_z \end{aligned} \quad (5.8)$$

$$\begin{aligned} E_{ZE}^T(q > 0: SAF) &= E_{ZE}^{FM}(0) + E_{ZE}^{SAF}(q) \\ &= w[2q(t_{UM}M_{UM} - t_{LM}M_{LM}) \\ &\quad - (L_{FM} - L_{SAF})t_{LM}M_{LM} - L_{SAF}t_{UM}M_{UM}]H_z \end{aligned} \quad (5.9)$$

According to E_{ZE}^T , when $H_z > 0$, the slopes of energy landscapes η vs. q for the cases that the DW is located in the FM ($q < 0$) and SAF regions ($q > 0$) are negative ($-2wt_{LM}M_{LM}H_z$) and positive ($2w(t_{UM}M_{UM} - t_{LM}M_{LM})H_z$), respectively, since $t_{UM}M_{UM} > t_{LM}M_{LM}$ in our SAF. This indicates that the DW is trapped at $x = 0$ (the junction boundary) due to the formation of a field-induced energy landscape of SAF, namely global energy barrier. On the other hand, when $H_z < 0$, the signs of the η change so that the DW moves away from $x = 0$. For a DW with $\downarrow\uparrow$, then the opposite is true.

Hence, we define the two energy barriers for DWs at the boundary of SAF-FM junction. One is the asymmetric local DW pinning potential corresponding to $E_{nc} + E_J^{SAF}$. The energy E_{nc} is required to nucleate a DW in the UM of the SAF region. It is experimentally demonstrated that the DW can overcome this local barrier as the J is large enough ($> J_{th}^{FM \rightarrow SAF}$). Another is the global energy barrier, which is equivalent to field-induced energy landscape of SAF. This global barrier is only activated in the presence of H_z that induces DW motion towards junction boundary. Here, the stronger H_z for the DW motion induces the stiffer global barrier. Thus, we conclude that the field-induced DW injection is impossible due to the global energy barrier.

5.4.4 Junction tilting angle dependent energy barrier at the junction

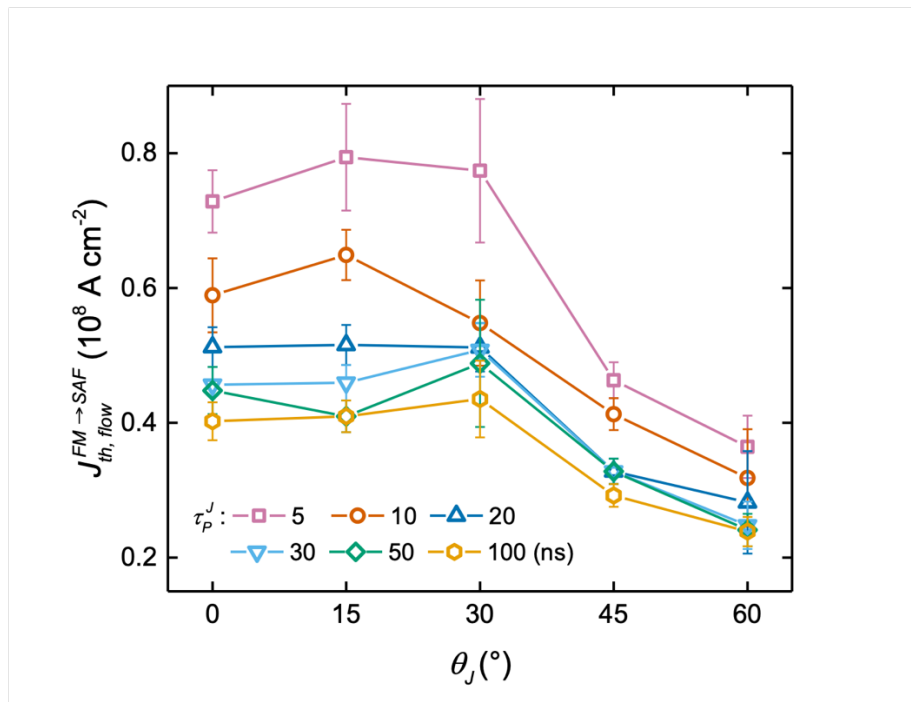


Figure 5.12. Junction tilting angle dependent DW injection threshold current density in the flow regime. $J_{th, flow}^{FM \rightarrow SAF}$ versus θ_J were measured in $\tau_P^J = 10$ ns (orange squares), 20 ns (blue triangles), 30 ns (light blue triangles), 50 ns (green diamonds), and 100 ns (yellow hexagons). The error bars represent 25/75% injection probabilities. Figure is adopted from [50]

In contrast to the extreme stability of the trapped DW to magnetic field, a DW can be expelled from the FM region into the neighboring SAF regions by current pulses, although, as discussed above $J_{th,flow}^{FM \rightarrow SAF}$ is large for $\theta_j = 0$, and we note that $J_{th,flow}^{FM \rightarrow SAF} > J_{th,flow}^{SAF \rightarrow FM}$, as discussed above. This large $J_{th,flow}^{FM \rightarrow SAF}$ is consistent with the large value of $E_j^{FM \rightarrow SAF} \sim 85 k_B T$ ($T=300$ K) that was obtained from the thermally activated regime measurements (section 5.3.1). Most importantly, we find that $J_{th,flow}^{FM \rightarrow SAF}$ depends sensitively on θ_j , decreasing with increasing θ_j for $\theta_j > 30^\circ$ (Fig. 5b). $J_{th,flow}^{FM \rightarrow SAF}$ is nearly constant for $\theta_j \leq 30^\circ$, as shown in Fig. 5.12. This is because the DW in the FM region aligns itself parallel to the junction boundary for small θ_j ($\leq 30^\circ$) when a current pulse is applied. For larger θ_j this is no longer the case due to the competition between the increased DW energy versus decreased dipolar energy[58], [127], [128]. Note that the $J_{th,flow}^{FM \rightarrow SAF}$ approaches to $J_{th,flow}^{SAF}$ with increasing θ_j . Also we find that the dependence of $E_j^{FM \rightarrow SAF}$ and $J_{th0,flow}^{FM \rightarrow SAF}$ on θ_j that was obtained from thermally activated regime measurements shows a similar trend to that of $J_{th,flow}^{FM \rightarrow SAF}$ on θ_j (Fig. 5.13a).

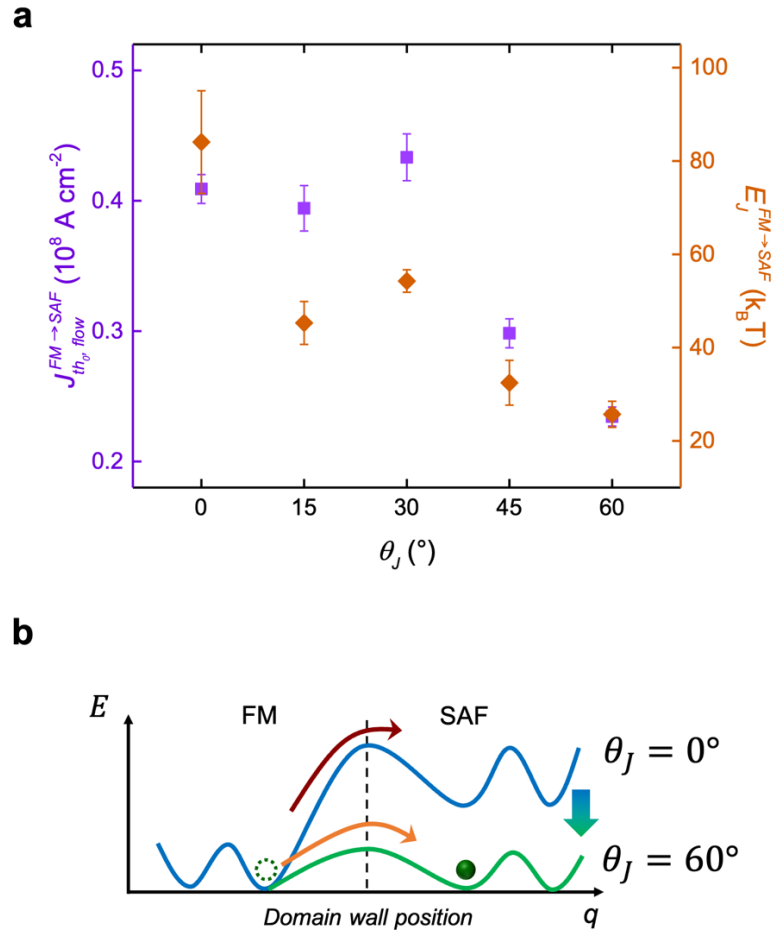


Figure 5.13. Junction tilting angle dependent DW injection energy barriers. (a) θ_J dependent $J_{th,flow}^{FM \rightarrow SAF}$ (purple squares) and $E_J^{FM \rightarrow SAF}$ (orange diamonds). Note that $J_{th,flow}^{FM \rightarrow SAF}$ and $E_J^{FM \rightarrow SAF}$ are derived from the flow and thermally activated regime, respectively. The error bars represent the standard deviation. **(b)** Illustration of current-induced DW injection energy barrier at junction with $\theta_J = 0^\circ$ (blue) and 60° (green). Note that $E_J^{FM \rightarrow SAF}$ decreases with increasing θ_J . Figure is adopted from [50].

These observations are consistent with our proposed mechanism following: the effective initial nucleation volume in the UM in the SAF region decreases with increasing θ_J , thereby, decreasing $J_{th,flow}^{FM \rightarrow SAF}$ and $E_J^{FM \rightarrow SAF}$. Let us assume that the DW cross sectional area A_{UM} in the upper layer is $A_{UM} = t_{UM}x \cot \theta_J$ where x is the distance between the junction endpoint and the DW (see Fig. 5.14). As the DW propagates (i.e. x increases) reaching $x =$

$w \tan \theta_j$ in the tilted junction region, $A_{UM} = t_{UM} w$. Consequently, we find that $\frac{dA_{UM}}{dx} = t_{UM} \cot \theta_j$ thereby showing that the larger θ_j is the smaller is $\frac{dA_{UM}}{dx}$. This means that the gradient of DW volume to be nucleated decreases with increasing θ_j , as the DW propagates in the junction region, consequently making it easier for the DW to propagate at larger θ_j .

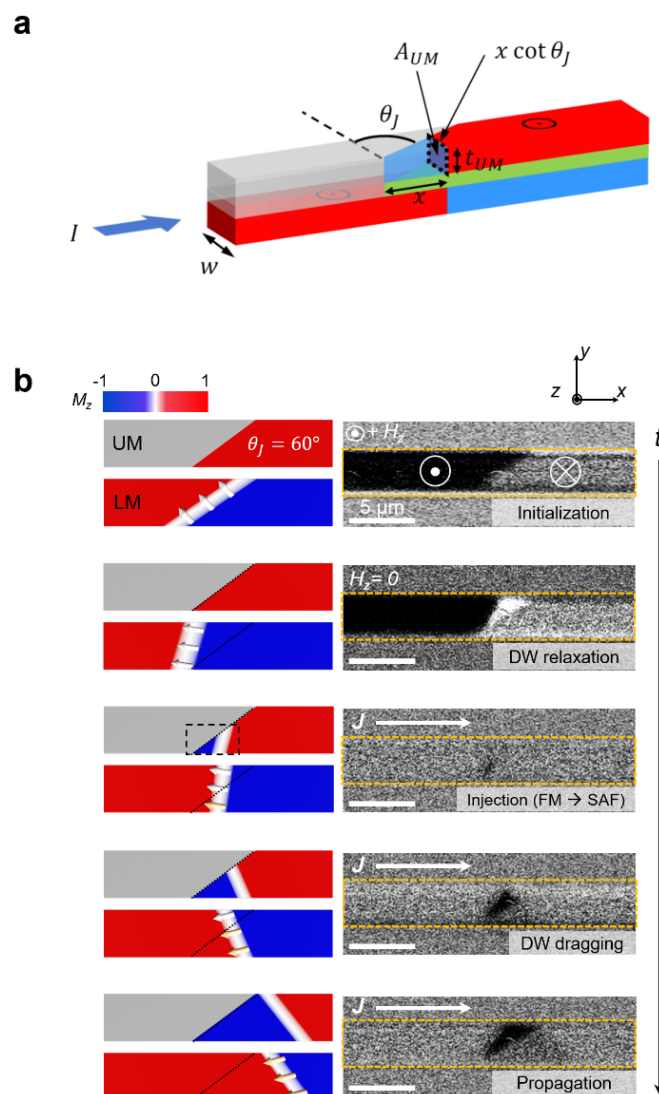


Figure 5.14. Domain wall injection into tilted SAF-FM junctions. A, Illustration of domain wall injection from FM to SAF region in the tilted FM-SAF junctions. **B,** Schematic illustrations and corresponding Kerr microscope images of domain wall injection from FM to SAF region at $\theta_j = 60^\circ$. Figure is adopted from [50].

5.5 Thermal stability of domain wall in SAF-FM lateral junctions

As discussed in section 2.3.3, the thermal stability of the non-volatility of the magnetic memory device can be evaluated from the corresponding energy barrier E by following relation as $\Delta = \frac{E}{k_B T}$, where the Δ is the thermal stability factor, k_B is the Boltzmann constant, and T is the finite temperature, respectively. To consider it for reliable memory devices, it is known that $\Delta > 40$ is required to retain the data against the thermal fluctuation at room temperature for over a decade [44]. For the DWs in FM-based racetrack memory, the determination of Δ is straightforward since there is a single E which is equivalent to both current and field-induced case ($E_J^{FM} \approx E_H^{FM}$). However, this is not simple for SAF and SAF-FM junction cases. Because SAF exhibits a discrepancy between energy barriers ($E_J^{SAF} \neq E_H^{SAF}$) and even the evaluation of E_H is not possible in SAF-FM junction due to the unconventional field-induced global energy barrier. In this section, we discuss how to evaluate the thermal stability in those cases by performing the temperature dependent current-induced DW depinning measurement. The energy barriers for FM, SAF, and SAF-FM junction are compared at 300 and 400 K, respectively. Based on the results, more importantly, we show that the thermal fluctuation is equivalent to the random field fluctuation, thereby, confirming the extremely high thermal stability in the SAF-FM junction.

5.5.1 Thermally-induced domain wall depinning at the junction

For direct demonstration of thermally-induced DW depinning, we firstly carried out an experiment to check the DW stability by monitoring the displacement of the DW position in the SAF-FM junction boundary region at different temperatures over extended time periods. Unfortunately, it was not possible to observe the DW motion under the over sixty hours of heating up to at 100, 150, and 200 °C. In reality, we found that it was very hard to quantify key

parameters for obtaining the energy barrier in such an experiment. However, it is widely known that thermal depinning of DWs is induced by thermally fluctuating magnetic fields due to microscopic degrees of freedom of the environment, such as phonons, conduction electrons or nuclear spins. Hence we investigate the DW dynamics including the thermal agitation that can be described by the stochastic Landau-Lifshitz-Gilbert equation (Langevin equation) as introduced in section 2.3.3.3 (Eq. 2.31),

$$\frac{d\vec{M}}{dt} = -\gamma\vec{M} \times (\vec{H}_{eff} + \vec{H}_{fl}) + \alpha\vec{M} \times \frac{d\vec{M}}{dt} \quad (2.31)$$

where γ , \mathbf{H}_{eff} , $\mathbf{H}_{fl}(\mathbf{r}, t)$ and α are the gyromagnetic ratio, the effective magnetic field, the random thermal fluctuating magnetic field, and the Gilbert damping, respectively. \mathbf{H}_{eff} includes the external field, the exchange field, the dipolar field, the DMI field, and the anisotropy field. $\mathbf{H}_{fl}(\mathbf{r}, t)$ is typically assumed to be a Gaussian random process satisfying $\langle H_{fl}^i(\vec{r}, t) \rangle = 0$ and $\langle H_{fl}^i(\vec{r}, t) H_{fl}^j(\vec{r}', t') \rangle = \frac{2\alpha k_B T}{\gamma \mu_0 M} \delta_{ij} \delta(\vec{r} - \vec{r}') \delta(t - t')$ ($i, j = x, y, z$) such that

$$\vec{H}_{fl}(\vec{r}, t) = \vec{\zeta}(\vec{r}, t) \sqrt{\frac{2\alpha k_B T}{\gamma \mu_0 M dV dt}} \quad (2.32)$$

where k_B , T , μ_0 , dV , dt , and $\zeta(\mathbf{r}, t)$ are the Boltzmann constant, temperature, magnetic permeability, fluctuating element volume, fluctuating time interval, and stochastic random unit vector, respectively. δ_{ij} is the Kronecker delta. $\delta(\mathbf{r} - \mathbf{r}')$ and $\delta(t - t')$ are Dirac delta functions. dV can be approximated to be the DW volume, $wt_{FM}\pi\Delta$ (width of wire : w , FM thickness: t_{FM} , DW width parameter: Δ). If we employ $\alpha = 0.1$, $T = 300$ K, $M = 600$ emu/cc, $dV = wt_{FM}\pi\Delta = 2.5 \times 10^{-17}$ cm³ ($w = 2$ μ m, $t_{FM} = 1$ nm, $\Delta = 4$ nm) and $\Delta t = 1$ ps, we obtain $\max(H_{fl}^z) \sim 177$ Oe that may depin the DW from any extrinsic pinning potential in the energy landscape over an extended time in either the FM or SAF region (e.g. see Fig. 5.6). Here note that only the z -component (easy-axis of FM and SAF) of \mathbf{H}_{fl} has been considered since the other components (x and y) cannot depin the DWs. Note also that $\max(H_{fl}^z)$ cannot be considered to the DC DW depinning field pulse in the FM region ($H_{th}^{FM} \sim 30$ Oe) since the time scale for H_{fl}^z is ~ 1 ps.

Now let us investigate how the \vec{H}_{fl} can depin the DWs depending on where the $\uparrow\downarrow$ DW is positioned (see Fig. 5.15). When the DW is in the FM (case I. $q < 0$) or in the SAF (case III. $q > 0$), the DW is depinned by \vec{H}_{fl} that is applied to the DW at $x = q$ and at a certain time scale t . The direction of the depinning torque τ_{DW} and the corresponding DW velocity v_{DW} are determined by the sign of $H_{fl}^z(q, t)$. For example, when $q < 0$ (FM region) and $H_{fl}^z(q, t) > 0$, $\tau_{DW}^z > 0$ and $v_{DW}^x > 0$ (case I in Fig. 5.15). On the other hand, when $q > 0$ (SAF region) and $H_{fl}^z(q, t) > 0$, $\tau_{DW}^z > 0$ and $v_{DW}^x < 0$ since the $\frac{m_{UM}}{m_{LM}} > 1$ in the SAF region such that the DW configuration is $\downarrow\uparrow$ as seen from the m_{net} landscape (case III in Fig. 5.15). As $H_{fl}^z(q, t)$ changes sign, then these statements are vice versa for both the FM and the SAF regions.

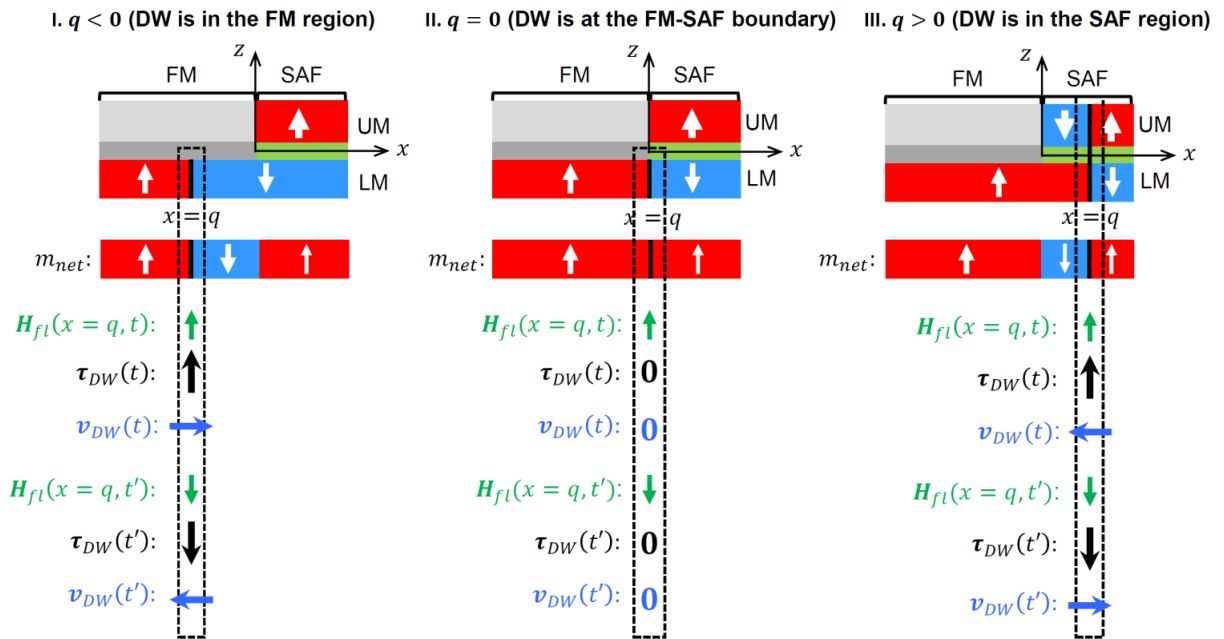


Figure 5.15. Illustration of thermal fluctuation torques depending on the DW position in FM-SAF junction. i, $\uparrow\downarrow$ DW in the FM region ($q < 0$), ii: $\uparrow\downarrow$ DW on the boundary ($q = 0$), iii: $\uparrow\downarrow$ DW in the lower layer of the SAF region ($q > 0$). Figure is adopted from [50]

When $q = 0$ (case II. DW is at the SAF-FM junction boundary), in contrast, the situation is different from the others: there is effectively no DW (see the net magnetic moment m_{net} landscape in case II in Fig. 5.15). This is a very special case, thus corresponding to a singular point at which the entire wire is nothing but a single domain due to the fact that the m_{UM} is larger than the m_{LM} in the SAF region. This suggests that any direction of \vec{H}_{fl} cannot depin or move the DW at singular point $q = 0$ unless a new DW is created, thus showing that

Chapter 5

the DW at the SAF-FM junction boundary is extremely stable against the magnetic field fluctuation, which is equivalent to the thermal fluctuation.

5.5.2 Effect of electrical current fluctuations on domain wall depinning

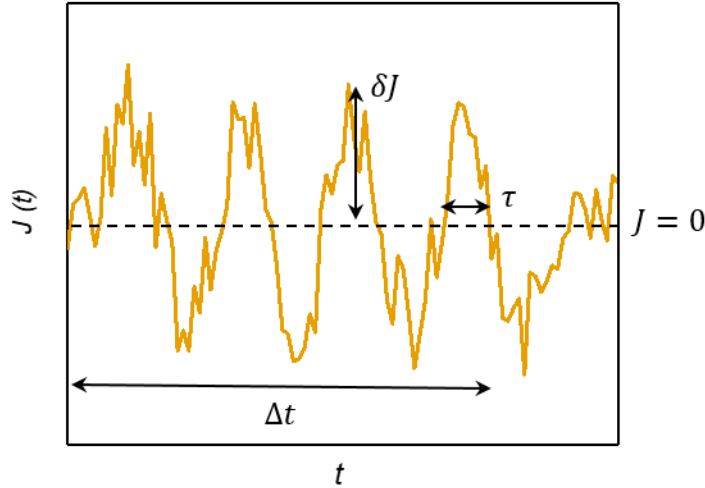


Figure 5.16. Illustration of electrical current density fluctuation induced by thermal energy in equilibrium. Schematic illustrations of exemplary current density fluctuation as a function of time in equilibrium ($J = 0$) with the average magnitude of fluctuation δJ . Here, we assume that J obeys Gaussian distribution.

Despite the thermal fluctuation field model, the direct experimental proofs on the influence of thermal fluctuation on DWs have never been reported due to the difficulties as mentioned in previous section. Furthermore, the thermal agitation also gives rise to the fluctuation of conduction electrons thereby resulting spin current as well. To exclude the effect of current fluctuation on the DWs, it is crucial to investigate the effect of the electrical current fluctuation in the given system and compare those of values with the DW depinning threshold J_{th}^i ($i = FM, SAF, \text{ or } FM \rightarrow SAF$). Since, at finite temperatures, electrical current fluctuations induced by thermal effects may depin DWs if the fluctuations are large enough to overcome the local energy barrier even in equilibrium. Here we quantify the magnitudes of such fluctuations to investigate how they affect the DW motion and depinning based on the fluctuation-dissipation theorem (see section 2.3.3.2).

We assume here that the current density randomly fluctuates with a magnitude of δJ with respect to the applied current density J . If a DW is depinned within the time Δt that is

much larger than τ , we obtain the average magnitude δJ by integrating the above equation with respect to ω , for the interval $0 < \omega < \frac{\pi}{\Delta t}$ as follows:

$$\delta J = \sqrt{\frac{k_B T}{V} \cdot \frac{\sigma}{\Delta t}} \quad \left(0 < \omega < \frac{\pi}{\Delta t}\right) \quad (2.29)$$

where σ is the d.c. conductivity ($\omega = 0$). Using $T = 300$ K, $\sigma \sim 1.28 \times 10^6 \Omega^{-1} \text{m}^{-1}$, DW volume $V_{DW} \sim 2.5 \times 10^4 \text{ nm}^3$ and $\Delta t = 1$ ns, we obtain $\delta J \cong 4.5 \times 10^4 \text{ A/cm}^2$. These values are much smaller than $J_{th}^i \sim 10^7 \text{ A/cm}^2$ by more than two orders of magnitude ($i = \text{FM, SAF, and FM} \rightarrow \text{SAF}$), thus showing that the DW depinning induced by thermally driven current density fluctuations is negligible.

As a result, we estimate the DW depinning probability P induced by current density fluctuations within a long period of time t as follows:

$$\ln P \sim -\frac{(J/\delta J)^2}{2} + \ln(t/\Delta t). \quad (5.10)$$

If we take $J_{th}^{SAF} \sim 3.0 \times 10^7 \text{ A/cm}^2$, $\delta J \cong 4.5 \times 10^4 \text{ A/cm}^2$, $t = 10^{10}$ sec, and $\Delta t = 1$ ns, we obtain $P \sim e^{-2.2 \times 10^5} \sim 10^{-10^5}$. Consequently, the depinning probability by δJ is eventually zero over a 300 year ($\cong 10^{10}$ sec) time period. In principle, we confirm that the current density fluctuations induced by thermal effect in our devices are negligibly small, thereby playing no role in the DW depinning.

5.5.3 Temperature dependent energy barriers for domain walls

For the experimental proof of the high thermal stability of SAF-FM junction, most importantly, we also first tried to perform the field-induced DW injection from FM to SAF region across the junction at high temperature ($T = 400\text{ K}$), but it was not able to be made as we expected in section 5.5.1. We confirm that the field-induced global barrier firmly inhibits the DW injection into SAF even at higher temperature. Thus, the quantification of energy barrier by field-induced injection was not possible. Therefore, we demonstrated the current-induced DW depinning and injection at $T = 400\text{ K}$ in FM, SAF, and FM \rightarrow SAF regions, then compare the energy barriers with those of values measured at $T = 300\text{ K}$, respectively.

From temperature dependent experiments, as shown in Fig. 5.17c, we first find that thermal effects induce magnetic fluctuation fields, i.e. a thermal-magnetic field equivalence, that more tightly bind DWs in the junction with increasing temperature, thus significantly increasing both the global energy barriers and the injection threshold current densities ($J_{th,therm,T=400K}^{FM\rightarrow SAF} > J_{th,therm,T=300K}^{FM\rightarrow SAF}$). This is in sharp contrast with DWs in FM or SAF regions in which the thermal fluctuation fields assist to depin DWs, thereby decreasing the threshold current densities $J_{th,therm}^i$ ($i = FM\text{ or }SAF$) very much while keeping the energy barriers E_j^i ($i = FM\text{ or }SAF$) constant. The E_j for FM, SAF and SAF-FM junction are obtained by measuring τ_p^J dependent $J_{th,therm}$ at $T = 300\text{ K}$ and 400 K in the thermal activation regime in the absence of external magnetic fields (see Fig. 5.17d). Note here that the E_j for the SAF-FM junction corresponds to the case that the DW is injected from FM to SAF by a current pulse along $+q$ -direction, that is, the current induced torque $\tau_j > 0$ (see Fig. 5.18). The DW with a $\uparrow\downarrow$ configuration has been used for all the experiments but the results are identical for the other DW configuration ($\downarrow\uparrow$).

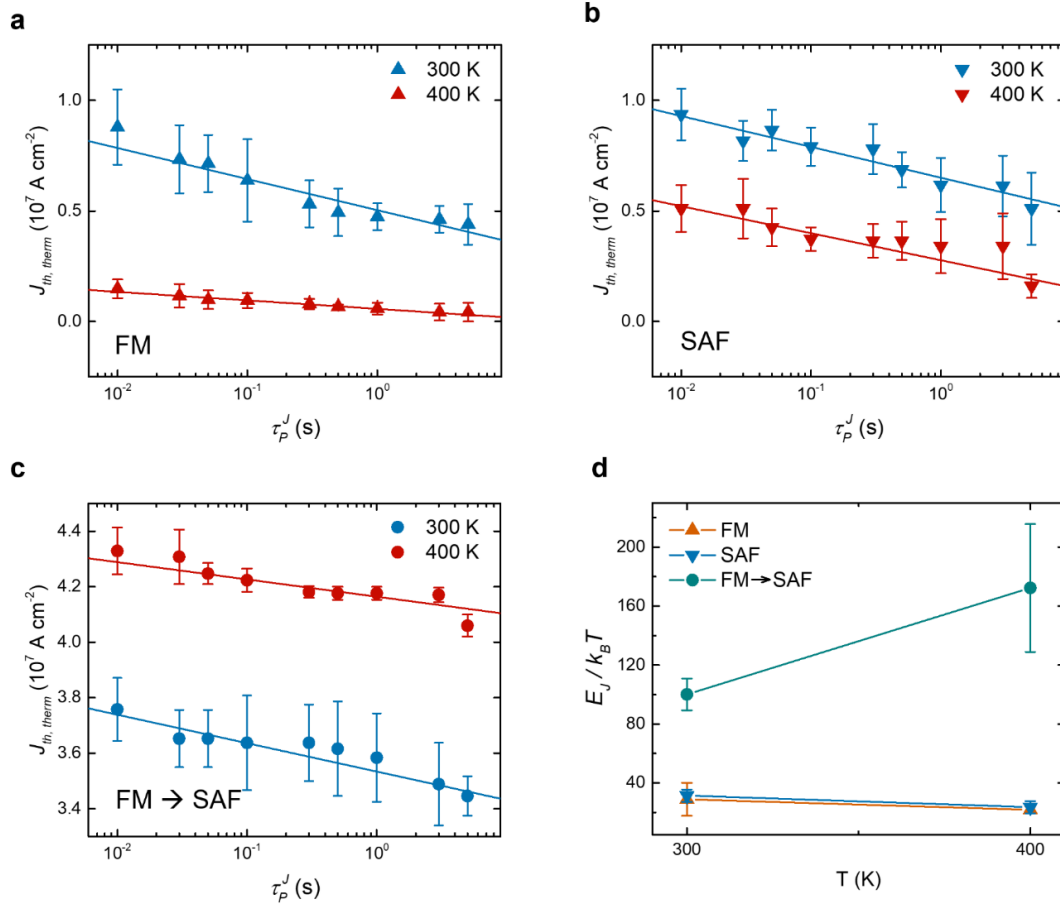


Figure 5.17. Temperature dependent current-induced DW depinning and energy barriers.

a-c, Threshold current density $J_{th,therm}$ versus current pulse length τ_p^J in the thermal activation regime at temperature $T = 300$ K (blue) and 400 K (red) **a:** FM region, **b:** SAF region, and **c:** SAF-FM junction. Solid lines correspond to the fitted ones. **d,** Energy barrier E_J normalized by $k_B T$ versus T . The error bars correspond to one standard deviation. Figure is adopted from [50].

First, we find that the $J_{th,therm}^{FM \rightarrow SAF}$ for the SAF-FM junction with $\theta_j = 0$ is larger at $T = 400$ K as compared to that at $T = 300$ K (see Fig. 5.17c and Table 5.1). This is in sharp contrast with what we observe for the FM (Fig. 5.17a) and SAF (Fig. 5.17b) cases in which both $J_{th,therm}^{FM}$ and $J_{th,therm}^{SAF}$ rather decrease with increasing T . Note that not only the magnitude of $J_{th,therm}$ but also the slope of $J_{th,therm}$ versus τ_p^J from which the energy barrier can be extracted, give the same results, i.e. a larger $J_{th,therm}$ and a smaller slope that correspond to a larger energy barrier. As clearly seen from Fig. 5.17c, the slope at $T = 400$ K is smaller than that at $T = 300$ K. Therefore, these results clearly show that the energy barrier for DW injection

from FM to SAF has been increased at the higher temperature (see Fig. 5.17d). This confirms that the thermal effect induces thermal fluctuation fields that strongly trap the DW in the field-induced global energy barrier.

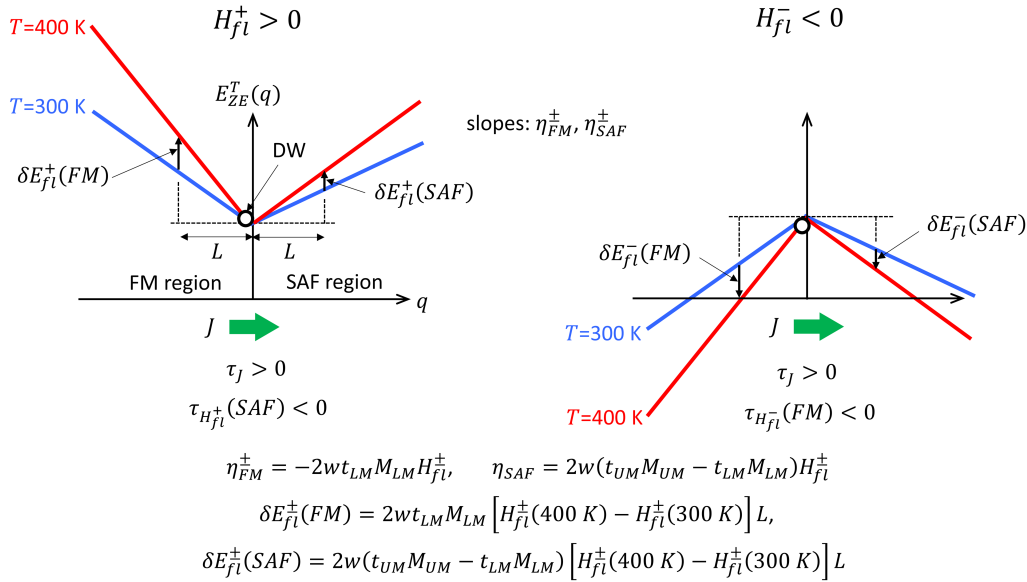


Figure 5.18. Illustration of temperature dependent energy landscapes induced by thermal fluctuation fields H_{fl} . The J induces a torque τ_j along the $+q$ -direction. The DW (white circle) initially sits in the FM-region immediate next to the SAF-FM junction boundary. Two cases H_{fl}^+ (left panel) and H_{fl}^- (right panel) that correspond to positive and negative H_{fl} along the easy z -axis, are considered, respectively. Figure is adopted from [50]

Second, as can be seen from Table 5.1, E_j is nearly constant as a function of T for the FM ($E_j^{FM} \approx 0.73$ eV) and SAF ($E_j^{SAF} \approx 0.79$ eV) cases so that the thermal-induced fields H_{fl} assist in the depinning of the DWs and, correspondingly, a lower $J_{th,therm}$. These results hint that the anisotropy and magnetizations in both FM and SAF are constant as $T = 300 \text{ K} \rightarrow 400 \text{ K}$. For the SAF-FM junction, surprisingly, we find that $E_j^{FM \rightarrow SAF} = 2.5$ eV at $T = 300 \text{ K}$ and $= 5.8$ eV at $T = 400 \text{ K}$, thus leading to an energy barrier increase as the temperature is raised from 300 K to 400 K of $\delta E_j^{FM \rightarrow SAF} = 5.8 - 2.5 = 3.3$ eV.

quantities	FM	SAF	SAF-FM junction
$J_{th,therm} (T=300 \text{ K}) (10^6 \text{ A/cm}^2)$	8.8±1.6 (10 ms)	9.4±1.2 (10 ms)	38±1.1 (10 ms)
$J_{th,therm} (T=400 \text{ K}) (10^6 \text{ A/cm}^2)$	1.5±0.4 (10 ms)	5.1±1.1 (10 ms)	43±0.8 (10 ms)
$\frac{E_J}{k_B T} (T=300 \text{ K})$	29±11.2	32±4.2	100±10.7
$\frac{E_J}{k_B T} (T=400 \text{ K})$	22±2.3	24±4.2	172±43.4
$E_J (T=300 \text{ K}) (\text{eV})$	0.73±0.3	0.8±0.11	2.5±0.27
$E_J (T=400 \text{ K}) (\text{eV})$	0.73±0.08	0.79±0.14	5.8±1.44
$\delta E_J (\text{eV})$	0±0.31	-0.01±0.18	3.3±1.47
$H_{fl}^+ (T=300 \text{ K}) (\text{Oe})$	177	791	791 (SAF region)
$H_{fl}^- (T=300 \text{ K}) (\text{Oe})$	-177	-791	-177 (FM region)
$H_{fl}^+ (T=400 \text{ K}) (\text{Oe})$	204	913	913 (SAF region)
$H_{fl}^- (T=400 \text{ K}) (\text{Oe})$	-204	-913	-204 (FM region)
$\delta H_{fl}^+ (\text{Oe})$	27	122	122 (SAF region)
$\delta H_{fl}^- (\text{Oe})$	-27	-122	-27 (FM region)
$\delta E_{fl}^+ (\text{eV})$	4	0.9	0.9 (SAF region)
$\delta E_{fl}^- (\text{eV})$	-4	-0.9	-4 (FM region)
$\delta E_{fl}^{ave} (\text{eV})$	4	0.9	2.5

Table 5.1. Quantities measured from experiment and estimated from thermal fluctuations for FM, SAF and SAF-FM junction. The upper part (shaded in red) corresponds to the quantities that are experimentally determined from the current-induced DW motion as shown in Fig. 5.17. The errors correspond to one standard deviation in the red part. The lower part (shaded in yellow) corresponds to the quantities that are obtained from our model of thermal fluctuations (see Fig. 5.18). Figure is adopted from [50].

Now let us investigate if this $\delta E_J^{FM \rightarrow SAF}$ quantitatively agrees with the thermal fluctuation field induced global energy barrier landscape. Since H_{fl} points in all directions and its easy-axis z -component only contributes to DW depinning, let us consider two cases for the $\uparrow\downarrow$ DW configuration: H_{fl}^+ (> 0 : $+z$ -direction) and H_{fl}^- (< 0 : $-z$ -direction), as shown in Fig. 5.18. Here the current pulse is applied along the $+q$ -direction such that the current-induced

torque $\tau_J > 0$ always drives the DW along the $+q$ -direction. It is assumed that the fluctuation fields are homogeneous at each instant in time, which we believe is a good approximation to describe DW depinning for the case of the FM-uncompensated SAF junction. Importantly, the sign and magnitude of the global energy landscape slope η as illustrated in Fig. 5.18 (red and blue lines) are determined by H_{fl} and have negative and positive slopes in the FM and SAF regions as follows: $\eta_{FM}^+ < 0$, $\eta_{SAF}^+ > 0$, $\eta_{FM}^- > 0$ and $\eta_{SAF}^- < 0$ (see Fig. 5.18). Note that the DW is sitting in the FM region immediate next to the SAF-FM boundary, and not on the boundary, as shown in Fig. 5.18.

First, let us start to consider H_{fl}^+ case. In this case, H_{fl}^+ results in $\eta_{SAF}^+ > 0$ and $\eta_{FM}^+ < 0$ in the energy landscape that traps a DW in the FM region immediate next to the SAF-FM boundary (see the left panel of Fig. 5.18). Since H_{fl}^+ increases with increasing T , the magnitude of the slope increases with T , thus trapping the DW more tightly and increasing $J_{th,therm}$. Importantly, note that the relevant energy landscape to the DW motion is η_{SAF}^+ since $\tau_J (> 0)$ tries to inject the DW into the SAF region whilst η_{SAF}^+ in the SAF region is against the injection. Consequently, the relevant energy barrier increases $\delta E_{fl}^+(SAF) = 0.9$ eV as $T=300$ K \rightarrow 400 K when the DW trapping range $L \sim 100$ nm is used. Here $L \sim 100$ nm is chosen since it is roughly a mean value of reported pinning potential sizes: e.g. ~ 10 nm [125] and ~ 200 nm [25]. Note that in this calculation it is assumed that the magnetizations do not change as $T = 300$ K \rightarrow 400 K, since the energy barriers in FM and SAF are found to be constant as shown above.

Next, for H_{fl}^- case, H_{fl}^- results in $\eta_{SAF}^- < 0$ and $\eta_{FM}^- > 0$ in the energy landscape that repels a DW away from the FM-SAF junction boundary, as shown in the right panel of Fig. 5.18. Since the DW is initially in the FM region, the relevant energy landscape to the DW motion is η_{FM}^- that tries to move DW along the $-q$ -direction thus competing with τ_J . This shows that H_{fl}^- prevents the injection of a DW into the SAF region just like the H_{fl}^+ case. The relevant energy barrier increase $\delta E_{fl}^-(FM) = 4$ eV as $T=300$ K \rightarrow 400 K when an effective DW range $L \sim 100$ nm roughly (see Fig. 5.18). As seen for the H_{fl}^\pm cases above, both H_{fl}^\pm act to form barriers against DW injection from the FM into the SAF region. Hence, the effective barrier induced by H_{fl}^\pm would be averaged to be $\frac{|\delta E_{fl}^+(SAF)| + |\delta E_{fl}^-(FM)|}{2} = 2.5$ eV, which well agrees with $\delta E_J^{FM \rightarrow SAF} = 3.3 \pm 1.7$ eV obtained from our new experiments, as discussed above. These results thus clearly confirm that the thermal effect is equivalent to a magnetic field in DW

pinning/depinning and that the DWs are highly thermally stable in SAF-FM junctions due to the global energy barrier. These experiments also show that the current-driven DW motion is determined not only by the local energy barrier but by the thermal fluctuation induced global energy barrier for SAF-FM junction.

5.5.4 Extremely high thermal stability of domain wall in SAF-FM-SAF bi-junctions

We showed that a DW is highly stable against thermal fluctuation near the boundary of the FM region in a SAF-FM junction when an external magnetic field H_z is applied (Fig. 5.19) (note that the SAF region is on the right-hand side of the junction). For example, when a $\uparrow\downarrow$ DW is sitting somewhere in the FM region and the neighbouring SAF layer has the configuration: upper layer: \uparrow and lower layer: \downarrow , a positive H_z results in the slope of the DW energy versus x , the distance along the junction, to be negative in the FM region but positive in the SAF region (top panel in Fig. 5.19). This drives the DW towards the junction boundary but the DW remains on the FM side of the junction.

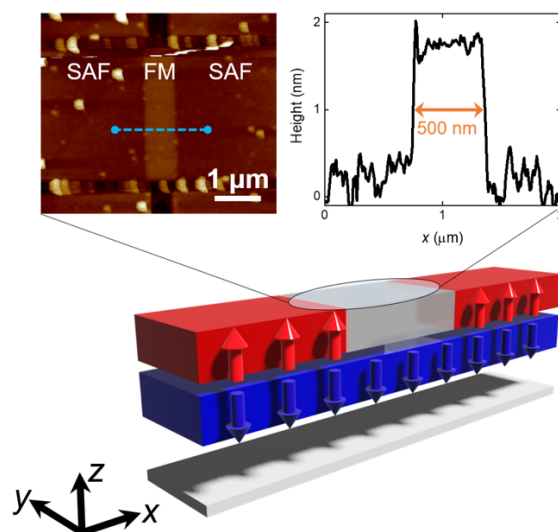


Figure 5.19. SAF-FM-SAF lateral bi-junctions. AFM image and schematic illustration of SAF-FM-SAF bi-junction integrated to racetrack nanowire. The height profile across the junctions formed with the width of FM region ~ 500 nm which is sandwiched between two SAF regions are measured (blue dashed line). Figure is adopted from [50].

On the other hand, when the field direction is reversed the DW moves away from the junction into the FM region, as illustrated in the bottom panel in Fig. 5.19. This indicates that the high thermal stability of DWs cannot be guaranteed by bi-polar external field, but only be limited by one direction. Since the thermal induced field fluctuation is random, this is critical

handicap for integrating SAF-FM junction into racetrack memory device. Thus, we devise a simple but highly effective approach to overcome this issue. In order to trap the DW for both positive and negative fields, we create a second junction with a second SAF region on the leftmost side of the FM region thereby forming a SAF-FM-SAF bi-junction (see Fig. 5.20a). As shown in Fig. 5.20a, experiments confirm that the DW is now firmly trapped within the FM region for $|H_z| < 3$ kOe. Once a single DW is located in the FM region, the configurations of the two SAF regions are opposite to each other. Therefore, the slopes of the energy landscape at the SAF-FM (left hand side) and FM-SAF (right hand side) junctions are tilted in opposite directions in response to external fields with opposite signs (see Fig. 5.20b). This gives rise to a strong confinement of the DW within the FM region. It is expected that this region can be shrunk to as little as the DW width whilst the trapping strength remains unchanged, so allowing for high density devices. This is because the domains are magnetically structureless while the region within the DW width only has magnetic gradients so that the device would function nearly independent of the length of the FM region till it reaches the DW width.

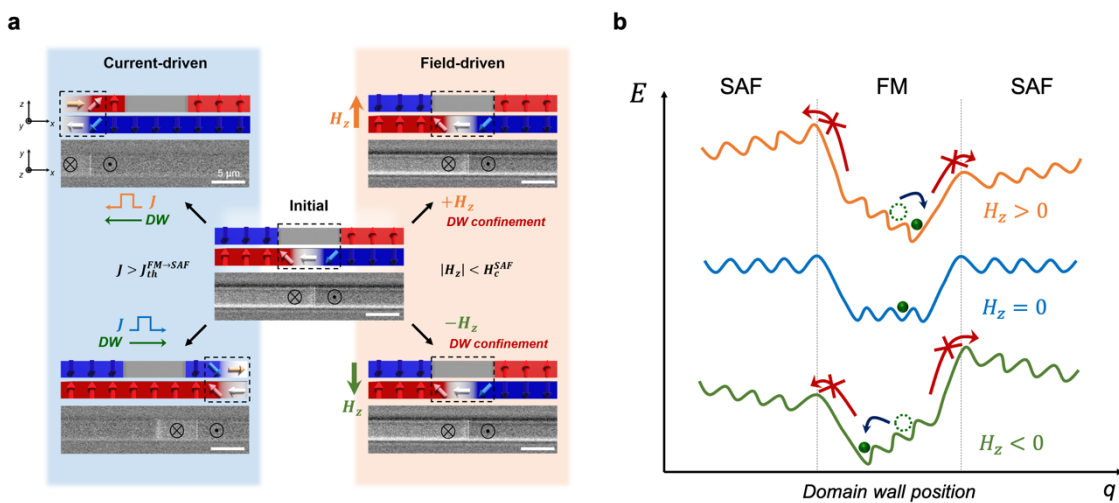


Figure 5.20. Demonstration of field stability of SAF-FM-SAF lateral bi-junction. a, b, Schematics and Kerr microscope images of current- and field-induced DW motion within a SAF-FM-SAF bi-junction (FM region width: 500 nm) **(a)** and corresponding DW energy landscape versus position for various H_z ($= 0$: middle panel, > 0 : top panel, < 0 : bottom panel) **(b)**. Figure is adopted from [50]

Chapter 6 Conclusion and perspectives

In this thesis, we presented a novel approach to overcome the trade-off between thermal stability and energy efficiency of chiral DW based devices that is one of the long-standing major challenges for DW-based electronic devices, such as racetrack memory. Our approach introduces the new concept of a SAF-FM lateral junction, which can be readily fabricated by conventional lithographic techniques and local oxygen plasma processing of conventional SAF racetrack nanowires. We discovered that the oxidation through the surface of the multilayered SAF structure gradually transforms the SAF into a FM. The magnetic properties, such as magnetization and anisotropy field, between oxidized SAF and pristine FM are found to be nearly identical by magnetic hysteresis measurements. In addition, a XPS depth-profile analysis confirms that the oxidation is only limited to the upper layer of SAF due to the thin Ru spacer which plays the role of a passivation layer, thereby preserving the magnetic properties of the lower FM layer of the SAF. The junction boundary was characterized by scanning AFM and cross-section TEM that directly shows a sharp transition region at the junction boundary which is comparable with a typical Néel DW width in either the FM or the SAF.

Studies of the current-induced DW motion was performed in FM, SAF, and SAF-FM lateral junctions, respectively, with various input current pulse durations to compare the distinct DW depinning mechanisms in the flow and the thermally activated regimes. We found that the threshold current density for DW motion in a FM is larger than that in a SAF in the flow regime, whilst it is opposite in the thermally activated regime. Based on measurements of the threshold current density in the thermally activated regime, the DW depinning energy barrier in the SAF was found to be larger than that of a FM. This result clearly corresponds to the aforementioned inversion of threshold current density in the flow and thermally activated regimes as well. In addition, field-induced DW depinning studies in FM and SAF devices were also carried out in the thermally activated regime to evaluate the DW depinning energy barriers in a similar manner as the current induced depinning cases. As reported in previous studies [39], [40], the current- and field-induced DW depinning in a FM is governed by the same energy barrier, thus resulting $E_J^{FM} \approx E_H^{FM}$, whereas for the SAF case $E_J^{SAF} > E_H^{SAF}$. The origin of this discrepancy

between E_j^{SAF} and E_H^{SAF} is not clear, but further experiments, for example by varying the degree of compensation of the SAF will help to understand the underlying mechanism in the future.

We also found that the threshold current density for DW injection across the junction from the FM to the SAF region is larger than that of the FM and SAF. Interestingly, the DW injection appeared to be asymmetric in which the DW injection from SAF to FM takes place with less threshold current density than for the opposite case ($J_{th}^{FM \rightarrow SAF} > J_{th}^{SAF \rightarrow FM}$). This diode-like behavior is due to the asymmetric local energy barrier, which originates from the nucleation energy of the DW in the UM of the SAF. The magnitude of the nucleation energy corresponds to the volume of the DW in the UM which can be reduced by tailoring the shape of the junction. By tilting the junction angle θ_j , we showed that the DW injection threshold current density is significantly reduced thereby reducing the nucleation energy by a factor of four as θ_j increases from 0° to 60° . In addition, we showed that this efficiency of current-induced motion is more significant in the short pulse regime which is technologically more useful to the development of high-speed devices.

Most surprisingly, the field-induced DW injection from a FM to a SAF was found to be nearly impossible, so that the DW is trapped at the junction boundary regardless of the shape of the junctions. This indicates that the field-stability of SAF-FM junction is extremely high, whilst DWs can be efficiently moved by currents. We discovered that this unconventional field-stability is due to tilting of the field-induced energy landscape of SAF, namely a global energy barrier. As the field is applied to move the DW forwards to the junction, the sign of the tilting of the energy landscape of FM and SAF is opposite so that the DW is tightly bound near the junction boundary. This is possible by designing the SAF where the moment in the UM is slightly larger than that of the LM. These findings gave us a hint of achieving high thermal stability of a DW at such a junction.

In this respect, we further carried out temperature-dependent current-induced DW injection experiments at $T = 300\text{ K}$, and 400 K to clearly prove that thermal fluctuation effects indeed give rise to corresponding fluctuating magnetic fields. Remarkably, moreover, we showed from these experiments that the global energy barrier indeed increases significantly with increasing temperature at the junction. Consequently, this results in an increase of the DW injection energy barrier at $T = 400\text{ K}$ compared to those at $T = 300\text{ K}$ which is in sharp contrast to the FM and SAF cases. We also quantitatively verified that the increase of the energy barrier obtained from our experiments agrees well with the effective energy barrier

induced by thermal fluctuation fields as $T = 300 \rightarrow 400$ K. It is noteworthy that these results not only prove the high thermal stability of the junction but also clearly reveal that the thermal effect is equivalent to the field effect rather than the current effect in magnetic systems. By taking advantage of this approach, we expect to further evaluate the thermal stability of various DW-based devices with magnetic field-induced experiments as well.

Beyond the single SAF-FM junction, we demonstrated that DWs located in the FM region of a SAF-FM-SAF lateral bi-junction can be tightly bound and are extremely thermally stable. In contrast to the single junction, the randomly oriented large external fields cannot depin the DWs from the FM region which is sandwiched on both sides by SAF regions. On the other hand, the DWs can be efficiently injected into the SAF regions across the junction in both direction depending upon the applied current direction.

In summary, here we take advantage of the locality of current-induced SOT and the globality of the field-induced energy landscape: the current-induced SOT depins a DW by overcoming a local energy barrier but, on the other hand, an applied field globally tilts the energy landscape. This thereby allows for a novel SAF-FM-SAF lateral bi-junction to induce a global energy well that tightly traps DWs.

In the future, our work will allow for the development of highly reliable DW-based spintronics. Particularly, densely packed SAF-FM-SAF lateral bi-junctions within a racetrack can be used for a multi-bit DW racetrack memory platform with high thermal stability that could potentially replace today's memory technologies. Moreover, FM-SAF-FM junction structures can also be an excellent platform for single-bit DW racetrack memory which is analogy to field-free SOT-MRAM, thereby promising a memory technology with low energy consumption. Furthermore, SAF-FM junctions can also be potentially useful for various applications such as logic [9], neuromorphic devices [129], [130], and DW oscillators [131]. By forming a SAF-FM junction in DW logic, for instance, the synchronization and propagation of two input DWs can be more precisely controlled, so that we expect to minimize output errors. Of course, there are still challenges that need to be addressed before commercialization, such as the high resistance of the racetrack channel and the enabling of the sensitive electrical detection of DWs in very narrow racetracks. However, in the near future, these issues will likely be resolved based on recent substantial progress in the integration of MTJs within conventional racetrack [132]. In conclusion, we are confident that our work will influence

Chapter 6

future research on DW-based spintronics to deliver commercial products within the next decade.

Appendix A

A.1 Deterministic multi-DW injection

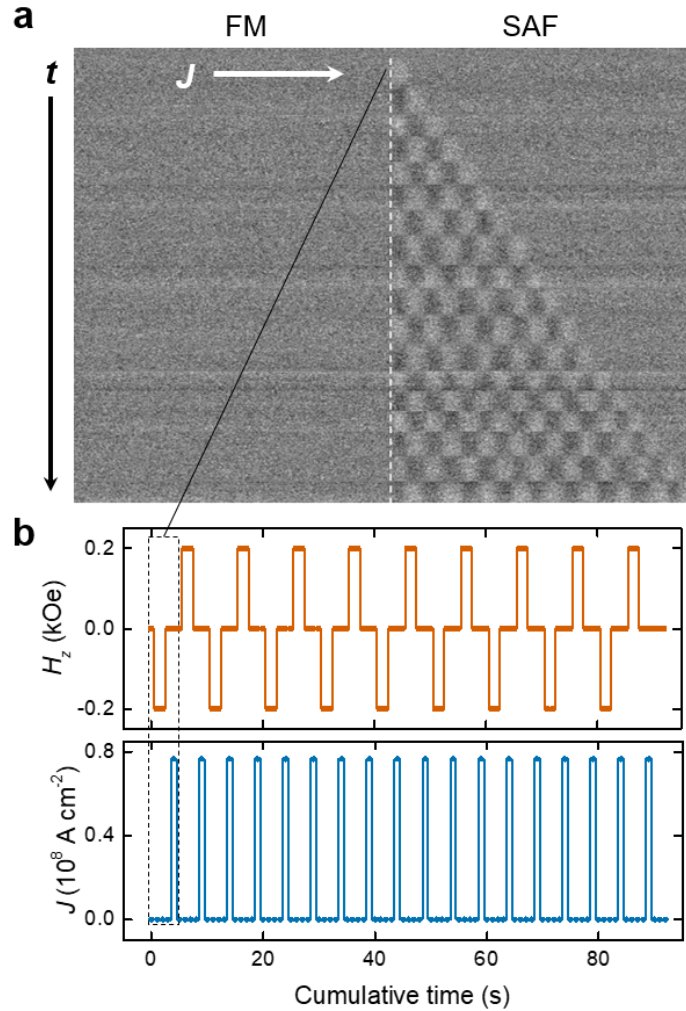


Figure A1. Sequential DW initialization and multi-bit injection from the FM into the SAF region in a racetrack. **a**, Sequential Kerr microscopy images of injection of eighteen DWs from the FM region into the SAF region. The racetrack is 3 μm wide and 40 μm long. The FM-SAF junction with $\theta_j = 0^\circ$ is designated by the white dashed line. Each Kerr image is taken after a combination of field and current pulse applications. Bright and dark contrast correspond to down (\downarrow) and up (\uparrow) domains, respectively. **b**, Cycles of field and current pulses versus cumulative time corresponding to Kerr images in (a). Each cycle is denoted by the black dashed line, which is repeated eighteen times. Figure is adopted from [50].

Appendix

By taking advantage of the large difference in coercivity and spin-flop field between the FM and SAF regions, DWs can be readily and reliably created by applying an external field. The field $|H_z|$ is chosen to be $|H_c^{FM}| (\approx 0.1 \text{ kOe}) < |H_z| < |H_{sf}^{SAF}| (\approx 3 \text{ kOe})$ such that a DW is nucleated in the FM region. The created DW is injected into the SAF region by current pulses. By repeating the DW nucleation and injection cycle, we demonstrated multi-DW injection, as shown in Fig. S11a. Each cycle for DW injection consists of a field pulse of ± 20 mT for 2 sec and a current pulse of $0.76 \times 10^8 \text{ A cm}^{-2}$ for 10 ns (see Fig. A1b). An external field is set to zero when the current pulse is applied. Consequently, eighteen DWs can be successfully injected with wall-to-wall distances of $\sim 1.4 \text{ }\mu\text{m}$. The domain bit sizes can be modulated by the amplitude and length of the current pulse.

A.2 Determination of DW injection across the SAF-FM junction

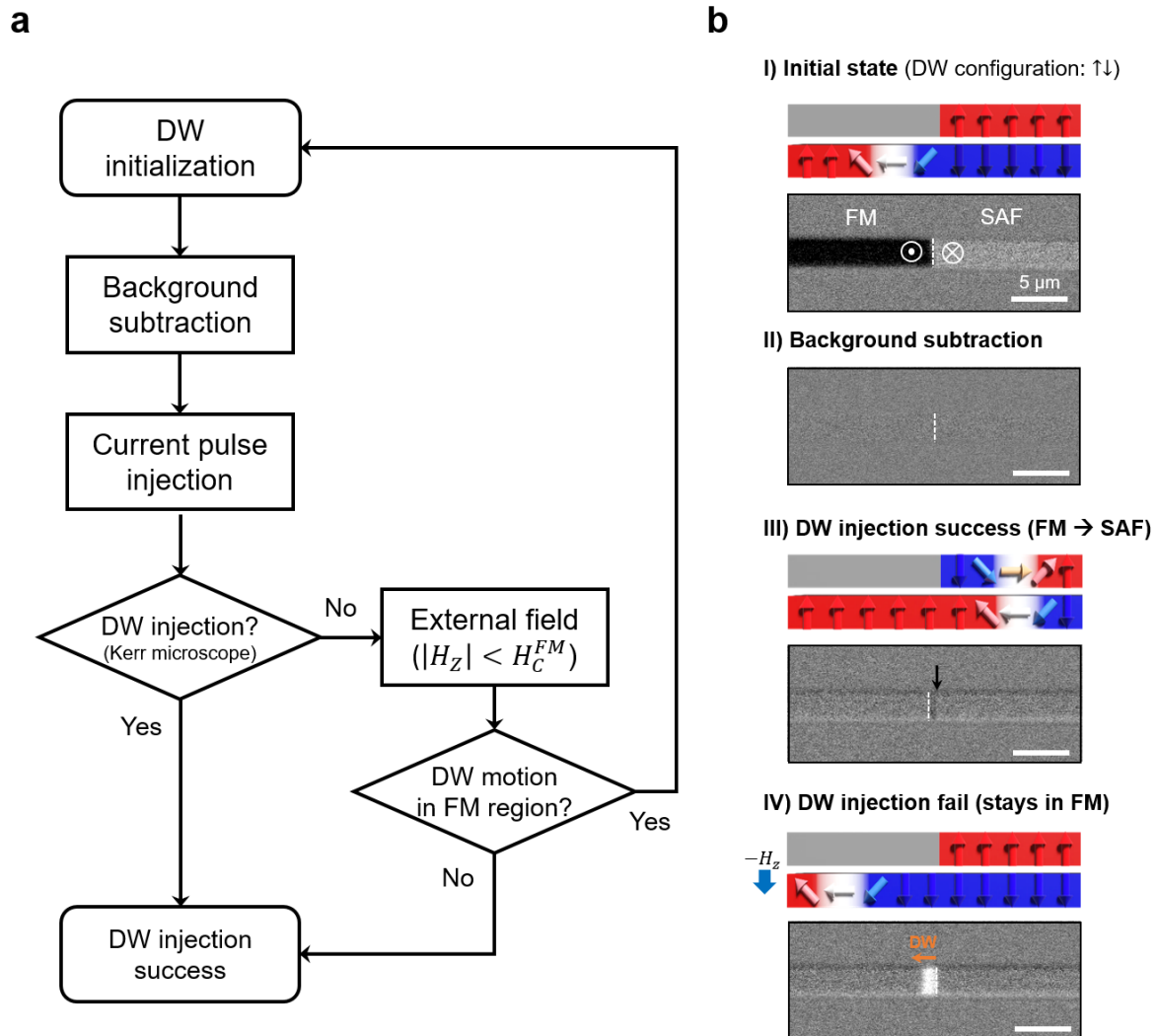


Figure A2. Determination procedure of DW injection across a FM-SAF junction. A, Logic flow diagram of determination procedure of DW injection from FM to SAF region across junction by current pulse. **B,** Schematics and corresponding Kerr microscope images of DW injection procedure. White dashed lines represent the FM-SAF junction, and black arrows indicate the DW injected into the SAF region. Figure is adopted from [50].

The optical resolution of a Kerr microscope limits the confirmation of DW injection across the interface. Fortunately, our FM-SAF junctions with their novel magnetic configuration by design allows us to carry out extremely precise and reliable confirmation of DW injection across the interfaces by combining Kerr microscopy with the application of easy axis magnetic fields that are larger than the DW propagation fields, as follows. Here let us take a $\uparrow\downarrow$ DW at the FM-SAF junction in which the FM and the SAF regions are on the left and right-hand side, respectively.

- a. When the DW is observed to be clearly injected across the interface from Kerr microscope, we are sure that the DW is injected since the DW has been displaced by more than the Kerr microscope resolution.
- b. When the DW is observed not to be injected by current pulse from Kerr microscope, an easy axis magnetic field is applied to check if the DW is actually injected across the interface. First, let us consider a DW that is initially in the FM region at the FM-SAF junction. If the DW was successfully injected across the interface so that it moves to the SAF region, the application of a negative H_z ($-H_z < 0.4$ kOe: propagation field in the SAF region) would move the DW from the left to the right since the total DW configuration in the SAF region is $\downarrow\uparrow$ (Note that the upper layer moment is larger than the lower layer). On the other hand, if the DW fails to be injected so that it still sits in the FM region, a negative H_z ($-H_z < 30$ Oe: propagation field in the FM region) would move the DW from the right to the left. Consequently, the DW moving direction by a negative H_z is opposite depending on whether the DW is successfully injected across the interface or not, from which we can rigorously judge the DW injection. Since the propagation field in the SAF region (~ 0.4 kOe) is significantly larger than the FM region (~ 30 Oe), the application of H_z in-between two propagation fields, i.e., $30 \text{ Oe} < -H_z < 0.4 \text{ kOe}$ can also tell whether the DW is injected across the interface. Fig. A2 describes this method to judge the DW injection across the interface.
- c. The same protocol as above can be applied to the case that the DW is injected from the SAF into the FM region.

A.3 Evaluation of pulsed magnetic fields

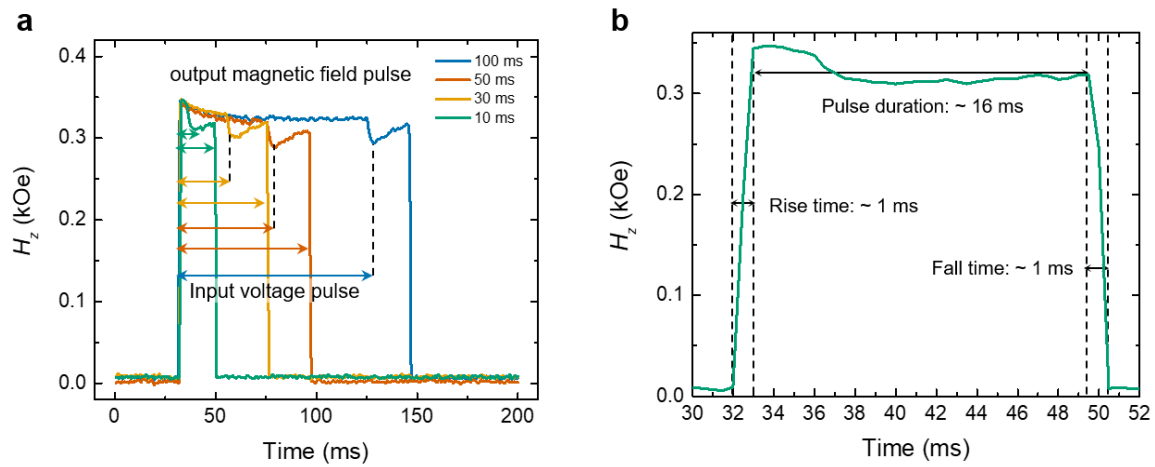


Figure A3. Profiles of pulsed magnetic fields measured by Hall probe. a, Measured magnetic field pulses with a magnitude of $H_z \sim 0.35$ kOe and corresponding input voltage pulse duration from 10 to 100 ms. Black dashed lines and arrows correspond to the applied pulse duration, respectively. **b,** Shape of single pulse magnetic field with 10 ms duration. Figure is adopted from [50].

Thermally assisted field-driven DW motion in FM and SAF regions were performed by applying single pulsed magnetic fields along the magnetic easy axis with a broad range of pulse durations τ_p^H from 10 ms to 5 s. Single pulses of magnetic field are generated by an Evico electromagnetic inductor coil combined with a Kepco bipolar BOP 100-4D power supply and a Keithley 2400 pulse generator.

To evaluate the shape of the magnetic field pulse, a Hall probe sensor combined with a digital oscilloscope were employed to measure the pulse shape resulting from the Hall voltage in response to the magnetic field changes. As shown in Fig. S10a, the shape of the field pulses with different pulse lengths exhibits a rise and fall time, each of ~ 1 ms, and a pulse duration corresponding to the nominal input voltage pulse length of from 10 to 100 ms (see arrows). Contrary to the nominal input pulse length, the actual magnetic field pulse length is slightly longer. For instance, the 10 ms nominal pulse length has a measured length of ~ 16 ms, as shown in Fig. A3.

Bibliography

- [1] A. Hubert and R. Schäfer, *Magnetic Domains: The Analysis of Magnetic Microstructures*. 1998.
- [2] S. S. P. Parkin, M. Hayashi, and L. Thomas, ‘Magnetic Domain-Wall Racetrack Memory’. [Online]. Available: <https://www.science.org>
- [3] S. Parkin and S. H. Yang, ‘Memory on the racetrack’, *Nature Nanotechnology*, vol. 10, no. 3. Nature Publishing Group, pp. 195–198, Mar. 05, 2015. doi: 10.1038/nnano.2015.41.
- [4] D. A. Allwood, G. Xiong, C. C. Faulkner, D. Atkinson, D. Petit, and R. P. Cowburn, ‘Magnetic Domain-Wall Logic’. [Online]. Available: <https://www.science.org>
- [5] A. P. Malozemoff, J. C. Slonczewski, Y. London, T. Sydney, and S. Francisco, ‘Magnetic Domain Walls in Bubble Materials ACADEMIC PRESS New’.
- [6] K. S. Ryu, L. Thomas, S. H. Yang, and S. Parkin, ‘Chiral spin torque at magnetic domain walls’, *Nat Nanotechnol*, vol. 8, no. 7, pp. 527–533, 2013, doi: 10.1038/nnano.2013.102.
- [7] S. Emori, U. Bauer, S. M. Ahn, E. Martinez, and G. S. D. Beach, ‘Current-driven dynamics of chiral ferromagnetic domain walls’, *Nat Mater*, vol. 12, no. 7, pp. 611–616, Jul. 2013, doi: 10.1038/nmat3675.
- [8] S. H. Yang, K. S. Ryu, and S. Parkin, ‘Domain-wall velocities of up to 750 m s⁻¹ driven by exchange-coupling torque in synthetic antiferromagnets’, *Nat Nanotechnol*, vol. 10, no. 3, pp. 221–226, Mar. 2015, doi: 10.1038/nnano.2014.324.
- [9] Z. Luo *et al.*, ‘Current-driven magnetic domain-wall logic’, *Nature*, vol. 579, no. 7798, pp. 214–218, Mar. 2020, doi: 10.1038/s41586-020-2061-y.
- [10] S. H. Yang, R. Naaman, Y. Paltiel, and S. S. P. Parkin, ‘Chiral spintronics’, *Nature Reviews Physics*, vol. 3, no. 5. Springer Nature, pp. 328–343, May 01, 2021. doi: 10.1038/s42254-021-00302-9.
- [11] D. A. Allwood *et al.*, ‘Submicrometer Ferromagnetic NOT Gate and Shift Register’, 1995. [Online]. Available: www.sciencemag.org/cgi/content/full/296/5575/1999/DC1
- [12] R. Blasing *et al.*, ‘Magnetic Racetrack Memory: From Physics to the Cusp of Applications within a Decade’, *Proceedings of the IEEE*, vol. 108, no. 8, pp. 1303–1321, Aug. 2020, doi: 10.1109/JPROC.2020.2975719.
- [13] ‘US20050078509A1’.

Bibliography

- [14] M. Hayashi, L. Thomas, R. Moriya, C. Rettner, and S. S. P. Parkin, ‘Current-Controlled Magnetic Domain-Wall Nanowire Shift Register’, *Science (1979)*, vol. 320, no. 5873, pp. 209–211, Apr. 2008, doi: 10.1126/science.1154587.
- [15] M. Hayashi, L. Thomas, C. Rettner, R. Moriya, Y. B. Bazaliy, and S. S. P. Parkin, ‘Current Driven Domain Wall Velocities Exceeding the Spin Angular Momentum Transfer Rate in Permalloy Nanowires’, *Phys Rev Lett*, vol. 98, no. 3, p. 037204, Jan. 2007, doi: 10.1103/PhysRevLett.98.037204.
- [16] J. C. Slonczewski, ‘~H journal of magnetism and magnetic ~H materials Current-driven excitation of magnetic multilayers’, 1996.
- [17] L. Berger, ‘Exchange interaction between ferromagnetic domain wall and electric current in very thin metallic films’, *J Appl Phys*, vol. 55, no. 6, pp. 1954–1956, Mar. 1984, doi: 10.1063/1.333530.
- [18] L. Berger, ‘Motion of a magnetic domain wall traversed by fast-rising current pulses’, *J Appl Phys*, vol. 71, no. 6, pp. 2721–2726, Mar. 1992, doi: 10.1063/1.351045.
- [19] V. Vlaminck and M. Bailleul, ‘Current-Induced Spin-Wave Doppler Shift’, *Science (1979)*, vol. 322, no. 5900, pp. 410–413, Oct. 2008, doi: 10.1126/science.1162843.
- [20] G. H. O. Daalderop, P. J. Kelly, and F. J. A. den Broeder, ‘Prediction and confirmation of perpendicular magnetic anisotropy in Co/Ni multilayers’, *Phys Rev Lett*, vol. 68, no. 5, pp. 682–685, Feb. 1992, doi: 10.1103/PhysRevLett.68.682.
- [21] D. Weller, Y. Wu, J. Stöhr, M. G. Samant, B. D. Hermsmeier, and C. Chappert, ‘Orbital magnetic moments of Co in multilayers with perpendicular magnetic anisotropy’, *Phys Rev B*, vol. 49, no. 18, pp. 12888–12896, May 1994, doi: 10.1103/PhysRevB.49.12888.
- [22] D. Chiba *et al.*, ‘Control of Multiple Magnetic Domain Walls by Current in a Co/Ni Nano-Wire’, *Applied Physics Express*, vol. 3, no. 7, p. 073004, Jul. 2010, doi: 10.1143/APEX.3.073004.
- [23] L. Thomas *et al.*, ‘Racetrack Memory: A high-performance, low-cost, non-volatile memory based on magnetic domain walls’, in *2011 International Electron Devices Meeting*, IEEE, Dec. 2011, pp. 24.2.1-24.2.4. doi: 10.1109/IEDM.2011.6131603.
- [24] I. M. Miron *et al.*, ‘Fast current-induced domain-wall motion controlled by the Rashba effect’, *Nat Mater*, vol. 10, no. 6, pp. 419–423, Jun. 2011, doi: 10.1038/nmat3020.
- [25] K. S. Ryu, S. H. Yang, L. Thomas, and S. S. P. Parkin, ‘Chiral spin torque arising from proximity-induced magnetization’, *Nat Commun*, vol. 5, no. May, pp. 1–8, 2014, doi: 10.1038/ncomms4910.

Bibliography

- [26] T. Moriya, ‘Anisotropic Superexchange Interaction and Weak Ferromagnetism’, *Physical Review*, vol. 120, no. 1, pp. 91–98, Oct. 1960, doi: 10.1103/PhysRev.120.91.
- [27] I. Dzyaloshinsky, ‘A thermodynamic theory of “weak” ferromagnetism of antiferromagnetics’, *Journal of Physics and Chemistry of Solids*, vol. 4, no. 4, pp. 241–255, Jan. 1958, doi: 10.1016/0022-3697(58)90076-3.
- [28] S. Meckler, N. Mikuszeit, A. Preßler, E. Y. Vedmedenko, O. Pietzsch, and R. Wiesendanger, ‘Real-Space Observation of a Right-Rotating Inhomogeneous Cycloidal Spin Spiral by Spin-Polarized Scanning Tunneling Microscopy in a Triple Axes Vector Magnet’, *Phys Rev Lett*, vol. 103, no. 15, p. 157201, Oct. 2009, doi: 10.1103/PhysRevLett.103.157201.
- [29] I. M. Miron *et al.*, ‘Perpendicular switching of a single ferromagnetic layer induced by in-plane current injection’, *Nature*, vol. 476, no. 7359, pp. 189–193, 2011, doi: 10.1038/nature10309.
- [30] L. Liu, O. J. Lee, T. J. Gudmundsen, D. C. Ralph, and R. A. Buhrman, ‘Current-Induced Switching of Perpendicularly Magnetized Magnetic Layers Using Spin Torque from the Spin Hall Effect’, *Phys Rev Lett*, vol. 109, no. 9, p. 096602, Aug. 2012, doi: 10.1103/PhysRevLett.109.096602.
- [31] J. E. Hirsch, ‘Spin Hall Effect’, *Phys Rev Lett*, vol. 83, no. 9, pp. 1834–1837, Aug. 1999, doi: 10.1103/PhysRevLett.83.1834.
- [32] A. Thiaville, S. Rohart, É. Jué, V. Cros, and A. Fert, ‘Dynamics of Dzyaloshinskii domain walls in ultrathin magnetic films’, *EPL (Europhysics Letters)*, vol. 100, no. 5, p. 57002, Dec. 2012, doi: 10.1209/0295-5075/100/57002.
- [33] S. S. P. Parkin, N. More, and K. P. Roche, ‘Oscillations in exchange coupling and magnetoresistance in metallic superlattice structures: Co/Ru, Co/Cr, and Fe/Cr’, *Phys Rev Lett*, vol. 64, no. 19, pp. 2304–2307, May 1990, doi: 10.1103/PhysRevLett.64.2304.
- [34] S. S. P. Parkin, ‘Systematic variation of the strength and oscillation period of indirect magnetic exchange coupling through the 3 *d*, 4 *d*, and 5 *d* transition metals’, *Phys Rev Lett*, vol. 67, no. 25, pp. 3598–3601, Dec. 1991, doi: 10.1103/PhysRevLett.67.3598.
- [35] S. Parkin, Xin Jiang, C. Kaiser, A. Panchula, K. Roche, and M. Samant, ‘Magnetically engineered spintronic sensors and memory’, *Proceedings of the IEEE*, vol. 91, no. 5, pp. 661–680, May 2003, doi: 10.1109/JPROC.2003.811807.

Bibliography

- [36] R. Bläsing *et al.*, ‘Exchange coupling torque in ferrimagnetic Co/Gd bilayer maximized near angular momentum compensation temperature’, *Nat Commun*, vol. 9, no. 1, 2018, doi: 10.1038/s41467-018-07373-w.
- [37] S. Fukami, T. Suzuki, K. Nagahara, N. Ohshima, and N. Ishiwata, ‘Large thermal stability independent of critical current of domain wall motion in Co/Ni nanowires with step pinning sites’, *J Appl Phys*, vol. 108, no. 11, p. 113914, Dec. 2010, doi: 10.1063/1.3518046.
- [38] K.-J. Kim *et al.*, ‘Tradeoff between low-power operation and thermal stability in magnetic domain-wall-motion devices driven by spin Hall torque’, *Applied Physics Express*, vol. 7, no. 5, p. 053003, May 2014, doi: 10.7567/APEX.7.053003.
- [39] K.-J. Kim *et al.*, ‘Two-barrier stability that allows low-power operation in current-induced domain-wall motion’, *Nat Commun*, vol. 4, no. 1, p. 2011, Jun. 2013, doi: 10.1038/ncomms3011.
- [40] S. Fukami, J. Ieda, and H. Ohno, ‘Thermal stability of a magnetic domain wall in nanowires’, *Phys Rev B*, vol. 91, no. 23, p. 235401, Jun. 2015, doi: 10.1103/PhysRevB.91.235401.
- [41] K. W. Kim and H. W. Lee, ‘Thermal fluctuation field for current-induced domain wall motion’, *Phys Rev B Condens Matter Mater Phys*, vol. 82, no. 13, Oct. 2010, doi: 10.1103/PhysRevB.82.134431.
- [42] D. Lacour, J. A. Katine, N. Smith, M. J. Carey, and J. R. Childress, ‘Thermal effects on the magnetic-field dependence of spin-transfer-induced magnetization reversal’, *Appl Phys Lett*, vol. 85, no. 20, pp. 4681–4683, Nov. 2004, doi: 10.1063/1.1819516.
- [43] R. H. Koch, J. A. Katine, and J. Z. Sun, ‘Time-Resolved Reversal of Spin-Transfer Switching in a Nanomagnet’, *Phys Rev Lett*, vol. 92, no. 8, p. 088302, Feb. 2004, doi: 10.1103/PhysRevLett.92.088302.
- [44] S. Ikeda *et al.*, ‘Magnetic Tunnel Junctions for Spintronic Memories and Beyond’, *IEEE Trans Electron Devices*, vol. 54, no. 5, pp. 991–1002, May 2007, doi: 10.1109/TED.2007.894617.
- [45] S. Ikeda *et al.*, ‘Tunnel magnetoresistance of 604% at 300 K by suppression of Ta diffusion in CoFeBMgOCoFeB pseudo-spin-valves annealed at high temperature’, *Appl Phys Lett*, vol. 93, no. 8, pp. 17–20, 2008, doi: 10.1063/1.2976435.
- [46] S. Ikeda *et al.*, ‘A perpendicular-anisotropy CoFeB-MgO magnetic tunnel junction’, *Nat Mater*, vol. 9, no. 9, pp. 721–724, 2010, doi: 10.1038/nmat2804.

Bibliography

- [47] A. V Khvalkovskiy *et al.*, ‘Basic principles of STT-MRAM cell operation in memory arrays’, *J Phys D Appl Phys*, vol. 46, no. 7, p. 074001, Feb. 2013, doi: 10.1088/0022-3727/46/7/074001.
- [48] J. Torrejon *et al.*, ‘Interface control of the magnetic chirality in CoFeB/MgO heterostructures with heavy-metal underlayers’, *Nat Commun*, vol. 5, no. 1, p. 4655, Aug. 2014, doi: 10.1038/ncomms5655.
- [49] T. Koyama *et al.*, ‘Observation of the intrinsic pinning of a magnetic domain wall in a ferromagnetic nanowire’, *Nat Mater*, vol. 10, no. 3, pp. 194–197, 2011, doi: 10.1038/nmat2961.
- [50] J. Yoon *et al.*, ‘Local and global energy barriers for chiral domain walls in synthetic antiferromagnet–ferromagnet lateral junctions’, *Nat Nanotechnol*, vol. 17, no. 11, pp. 1183–1191, Nov. 2022, doi: 10.1038/s41565-022-01215-z.
- [51] P. Frank and R. Wood, ‘A Perspective on the Future of Hard Disk Drive (HDD) Technology’, in *Asia-Pacific Magnetic Recording Conference 2006*, IEEE, Nov. 2006, pp. 1–2. doi: 10.1109/APMRC.2006.365887.
- [52] ‘Hard Disk Drive Servo Systems, 2nd edition (Chen, B.M. et al.; 2006)’, *IEEE Control Syst*, vol. 28, no. 3, pp. 80–81, Jun. 2008, doi: 10.1109/MCS.2008.920444.
- [53] T. M. Coughlin, ‘Fundamentals of Hard Disk Drives’, in *Digital Storage in Consumer Electronics*, Cham: Springer International Publishing, 2018, pp. 25–44. doi: 10.1007/978-3-319-69907-3_2.
- [54] W. Heisenberg, ‘Mehrkörperproblem und Resonanz in der Quantenmechanik’, *Zeitschrift für Physik*, vol. 38, no. 6–7, pp. 411–426, Jun. 1926, doi: 10.1007/BF01397160.
- [55] P. Dirac, ‘On the theory of quantum mechanics’, *Proceedings of the Royal Society of London. Series A, Containing Papers of a Mathematical and Physical Character*, vol. 112, no. 762, pp. 661–677, Oct. 1926, doi: 10.1098/rspa.1926.0133.
- [56] Charles Kittel, *Introduction to Solid State Physics*, 8th ed. Wiley, 2004.
- [57] J. M. D. Coey, *Magnetism and Magnetic Materials*. Cambridge University Press, 2001. doi: 10.1017/CBO9780511845000.
- [58] O. Boulle *et al.*, ‘Domain Wall Tilting in the Presence of the Dzyaloshinskii-Moriya Interaction in Out-of-Plane Magnetized Magnetic Nanotracks’, *Phys Rev Lett*, vol. 111, no. 21, p. 217203, Nov. 2013, doi: 10.1103/PhysRevLett.111.217203.

Bibliography

- [59] S. H. Yang and S. Parkin, ‘Novel domain wall dynamics in synthetic antiferromagnets’, *Journal of Physics Condensed Matter*, vol. 29, no. 30, 2017, doi: 10.1088/1361-648X/aa752d.
- [60] A. Thiaville, J. M. García, and J. Miltat, ‘Domain wall dynamics in nanowires’, *J Magn Magn Mater*, vol. 242–245, pp. 1061–1063, Apr. 2002, doi: 10.1016/S0304-8853(01)01353-1.
- [61] S.-H. Yang, C. Garg, and S. S. P. Parkin, ‘Chiral exchange drag and chirality oscillations in synthetic antiferromagnets’, *Nat Phys*, vol. 15, no. 6, pp. 543–548, Jun. 2019, doi: 10.1038/s41567-019-0438-3.
- [62] F. Keffer, ‘Moriya Interaction and the Problem of the Spin Arrangements in $\beta\text{-MnS}$ ’, *Physical Review*, vol. 126, no. 3, pp. 896–900, May 1962, doi: 10.1103/PhysRev.126.896.
- [63] N. S. Gusev, A. V. Sadovnikov, S. A. Nikitov, M. V. Sapozhnikov, and O. G. Udalov, ‘Manipulation of the Dzyaloshinskii–Moriya Interaction in Co/Pt Multilayers with Strain’, *Phys Rev Lett*, vol. 124, no. 15, p. 157202, Apr. 2020, doi: 10.1103/PhysRevLett.124.157202.
- [64] A. N. Bogdanov and U. K. Röbber, ‘Chiral Symmetry Breaking in Magnetic Thin Films and Multilayers’, *Phys Rev Lett*, vol. 87, no. 3, p. 037203, Jun. 2001, doi: 10.1103/PhysRevLett.87.037203.
- [65] M. Heide, G. Bihlmayer, and S. Blügel, ‘Dzyaloshinskii-Moriya interaction accounting for the orientation of magnetic domains in ultrathin films: Fe/W(110)’, *Phys Rev B*, vol. 78, no. 14, p. 140403, Oct. 2008, doi: 10.1103/PhysRevB.78.140403.
- [66] A. V. Khvalkovskiy *et al.*, ‘Matching domain-wall configuration and spin-orbit torques for efficient domain-wall motion’, *Phys Rev B*, vol. 87, no. 2, p. 020402, Jan. 2013, doi: 10.1103/PhysRevB.87.020402.
- [67] K.-U. Demasius *et al.*, ‘Enhanced spin–orbit torques by oxygen incorporation in tungsten films’, *Nat Commun*, vol. 7, no. 1, p. 10644, Feb. 2016, doi: 10.1038/ncomms10644.
- [68] M. A. Ruderman and C. Kittel, ‘Indirect Exchange Coupling of Nuclear Magnetic Moments by Conduction Electrons’, *Physical Review*, vol. 96, no. 1, pp. 99–102, Oct. 1954, doi: 10.1103/PhysRev.96.99.

Bibliography

- [69] T. Kasuya, 'A Theory of Metallic Ferro- and Antiferromagnetism on Zener's Model', *Progress of Theoretical Physics*, vol. 16, no. 1, pp. 45–57, Jul. 1956, doi: 10.1143/PTP.16.45.
- [70] K. Yosida, 'Magnetic Properties of Cu-Mn Alloys', *Physical Review*, vol. 106, no. 5, pp. 893–898, Jun. 1957, doi: 10.1103/PhysRev.106.893.
- [71] L. M. Roth, H. J. Zeiger, and T. A. Kaplan, 'Generalization of the Ruderman-Kittel-Kasuya-Yosida Interaction for Nonspherical Fermi Surfaces', *Physical Review*, vol. 149, no. 2, pp. 519–525, Sep. 1966, doi: 10.1103/PhysRev.149.519.
- [72] P. Bruno and C. Chappert, 'Oscillatory coupling between ferromagnetic layers separated by a nonmagnetic metal spacer', *Phys Rev Lett*, vol. 67, no. 12, pp. 1602–1605, Sep. 1991, doi: 10.1103/PhysRevLett.67.1602.
- [73] B. Dieny, J. P. Gavigan, and J. P. Rebouillat, 'Magnetisation processes, hysteresis and finite-size effects in model multilayer systems of cubic or uniaxial anisotropy with antiferromagnetic coupling between adjacent ferromagnetic layers', *Journal of Physics: Condensed Matter*, vol. 2, no. 1, pp. 159–185, Jan. 1990, doi: 10.1088/0953-8984/2/1/013.
- [74] W. Folkerts, 'Calculated magnetic phase diagrams and magnetoresistance curves for an antiferromagnetically coupled multilayer system', *J Magn Magn Mater*, vol. 94, no. 3, pp. 302–310, Mar. 1991, doi: 10.1016/0304-8853(91)90091-N.
- [75] L. LANDAU and E. LIFSHITZ, 'On the theory of the dispersion of magnetic permeability in ferromagnetic bodies', in *Perspectives in Theoretical Physics*, Elsevier, 1992, pp. 51–65. doi: 10.1016/B978-0-08-036364-6.50008-9.
- [76] T. L. Gilbert, 'Classics in Magnetism A Phenomenological Theory of Damping in Ferromagnetic Materials', *IEEE Trans Magn*, vol. 40, no. 6, pp. 3443–3449, Nov. 2004, doi: 10.1109/TMAG.2004.836740.
- [77] D. Petit, A.-V. Jausovec, D. Read, and R. P. Cowburn, 'Domain wall pinning and potential landscapes created by constrictions and protrusions in ferromagnetic nanowires', *J Appl Phys*, vol. 103, no. 11, p. 114307, Jun. 2008, doi: 10.1063/1.2936981.
- [78] D. Chiba *et al.*, 'Electric-field control of magnetic domain-wall velocity in ultrathin cobalt with perpendicular magnetization', *Nat Commun*, vol. 3, no. 1, p. 888, Jun. 2012, doi: 10.1038/ncomms1888.

Bibliography

- [79] J. H. Franken, H. J. M. Swagten, and B. Koopmans, ‘Shift registers based on magnetic domain wall ratchets with perpendicular anisotropy’, *Nat Nanotechnol*, vol. 7, no. 8, pp. 499–503, Aug. 2012, doi: 10.1038/nnano.2012.111.
- [80] D. C. Langreth and J. W. Wilkins, ‘Theory of Spin Resonance in Dilute Magnetic Alloys’, *Phys Rev B*, vol. 6, no. 9, pp. 3189–3227, Nov. 1972, doi: 10.1103/PhysRevB.6.3189.
- [81] B. Coqblin and J. R. Schrieffer, ‘Exchange Interaction in Alloys with Cerium Impurities’, *Physical Review*, vol. 185, no. 2, pp. 847–853, Sep. 1969, doi: 10.1103/PhysRev.185.847.
- [82] L. Berger, ‘Low-field magnetoresistance and domain drag in ferromagnets’, *J Appl Phys*, vol. 49, no. 3, pp. 2156–2161, Mar. 1978, doi: 10.1063/1.324716.
- [83] A. Yamaguchi, T. Ono, S. Nasu, K. Miyake, K. Mibu, and T. Shinjo, ‘Real-Space Observation of Current-Driven Domain Wall Motion in Submicron Magnetic Wires’, *Phys Rev Lett*, vol. 92, no. 7, p. 077205, Feb. 2004, doi: 10.1103/PhysRevLett.92.077205.
- [84] S. Zhang and Z. Li, ‘Roles of Nonequilibrium Conduction Electrons on the Magnetization Dynamics of Ferromagnets’, *Phys Rev Lett*, vol. 93, no. 12, p. 127204, Sep. 2004, doi: 10.1103/PhysRevLett.93.127204.
- [85] G. Dresselhaus, ‘Spin-Orbit Coupling Effects in Zinc Blende Structures’, *Physical Review*, vol. 100, no. 2, pp. 580–586, Oct. 1955, doi: 10.1103/PhysRev.100.580.
- [86] E. I. J. S. P. Rashba, ‘Properties of semiconductors with an extremum loop. I. Cyclotron and combinational resonance in a magnetic field perpendicular to the plane of the loop’, *Sov. Phys.-Solid State*, vol. 2, p. 1109, 1960.
- [87] A. Manchon, H. C. Koo, J. Nitta, S. M. Frolov, and R. A. Duine, ‘New perspectives for Rashba spin–orbit coupling’, *Nat Mater*, vol. 14, no. 9, pp. 871–882, Sep. 2015, doi: 10.1038/nmat4360.
- [88] D. Xiao, M.-C. Chang, and Q. Niu, ‘Berry phase effects on electronic properties’, *Rev Mod Phys*, vol. 82, no. 3, pp. 1959–2007, Jul. 2010, doi: 10.1103/RevModPhys.82.1959.
- [89] Y. K. Kato, R. C. Myers, A. C. Gossard, and D. D. Awschalom, ‘Observation of the Spin Hall Effect in Semiconductors’, *Science (1979)*, vol. 306, no. 5703, pp. 1910–1913, Dec. 2004, doi: 10.1126/science.1105514.

Bibliography

- [90] J. Sinova, S. O. Valenzuela, J. Wunderlich, C. H. Back, and T. Jungwirth, ‘Spin Hall effects’, *Rev Mod Phys*, vol. 87, no. 4, pp. 1213–1260, Oct. 2015, doi: 10.1103/RevModPhys.87.1213.
- [91] N. Nagaosa, J. Sinova, S. Onoda, A. H. MacDonald, and N. P. Ong, ‘Anomalous Hall effect’, *Rev Mod Phys*, vol. 82, no. 2, pp. 1539–1592, May 2010, doi: 10.1103/RevModPhys.82.1539.
- [92] A. Hoffmann, ‘Spin Hall Effects in Metals’, *IEEE Trans Magn*, vol. 49, no. 10, pp. 5172–5193, Oct. 2013, doi: 10.1109/TMAG.2013.2262947.
- [93] R. A. Duine, K. J. Lee, S. S. P. Parkin, and M. D. Stiles, ‘Synthetic antiferromagnetic spintronics’, *Nat Phys*, vol. 14, no. 3, pp. 217–219, 2018, doi: 10.1038/s41567-018-0050-y.
- [94] J. Chico *et al.*, ‘Thermally driven domain-wall motion in Fe on W(110)’, *Phys Rev B Condens Matter Mater Phys*, vol. 90, no. 1, Jul. 2014, doi: 10.1103/PhysRevB.90.014434.
- [95] W. Jiang *et al.*, ‘Direct Imaging of Thermally Driven Domain Wall Motion in Magnetic Insulators’, *Phys Rev Lett*, vol. 110, no. 17, p. 177202, Apr. 2013, doi: 10.1103/PhysRevLett.110.177202.
- [96] P. Duranka, J. Onufer, and J. Ziman, ‘Effect of temperature on domain wall dynamics in magnetic microwire’, in *AIP Conference Proceedings*, American Institute of Physics Inc., Aug. 2018. doi: 10.1063/1.5048860.
- [97] J. L. García-Palacios and F. J. Lázaro, ‘Langevin-dynamics study of the dynamical properties of small magnetic particles’, *Phys Rev B*, vol. 58, no. 22, pp. 14937–14958, Dec. 1998, doi: 10.1103/PhysRevB.58.14937.
- [98] E. Martinez, L. Lopez-Diaz, L. Torres, C. Tristan, and O. Alejos, ‘Thermal effects in domain wall motion: Micromagnetic simulations and analytical model’, *Phys Rev B*, vol. 75, no. 17, p. 174409, May 2007, doi: 10.1103/PhysRevB.75.174409.
- [99] D. Ravelosona, D. Lacour, J. A. Katine, B. D. Terris, and C. Chappert, ‘Nanometer Scale Observation of High Efficiency Thermally Assisted Current-Driven Domain Wall Depinning’, *Phys Rev Lett*, vol. 95, no. 11, p. 117203, Sep. 2005, doi: 10.1103/PhysRevLett.95.117203.
- [100] E. Martinez, L. Lopez-Diaz, O. Alejos, L. Torres, and C. Tristan, ‘Thermal Effects on Domain Wall Depinning from a Single Notch’, *Phys Rev Lett*, vol. 98, no. 26, p. 267202, Jun. 2007, doi: 10.1103/PhysRevLett.98.267202.

Bibliography

- [101] H.-B. Braun, ‘Fluctuations and instabilities of ferromagnetic domain-wall pairs in an external magnetic field’, *Phys Rev B*, vol. 50, no. 22, pp. 16485–16500, Dec. 1994, doi: 10.1103/PhysRevB.50.16485.
- [102] K. W. Kim and H. W. Lee, ‘Thermal fluctuation field for current-induced domain wall motion’, *Phys Rev B Condens Matter Mater Phys*, vol. 82, no. 13, Oct. 2010, doi: 10.1103/PhysRevB.82.134431.
- [103] R. A. Duine and C. M. Smith, ‘Creep of current-driven domain-wall lines: Effects of intrinsic versus extrinsic pinning’, *Phys Rev B Condens Matter Mater Phys*, vol. 77, no. 9, Mar. 2008, doi: 10.1103/PhysRevB.77.094434.
- [104] R. A. Duine, A. S. Núñez, and A. H. MacDonald, ‘Thermally Assisted Current-Driven Domain-Wall Motion’, *Phys Rev Lett*, vol. 98, no. 5, p. 056605, Feb. 2007, doi: 10.1103/PhysRevLett.98.056605.
- [105] G. Tatara, N. Vernier, and J. Ferré, ‘Universality of thermally assisted magnetic domain-wall motion under spin torque’, *Appl Phys Lett*, vol. 86, no. 25, p. 252509, Jun. 2005, doi: 10.1063/1.1951058.
- [106] Y. Yang, C.-H. Lambert, J. Bokor, S. Salahuddin, R. B. Wilson, and J. Gorchon, ‘Ultrafast magnetization reversal by picosecond electrical pulses’, *Sci Adv*, vol. 3, no. 11, p. e1603117, 2017, doi: 10.1126/sciadv.1603117.
- [107] K. Garello *et al.*, ‘Ultrafast magnetization switching by spin-orbit torques’, *Appl Phys Lett*, vol. 105, no. 21, 2014, doi: 10.1063/1.4902443.
- [108] R. Kubo, ‘The fluctuation-dissipation theorem’, *Reports on Progress in Physics*, vol. 29, no. 1, p. 306, Jan. 1966, doi: 10.1088/0034-4885/29/1/306.
- [109] P. J. Kelly and R. D. Arnell, ‘Magnetron sputtering: a review of recent developments and applications’, *Vacuum*, vol. 56, no. 3, pp. 159–172, Mar. 2000, doi: 10.1016/S0042-207X(99)00189-X.
- [110] S. Foner, ‘Versatile and Sensitive Vibrating-Sample Magnetometer’, *Review of Scientific Instruments*, vol. 30, no. 7, pp. 548–557, Jul. 1959, doi: 10.1063/1.1716679.
- [111] Y. Chen, ‘Nanofabrication by electron beam lithography and its applications: A review’, *Microelectron Eng*, vol. 135, pp. 57–72, Mar. 2015, doi: 10.1016/j.mee.2015.02.042.
- [112] K. Nojiri, *Dry Etching Technology for Semiconductors*. Cham: Springer International Publishing, 2015. doi: 10.1007/978-3-319-10295-5.
- [113] P. S. Pershan, ‘Magneto-Optical Effects’, *J Appl Phys*, vol. 38, no. 3, pp. 1482–1490, Mar. 1967, doi: 10.1063/1.1709678.

Bibliography

- [114] P. Bruno, Y. Suzuki, and C. Chappert, ‘Magneto-optical Kerr effect in a paramagnetic overlayer on a ferromagnetic substrate: A spin-polarized quantum size effect’, *Phys Rev B*, vol. 53, no. 14, pp. 9214–9220, Apr. 1996, doi: 10.1103/PhysRevB.53.9214.
- [115] P. N. Argyres, ‘Theory of the Faraday and Kerr Effects in Ferromagnetics’, *Physical Review*, vol. 97, no. 2, pp. 334–345, Jan. 1955, doi: 10.1103/PhysRev.97.334.
- [116] L. Uba, S. Uba, V. N. Antonov, A. N. Yaresko, and R. Gontarz, ‘Magneto-optical Kerr spectroscopy of platinum’, *Phys Rev B*, vol. 62, no. 24, pp. 16510–16521, Dec. 2000, doi: 10.1103/PhysRevB.62.16510.
- [117] G.-M. Choi and D. G. Cahill, ‘Kerr rotation in Cu, Ag, and Au driven by spin accumulation and spin-orbit coupling’, *Phys Rev B*, vol. 90, no. 21, p. 214432, Dec. 2014, doi: 10.1103/PhysRevB.90.214432.
- [118] J. Robbins, J. F. Annett, and M. Gradhand, ‘Effect of spin-orbit coupling on the polar Kerr effect in Sr_2RuO_4 ’, *Phys Rev B*, vol. 96, no. 14, p. 144503, Oct. 2017, doi: 10.1103/PhysRevB.96.144503.
- [119] L. Uba, S. Uba, V. N. Antonov, A. N. Yaresko, and R. Gontarz, ‘Magneto-optical Kerr spectroscopy of platinum’, *Phys Rev B*, vol. 62, no. 24, pp. 16510–16521, Dec. 2000, doi: 10.1103/PhysRevB.62.16510.
- [120] J. McCord, ‘Progress in magnetic domain observation by advanced magneto-optical microscopy’, *J Phys D Appl Phys*, vol. 48, no. 33, p. 333001, Aug. 2015, doi: 10.1088/0022-3727/48/33/333001.
- [121] A. Stupakiewicz, A. Chizhik, M. Tekielak, A. Zhukov, J. Gonzalez, and A. Maziewski, ‘Direct imaging of the magnetization reversal in microwires using all-MOKE microscopy’, *Review of Scientific Instruments*, vol. 85, no. 10, p. 103702, Oct. 2014, doi: 10.1063/1.4896758.
- [122] Z. Luo *et al.*, ‘Chirally coupled nanomagnets’, *Science (1979)*, vol. 363, no. 6434, pp. 1435–1439, Mar. 2019, doi: 10.1126/science.aau7913.
- [123] Z. Luo *et al.*, ‘Field- and Current-Driven Magnetic Domain-Wall Inverter and Diode’, *Phys Rev Appl*, vol. 15, no. 3, p. 034077, Mar. 2021, doi: 10.1103/PhysRevApplied.15.034077.
- [124] J. Balcerzak, W. Redzyna, and J. Tyczkowski, ‘In-situ XPS analysis of oxidized and reduced plasma deposited ruthenium-based thin catalytic films’, *Appl Surf Sci*, vol. 426, pp. 852–855, Dec. 2017, doi: 10.1016/j.apsusc.2017.07.248.

Bibliography

- [125] S. Fukami, M. Yamanouchi, S. Ikeda, and H. Ohno, ‘Depinning probability of a magnetic domain wall in nanowires by spin-polarized currents’, *Nat Commun*, vol. 4, no. 1, p. 2293, Aug. 2013, doi: 10.1038/ncomms3293.
- [126] B. Raquet *et al.*, ‘Dynamical properties of magnetization reversal in an ultrathin film’, *J Magn Magn Mater*, vol. 150, no. 1, pp. L5–L12, Sep. 1995, doi: 10.1016/0304-8853(95)00515-3.
- [127] C. Garg, S.-H. Yang, T. Phung, A. Pushp, and S. S. P. Parkin, ‘Dramatic influence of curvature of nanowire on chiral domain wall velocity’, *Sci Adv*, vol. 3, no. 5, May 2017, doi: 10.1126/sciadv.1602804.
- [128] C. Garg *et al.*, ‘Highly Asymmetric Chiral Domain-Wall Velocities in Y-Shaped Junctions’, *Nano Lett*, vol. 18, no. 3, pp. 1826–1830, Mar. 2018, doi: 10.1021/acs.nanolett.7b05086.
- [129] S.-H. Yang, C. Garg, T. Phung, C. Rettner, and B. Hughes, ‘Spin-Orbit Torque Driven One-Bit Magnetic Racetrack Devices - Memory and Neuromorphic Applications’, in *2019 International Symposium on VLSI Technology, Systems and Application (VLSI-TSA)*, IEEE, Apr. 2019, pp. 1–2. doi: 10.1109/VLSI-TSA.2019.8804677.
- [130] S.-W. Lee and K.-J. Lee, ‘Emerging Three-Terminal Magnetic Memory Devices’, *Proceedings of the IEEE*, vol. 104, no. 10, pp. 1831–1843, Oct. 2016, doi: 10.1109/JPROC.2016.2543782.
- [131] N. Sato *et al.*, ‘Domain Wall Based Spin-Hall Nano-Oscillators’, *Phys Rev Lett*, vol. 123, no. 5, p. 057204, Aug. 2019, doi: 10.1103/PhysRevLett.123.057204.
- [132] E. Raymenants *et al.*, ‘Nanoscale domain wall devices with magnetic tunnel junction read and write’, *Nat Electron*, vol. 4, no. 6, pp. 392–398, Jun. 2021, doi: 10.1038/s41928-021-00593-x.

Eidesstattliche Erklärung

Ich, Jiho Yoon, erkläre an Eides statt, dass ich die Arbeit selbstständig und ohne fremde Hilfe verfasst, keine anderen als die von mir angegebenen Quellen und Hilfsmittel benutzt und die den benutzten Werken wörtlich oder inhaltlich entnommenen Stellen als solche kenntlich gemacht habe.

Halle (Saale), den 26. 06. 2023

(Jiho Yoon)

Curriculum vitae

Jiho Yoon

Education

- 02/2017 – 06/2023 **PhD student at Martin Luther University of Halle-Wittenberg and research assistant at Max Planck Institute of Microstructure Physics, Halle (Saale), Germany**
PhD thesis: *Chiral magnetic domain wall dynamics in synthetic antiferromagnet-ferromagnet lateral junctions*
- 03/2014 – 09/2016 **Dual Master's degree program**
Master of Engineering in Innovation Technologie: engineering and entrepreneurship at École polytechnique, Palaiseau, France
Master of Engineering in information display at Kyung Hee University, Seoul, Republic of Korea
Master thesis in cooperation with **Columbia University in the City of New York, New York, USA: Perfluorinated self-assembled monolayers treated alternative electrode for organic thin film transistors**
- 03/2008 – 02/2014 **Bachelor of Science in Information Display at Kyung Hee University, Seoul, Republic of Korea**

Publications

[1] **J. Yoon**, S.-H. Yang, J.-C. Jeon, A. Migliorini, I. Kostanovskiy, T. Ma, and S. S. P. Parkin, ‘Local and global energy barriers for chiral domain walls in synthetic antiferromagnet–ferromagnet lateral junctions’, *Nat. Nanotechnol.*, vol. 17, no. 11, pp. 1183–1191, Nov. 2022, doi: 10.1038/s41565-022-01215-z.

[2] **J. Yoon**, E. Lesne, K. Sklarek, J. Sheckelton, C. Pasco, S.S.P. Parkin, T. M. McQueen, and M. N. Ali, ‘Anomalous thickness-dependent electrical conductivity in van der Waals layered transition metal halide, Nb₃Cl₈’, *J. Phys.: Condens. Matter*, 32, 30400, 2020, doi: 10.1088/1361-648X/ab832b.

[3] D.J. Hagen, **J. Yoon**, H. Zhang, B. Kalkofen, M. Silinskas, F. Börrnert, H. Han, and S.S.P. Parkin, ‘Atomic layer deposition of the conductive delafossite PtCoO₂’, *Adv.Mater. Interfaces*, 9, 2200013, 2022.

[4] K.-R. Jeon, J.-K. Kim, **J. Yoon**, J.-C. Jeon, H. Han, A. Cottet, T. Kontos, and S.S.P. Parkin, ‘Zero-field polarity-reversible Josephson supercurrent diodes enabled by a proximity-magnetized Pt barrier’, *Nat. Mater.* vol. 21, no. 9, pp. 1008–1013, 2022.

[5] Y.-B. Choi, Y. Xie, C.-Z. Chen, J. Park, S.-B. Song, **J. Yoon**, B.J. Kim, T. Taniguchi, K. Watanabe, J. Kim, K.C. Fong, M.N. Ali, K.T. Law, G.-H. Lee, ‘Evidence of higher-order topology in multilayer WTe₂ from Josephson coupling through anisotropic hinge states’, *Nat. Mater.*, vol. 19, no. 9, pp. 974–979, 2020.

[6] H. Han, A. Sharma, H.L. Meyerheim, **J. Yoon**, H. Deniz, K.-R. Jeon, A.K. Sharma, K. Mohseni, C. Guillemard, M. Valvidares, P. Gargiani, and S.S.P. Parkin, ‘Control of oxygen vacancy ordering in brownmillerite thin films via ionic liquid gating’, *ACS Nano*, 16, 4, 6206–6214, 2022.

[7] K.-R. Jeon, J.-C. Jeon, X. Zhou, A. Migliorini, **J. Yoon**, and S.S.P. Parkin, ‘Giant transition-state quasiparticle spin-Hall effect in an exchange-spin-split superconductor detected by nonlocal magnon spin transport’, *ACS Nano*, 14, 11, 15874-15883, 2020.

[8] K.-R. Jeon, K. Cho, A. Chakraborty, J.-C. Jeon, **J. Yoon**, H. Han, J.-K. Kim, and S.S.P. Parkin, ‘Role of two-dimensional Ising superconductivity in the nonequilibrium quasiparticle spin-to-charge conversion efficiency’, *ACS Nano*, 15, 10, 16819-16827, 2021.

[9] A. Weiland, D.G. Chaparro, M.G. Vergniory, E. Derunova, **J. Yoon**, I.W.H. Oswald, G.T. McCandless, M.N. Ali, J.Y. Chan, ‘Band structure engineering of chemically tunable LnSbTe(Ln=La, Ce, Pr)’, *APL Mater*, 7, 10, 101113, 2019

Patent applications

[1] S.S.P. Parkin, S.-H. Yang, **J. Yoon**, and U.H. Pi, Magnetic memory device, US Patent App. 18/050, 600, 2023.

[2] S.S.P. Parkin, S.-H. Yang, **J. Yoon**, and U.H. Pi, Magnetic memory devices, US Patent App. 17/983, 554, 2023

[3] S.S.P. Parkin, S.-H. Yang, **J. Yoon**, and U.H. Pi, Magnetic memory devices and methods for initializing the same, US Patent App. 18/051, 857

Conference contributions

[1] **J. Yoon**, E. Lesne, J. Sheckelton, C. Pasco, T. McQueen, S.S.P. Parkin, M.N. Ali, ‘Electronic transport in layered van der Waals Kagome lattice cluster compounds Nb_3X_8 ’, *American Physical Society March Meeting*, Los Angeles, USA, 2018.

[2] **J. Yoon**, S.-H. Yang, J.-C. Jeon, A. Migliorini, I. Kostanovskiy, T. Ma, and S. S. P. Parkin, ‘Giant thermal stability and efficient current-driven motion of chiral magnetic domain walls in ferromagnet-synthetic antiferromagnet lateral junctions’, *American Physical Society March Meeting*, Las Vegas, USA, 2023.